Model Coupled Accelerator Tuning

by

Olivier Shelbaya
M.Sc., McGill University, 2012

A Dissertation Submitted in Partial Fulfillment of the
Requirements for the Degree of

Doctor of Philosophy

in the Department of Physics and Astronomy

Model Coupled Accelerator Tuning

by

Olivier Shelbaya
M.Sc., McGill University, 2012

Supervisory Committee

Dr. O. Kester, Co-Supervisor
(*Department of Physics and Astronomy / TRIUMF*)

Dr. D. Karlen, Co-Supervisor
(*Department of Physics and Astronomy*)

Dr. T. Junginger, Departmental Member
(*Department of Physics and Astronomy*)

Dr. P. So, Outside Member
(*Department of Electrical and Computer Engineering*)

Abstract

Relativistic charged particle optics in the context of accelerator physics have been treated using transfer matrix methods since the 1950s. The realization that a hyperellipsoidal charged particle distribution could likewise be transformed if its 6-dimensional covariance matrix was used, with diagonal elements as the squared sizes, allowed for a computationally efficient and generalizable means to perform beam optics studies and analysis. Initially confined to elements with constant focal strengths, representable as square functions along the reference orbit and limited to constant energy beamline sections, such methods have not been applied to accelerated beam envelopes. Instead, the latter have to date been reserved for multiparticle simulations, more computationally taxing. The envelope code `TRANSOPTR`, developed at Chalk River Nuclear Laboratories in the late 1970s, added to the repertoire of envelope simulation capabilities by using a quadraticized Hamiltonian about a Frenet-Serret reference particle frame, for numerical integration of beam envelopes subject to scalar and vector potentials, including time-dependency. In this work, the beam-envelope simulation capabilities of `TRANSOPTR` are extended to include rf quadrupole accelerators and applied to include drift tube linear accelerators, enabling a full envelope model of the ISAC-I linac, leading to the identification of a long standing issue with its design tune. A corrective tuning prescription is elaborated for the ISAC-DTL. The novel tuning method significantly reduces accelerator operation complexity and therefore overhead time, by coupling machine tuning to parallel, beam diagnostic fed simulations. The generalizibility of the MCAT approach and speed of `TRANSOPTR` produce a suitable candidate for site-wide roll-out as the standard feedback driven accelerator tuning control software.

Table of Contents

List of Tables

List of Figures

List of Acronyms

DTL	Drift Tube Linac
FODO	Focus, Drift, Defocus, Drift
HEBT	High Energy Beam Transport
IH	Interdigital H-mode
ILT	ISAC Low Energy Transport
IMS	ISAC Mass Separator
IOS	ISAC Ion Source Transport
IRA	ISAC RFQ Injection Beamline
ISAC	Isotope Separator and Accelerator
ISOL	Isotope Separation On-Line
LEBT	Low Energy Beam Transport
LINAC	Linear Accelerator
LPM	Linear Position Monitor
MCIS	Multicharge Ion Source
MEBT	Medium Energy Beam Transport
MWS	Microwave Source
MB	Magnetic Bender
OLIS	Offline Ion Source
rf	Radio Frequency
RFQ	Radiofrequency Quadrupole
RIB	Radioactive Ion Beam
rms	Root Mean Square
RPM	Rotary Position Monitor
SEBT	Superconducting Energy Beam Transport
TTF	Transit Time Factor
UCx	Uranium Carbide

Acknowledgements

Ce fut un voyage difficile.

I want to thank first and foremost Oliver Kester, for guiding and supporting this work from its infancy. Rick Baartman has been a constant (and patient) source of wisdom, advice and feedback and I thank him sincerely. Thanks to Dean Karlen for his valuable input and guidance during this project. Violeta Toma is dearly thanked, for having provided me the opportunity to be an operator at TRIUMF in 2012, a path which led to this work.

Thomas Planche and Paul Jung have aided significantly with their advice, review and code, and I thank them both. Stephanie Rädel provided invaluable assistance, particularly in the MEBT and DTL sections, which were difficult and at times frustrating. Thanks to Tiffany Angus and all Operators, my colleagues. Thanks to Spencer Kiy and Dan Thomson.

Phil Lagogiannis, Joel Beaudry and Kirk North, the Montréal connection, are thanked for their much needed distractions and physics discussions, particularly during confinement.

And finally, thanks to my family; Dad for instilling in me a love of science and Mom for working to allow me to reach this destination. To Fanny for having supported me during this work, it would simply not have been possible without these pillars in my life...

Dedication

Félix

Chapter 1

Introduction

Over the last 100 years there has been a revolution in our understanding of matter, thanks in no small part to the advent of a quantum perspective of elementary particles and interactions. As the methods of nuclear physics and chemistry have become more refined, so too has grown the domain of scrutinized atomic nuclei. This has resulted in a state of affairs where the properties of abundant and stable elements have by now become very exhaustively studied and measured. The discovery of radioactivity culminating in the advent of controlled nuclear fission resulted in an ever-growing ability to synthesize radioactive isotopes. This benefited our understanding of the elements, their genesis in stars, and ultimately the evolution of matter in the universe and our place within it. However, despite the progress in mapping out the known elements, as one strays from the stable entries on the nuclear chart, the state of understanding and knowledge of nuclear properties tends to diminish. Studying unstable matter is part of answering ancient and vast questions...

1.1 Accelerators and Particles

The 20th century also saw the advent of a growing ability to exploit electromagnetism to manipulate streams of ionized particles under vacuum. Emerging technologies such as transistors, amplifiers and oscillators allowed for the gradual increase of complexity and refinement of these devices. Several accelerator designs and geometries have emerged over the years, using time-varying electric fields to achieve energy gain. The unprecedented ability to control and accelerate beams in turn drove the growth of the field of particle physics for which the accelerator remains one of the most valuable experimental tools.

As the maximum achievable energy of accelerators increased over time, so too did the opportunity to study increasingly energetic interactions between particles. During the 1960's, accelerator-based experiments were so prolifically identifying new particles that the period and its discoveries are jokingly referred to as the *particle zoo*. The discovery of the electroweak interaction and quarks[1], once again in accelerator-driven experiments, resolved the disorder by revealing that the unruly list of particles are in fact different bound states of quarks. This culminated in the Standard Model.

1.2 The Cyclotron at TRIUMF

Initially an acronym standing for Tri-University Meson Factory, TRIUMF's earliest mission was centered around the production and study of Mesons, namely Pions or Kaons, and their interactions. At its heart is an 18 m diameter, 520 MeV proton cyclotron which has been accelerating H^- beams since 1974[2]. The machine consists of six magnet sectors (Figure 1.1), which define a vertical magnetic field inside the vacuum chamber that produces magnetic deflection per the Lorentz force law:

$$\vec{F_B} = q(\vec{v} \times \vec{B}).$$

If a particle of mass m is not at rest with respect to the field ($v > 0$), the resulting motion is centripetal:

$$\frac{mv^2}{r} = qvB \tag{1.1}$$

with magnetic resonance frequency[4]:

$$f = \frac{v}{2\pi r} = \frac{qB}{2\pi m}. \tag{1.2}$$

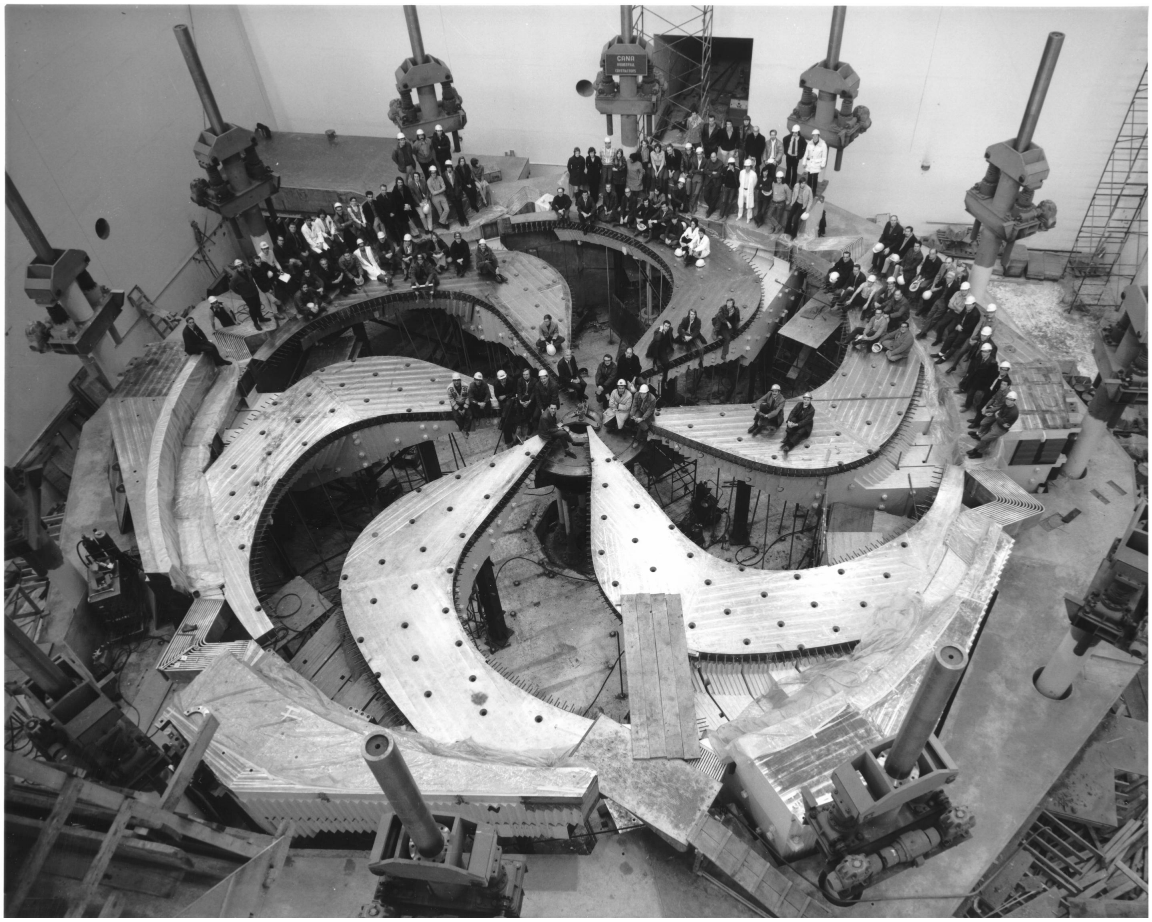

Figure 1.1: The lower segments of the TRIUMF cyclotron main magnets during installation circa 1972[3]. The 520 MeV cyclotron's 18 m main magnet diameter is the largest for a cyclotron. Image obtained from TRIUMF photo archives.

Both equations assume the magnetic field B is normal to the velocity vector. This is known as the cyclotron equation and results in circular trajectories of radius r under vacuum at constant energy. Cyclotrons achieve energy gain using a gap electric field synchronized to the frequency of their revolution in the machine. In TRIUMF's case, the gap spans the diameter of the machine. Acceleration proceeds using a 23.56 MHz oscillating longitudinal electric field, the fifth harmonic of the ion revolution frequency, which provides a small kick in energy as the particles traverse it. As their energy increases, so too does the radius of their trajectory via Eq. (1.1) such that their orbit tends them toward the outer circumference of the machine. Acceleration within the TRIUMF cyclotron of negatively charged hydrogen means that beams can be extracted at any intermediate energy by insertion of a carbon stripping foil. As the beam and foil interact, H^- is stripped of both its electrons. The change in charge state, from negative to positive, inverts the sign of the orbit curvature, allowing extraction. This design choice means TRIUMF's cyclotron enables use of up to five separate beamlines simultaneously at different energies if desired.

Since its inception in the late 1960's, TRIUMF's site has grown considerably with the addition of new facilities such as ISAC's linear accelerators delivering radioactive beams to experiment stations. Most recently, the ARIEL project has added a new driver electron linear accelerator on campus & corresponding network of transport beamlines. No longer dedicated to meson production, as of 2023 TRIUMF consists of a diversity of accelerators and facilities producing and delivering a range of particle beams. There are no longer three full member universities, but fourteen. Though the laboratory has outgrown its acronym, the name lives on.

1.3 Isotope Separation On-Line (ISOL)

Another emergent use of accelerators over the past decades has been the generation of radioactive isotopes by particle bombardment, using a driver accelerator to send beam into a target material. Typically the nuclear reactions at play are spallation, and fragmentation with induced fission to a lesser extent. These transmutations produce unstable radioactive isotopes within the target material, heated to temperatures on the order of thousands of degrees centigrade[5]. This facilitates the diffusive escape of radionuclides from the target material. Ionization can be induced either with an ionizer tube possessing a low work function, or through through collisional excitation with a plasma. In addition, resonant ionization using laser light is possible, enabling the selective charging of individual species. The ionized radioisotopes are extracted to a beam transport system for delivery to experiments. This method is known as Isotope-Separation On-Line (ISOL). TRIUMF's implementation of this concept, the Isotope Separator and Accelerator (ISAC), is shown in Figure 1.2. The cutaway view in the figure includes both the ISAC-I and ISAC-II experimental halls along with the underground 2A proton beamline from the main cyclotron. An ISAC target device is shown in Fig. 1.3. Proton bombardment of the target, made on-site from different materials including UCx, Ta, Nb and SiC[6], drives the production of radioactive isotopes with ISAC target yields shown in Figure 1.4[7]. Target-extracted radioisotope

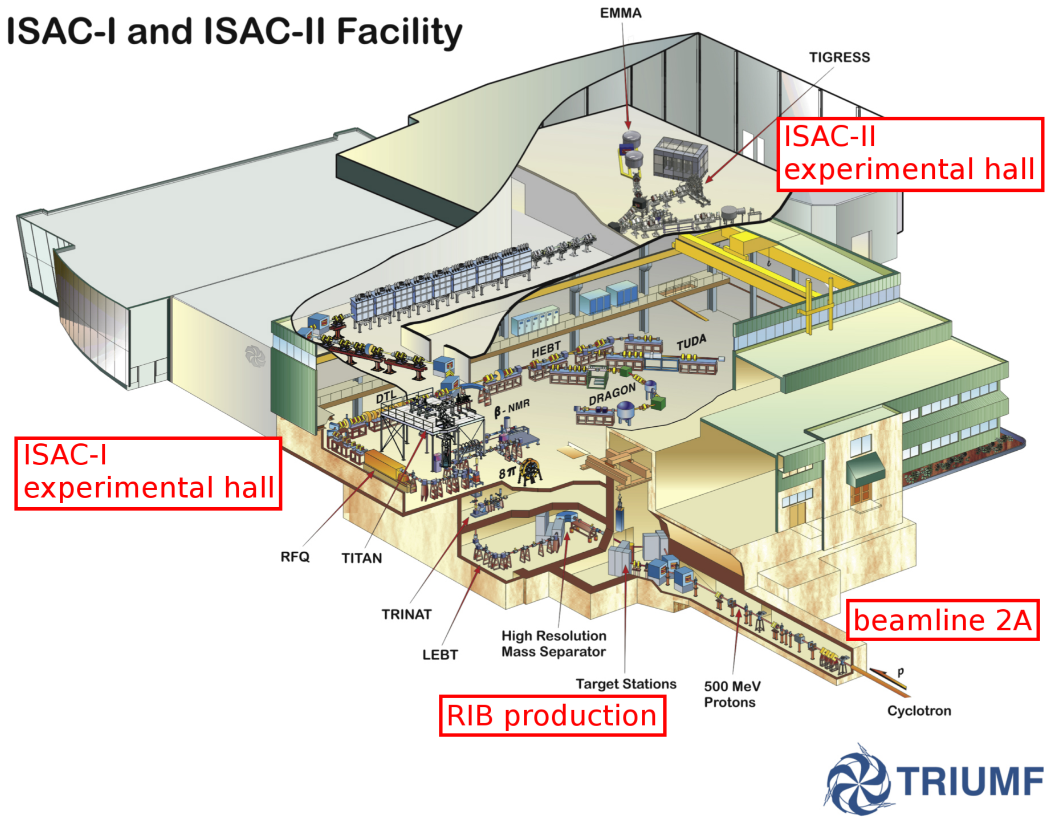

Figure 1.2: Overview of the ISAC facility at TRIUMF, consisting of the ISAC-I (middle) and ISAC-II (top right) experimental halls. The 2A beamline, delivering up to 520 MeV protons from the TRIUMF cyclotron, is located at the bottom right of the figure. At the ISAC target stations (bottom, middle) RIB production proceeds by a variety of nuclear interactions between target material and beam. Original image obtained from the TRIUMF Design Office.

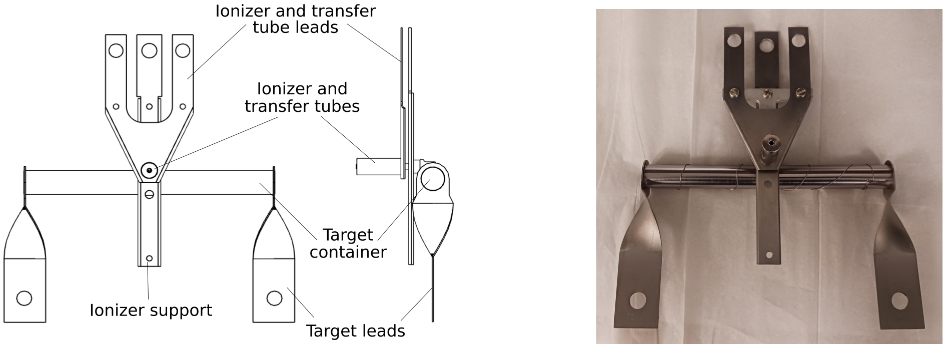

Figure 1.3: **Left:** Diagram of an ISAC target ion source showing a side and front views. **Right:** Picture of an ISAC target, showing connection points for target heating, allowing operation at 2000° C[8]. Images produced by and used with permission from Dr. C. Babcock, TRIUMF.

beams are mass filtered through two analyzing magnets which compose the 135° ISAC high resolution separator (Fig. 1.2), with mass separation resolution of $m/\Delta m = 2000$. Mass-selected beams can also be charge-bred in a charge state booster decreasing the beam's mass-to-charge (A/q) ratio as may be necessary for delivery.

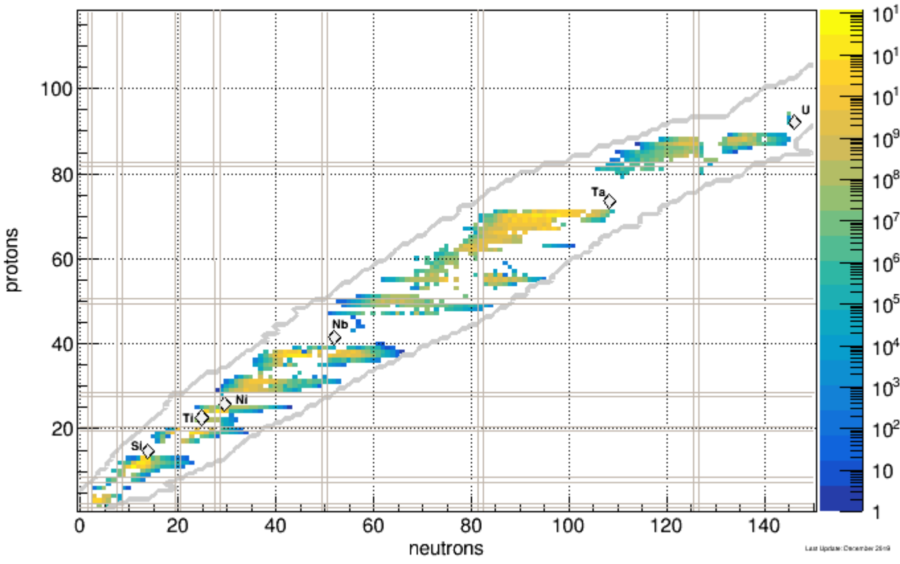

Figure 1.4: Aggregate yield of produced isotopes at ISAC from different specified target materials, as of 2020. Color scale indicates yield in ions/second. Produced by and used with permission from Dr. P. Kunz, TRIUMF.

1.4 The ISAC-I Postaccelerator

Post-accelerators coupled with an ISOL facility enable the study of higher energy radioactive beams. At ISAC, beam acceleration and delivery to experiment is achieved with a series of linear accelerating (linac) structures delivering mass-separated RIBs to detector stations at specified energies. The ISAC-I linac's segments are shown in Figure 1.5. The accelerator consists of two main components: a radiofrequency quadrupole (RFQ) for initial acceleration, followed by a drift tube linac (DTL). Both devices will be further discussed in subsequent chapters. The diversity of requested beam properties for the accelerator (energy, mass-to-charge, intensity, beam spot size, etc..), results in an operational need to frequently reconfigure the machine. This can be time-consuming owing to the complexity of establishing correct beam optics within the linac and beamlines.

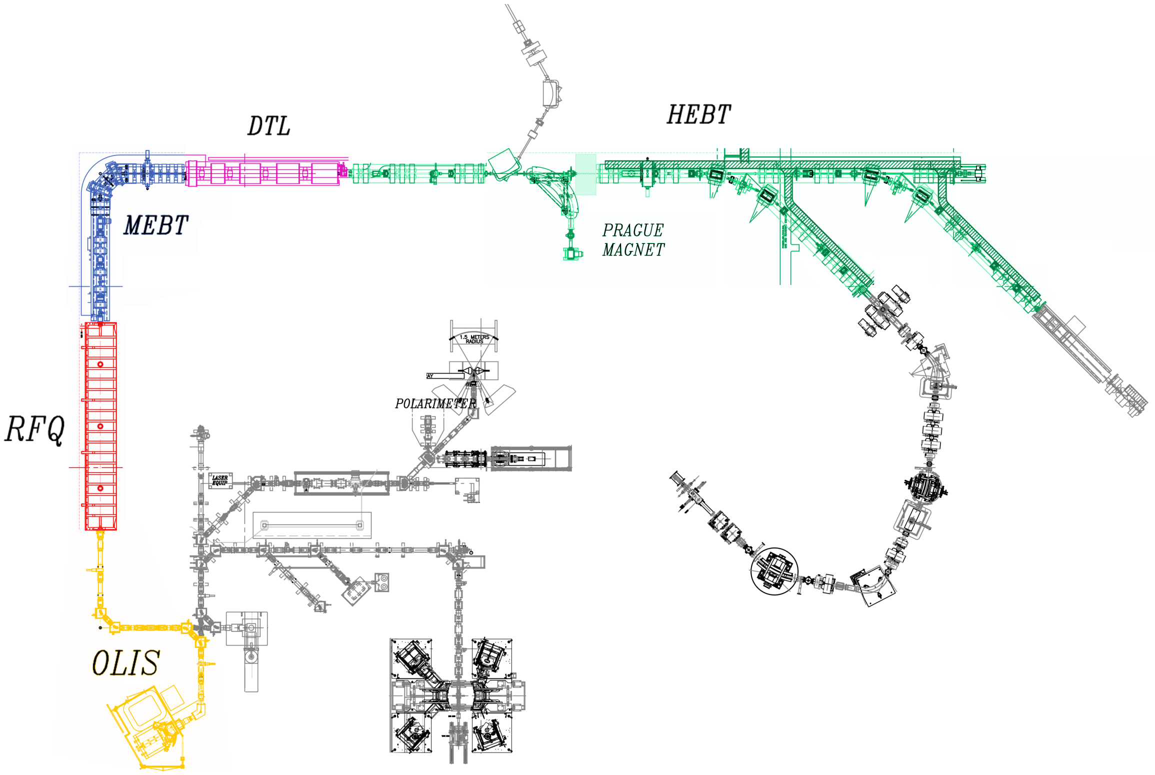

Figure 1.5: Overview of the ISAC Accelerator and ISAC-I beamlines. The ISAC-II superconducting rf component is not shown. Relevant sections of the beamlines and accelerators are colored. Obtained from the TRIUMF Design Office. For scale, the RFQ tank (red) is 8 m long.

1.5 Research Goals

Modern accelerator designs have increased in complexity[9], for example the separated function[10] combined zero degree structure (KONUS)[11], which provides fully variable output energy and flexibility in A/q. The ISAC-I linac (Fig. 1.5) features 17 total rf cavities, which includes bunchers, an RFQ structure and interdigital H-mode (IH) cavities. In order to compute the ”tune” or global configuration of the machine therefore has meant piecing together the outputs of a variety of specialized models which use different codes (`PARMTEQ`, `TraceWin`, `LANA`, `LORASR`, `PARMELA`, etc..), despite each often being based on different operating systems if not from different computing eras altogether. The study of inter-cavity effects and other emergent phenomena such as transmission variations[12] is correspondingly more difficult. It is thus advantageous to study such machines in a unified end-to-end model.

This capability can also be used to compute tunes, provided starting beam conditions, either using available documentation or measured on-line. For a separated function accelerator such as the apparatus at ISAC, the need for an efficient parallel modelling is clear. A fast beam envelope simulation capability can further be used to develop model coupled accelerator tuning applications, for use by operators tasked with the configuration of such a machine for beam delivery. Further, as the accelerator community turns toward machine learning (ML) based tuning techniques, an efficient envelope modelling code is mandatory for the purposes of training an ML-based agent. The goal of the present research project is thus the development of an end-to-end beam envelope model of the ISAC-I linear accelerator in the code `TRANSOPTR` (optr).

To this end, the source for the beam envelope code, in use at TRIUMF for almost four decades[13], has been expanded to enable the simulation of one of the main components of the machine previously lacking: the radiofrequency quadrupole (RFQ) linac[14], using a quadraticized Hamiltonian featuring the two-term Kapchinsky-Teplyakov potential. The ISAC-DTL was further implemented in `TRANSOPTR`[15]. In both cases, these are novel demonstrations of beam transfer matrix optics[16], applied for the simulation and optimization of beam envelopes undergoing acceleration in RFQs and DTLs. This required the generation of static electric field maps in the code `Opera2D`, where models of the radiofrequency (rf) cavities based on original engineering drawings of the linac have been used, in addition to a beam-based verification of `TRANSOPTR`'s predicted DTL E/A output. The medium and high energy transport beamlines (MEBT/HEBT/SEBT) have been constructed in optr as part of this project, with technical reports[17, 18, 19] detailing those implementations. Additionally, a `TRANSOPTR` model of the two gap ISAC-II superconducting rf resonators (SCRF) has been implemented[20]. The full `TRANSOPTR` model of the ISAC linac which is elaborated in this dissertation is intended for use as part of TRIUMF's high level application (HLA) effort[21], which aims to provide operators with tuning applications based on this work[22]. Examples of HLA's include real-time simulation of the beam through the machine, based on live setpoints in the accelerator. For this, a web-based infrastructure has been developed at TRIUMF which enables interfacing with the machine's control system, `EPICS`[23]. By polling the latter in real time, it is possible to supply the model with these setpoints, perform an optimization and return the values to the machine, coupling envelope modelling and machine tuning.

This dissertation is divided into six chapters, including the present introduction. Chapter 2 consists of an overview of elementary concepts relevant to accelerator tuning and beam dynamics. In Chapter 3, the envelope code `TRANSOPTR` is discussed along with the underlying Hamiltonian framework allowing for the treatment of relativistic charged particle beams undergoing acceleration and introduces `python`[24] software developed with the envelope code enabling full linac tune computations. Chapter 4 showcases the main components of the ISAC linac, along with their `TRANSOPTR` implementations: the ISAC-RFQ and DTL. Benchmark simulations with particle codes are presented for both, in addition to a demonstration of the full end-to-end envelope simulation capability that has now been developed. An analysis of the MEBT optics is presented, using the model to understand the longstanding observation that DTL quadrupoles, when set to model computed values did not produce good beam quality, instead causing low transmission. Chapter 5 presents beam-based data obtained with the coupled use of the model, including the low energy sections. A calibration between `TRANSOPTR` and on-line DTL cavity rf amplitude settings, based on $^{16}O^{4+}$ beam data, is presented. This notably allows for the use of `TRANSOPTR` to compute full linac tunes including prediction of DTL tank energies, the culmination of this dissertation. A conclusion is presented in Chapter 6, reviewing the work and discussing future prospects for development and research with this new tool.

Chapter 2

Survey of Beam Optics

This chapter presents a brief overview of the basic concepts in beam optics, introducing the sliding Frenet-Serret reference particle frame and important quantities relevant to the computation of beam containment envelopes and phase space ellipses. Transfer matrices for select optical elements are presented and discussed, along with concepts such as mismatches, energy gain and transit time factors. Nonlinear accelerating cavity behaviour is introduced.

2.1 Frenet-Serret Coordinates

Tracking the evolution of charged particles along an accelerator requires computing very fine and quite large quantities, for example the evolution of a millimetre wide beam over several dozen meters of travelled beampath or more. It is thus chosen to adopt a sliding reference frame and separately track the total length of its displacement. This avoids mixing both small and large quantities, which can introduce sensitivity to rounding errors. The Frenet-Serret coordinate system shown in Figure 2.1 is chosen for the tracking of particle distributions moving through electromagnetic fields over large travelled distances. It consists of a moving, at times non-inertial set of orthogonal coordinates which are attached to a reference particle, about which is centered the remainder of the ion distribution. The position vector $\vec{R}$ and basis vectors $\hat{x}, \hat{y}, \hat{s}$ are referenced to a fixed origin point $\mathcal{O}$ and relate to each other by:

$$\vec{R} = x\hat{x} + y\hat{y} + \vec{R_0}(s), \tag{2.1}$$

$$\hat{x} \times \hat{y} = \hat{s} \tag{2.2}$$

and (x, y) are the transverse coordinates with respect to the reference. The unit vector $\hat{s}$ points in the direction of beam propagation, while $\hat{x}$ is in the osculating plane of the curvature. Both $\hat{x}$ and $\hat{y}$ are always transverse to the propagation axis by Eq. (2.2). The vector $\vec{R_0}(s)$ follows the reference particle through the system. Owing to its frequent use in circular accelerators, the Frenet-Serret reference trajectory s is also referred to as the reference orbit, even if not necessarily circular, as is the case for linacs. A longitudinal small displacement vector $\vec{z}$ is also defined with respect to the reference particle, collinear to $\hat{s}$:

$$\vec{z} \times \hat{s} = \vec{0}. \tag{2.3}$$

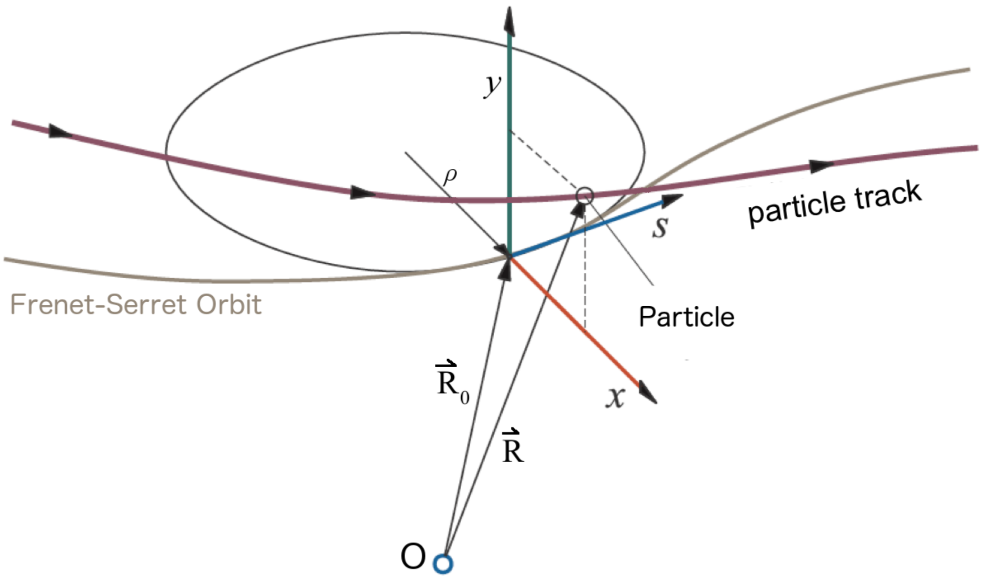

Figure 2.1: Representation of a Frenet-Serret coordinate system, centered at the origin point **O**. The vector $\vec{R}$ tracks an arbitrary particle which follows the specified trajectory, while the Frenet-Serret orbit, corresponding to the reference trajectory through the system, is tracked with the vector $\vec{R_0}$. A small displacement vector $\vec{z}$ is also defined, collinear to the propagation direction $\hat{s}$. Image obtained from R. Baartman, TRIUMF, adapted from[25].

For curvature along an orbit of radius $\rho(s)$ in the x-plane, the associated longitudinal momentum vector becomes:

$$P_s = \vec{P} \cdot \hat{s}\left(1 + \frac{x}{\rho(s)}\right). \tag{2.4}$$

The s-coordinate refers to the beam propagation distance defined by the reference particle's trajectory. In the case of linear accelerators ρ is infinite.

2.2 Envelope, rms and Emittance

When tracking the collective motion of a distribution of particles, it can become impractical to consider individual trajectories. As an example, a beam current of one nanoampere (10^{-9}A) of singly charged ions corresponds to roughly 6×10^{9} particles per second. Instead, the beam envelope, which measures the extent of their collective trajectories can be tracked, shown in Figure 2.2. It is much less burdensome to work with a handful of envelope size parameters and it also allows for greater computational efficiency. In the remainder of this work, the metric of choice to measure the spread of a distribution is the root mean square or rms:

$$x_{\text{rms}} = \sqrt{\frac{1}{N}\sum_{i=1}^{N} x_i^2}. \tag{2.5}$$

If the underlying population is Gaussian and two-dimensional, the 2 rms envelope encapsulates 86% of the particles. Though position coordinates typically have units of centimeters or millimeters, the transverse momenta (P_x, P_y) are typically normalized to the total beam momentum P_0, which is generally orders of magnitude greater. Both are by definition at right angles to each other, producing a transverse momenta definition expressed as a small divergence angle with respect to P_0, typically in milliradians. This paraxial approximation allows for the expression of the transverse momentum as a divergence angle x':

$$x' \equiv \frac{\mathrm{d}x}{\mathrm{d}s} = \frac{P_x}{P_0}. \tag{2.6}$$

The approximation is only valid if the momentum does not contain vector potential terms. In this dissertation, unless otherwise specified, use of x' to represent transverse canonical momentum assumes this. For a given conjugate (x, x') phase space particle distribution, a common approach in beam optics is to parameterize its extent as that of an ellipse, using the Twiss or Courant-Snyder parameters[27], which define a tilted ellipse:

$$\epsilon_{\mathrm{rms}} = \gamma x^2 + 2\alpha x x' + \beta x'^2. \tag{2.7}$$

Gaussian phase space particle distributions possess contours of constant density which are ellipses. Eq. (2.7) defines one of emittance ϵ_{rms} which contains 86% of the population. An unfortunate reality in accelerator physics is the coexistence of two definitions for the symbols (β, γ): the relativistic definitions and the Twiss parameters. For this reason, it is always necessary to specify the context of its use. The Twiss parameters (α, β, γ) are related to each other by:

$$\beta\gamma = 1 + \alpha^2. \tag{2.8}$$

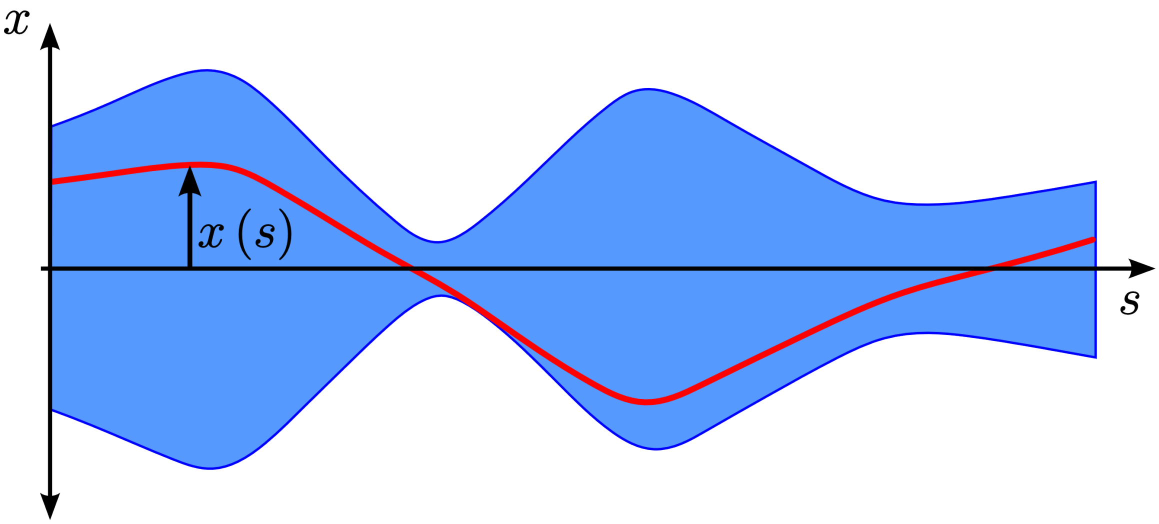

Figure 2.2: Representation of the envelope of a beam (blue), a containment surface whose extent encapsulates the collective trajectories of the ions in the beam. A single ion trajectory is shown in red. Image provided by Dr. S. Rädel, TRIUMF, adapted from[25, 26].

This ellipse has an area of $A = \pi\epsilon_{\text{rms}}$, where the size parameter ϵ_{rms} is related to the extent $(x_{\text{rms}}, x'_{\text{rms}}, (xx')_{\text{rms}})$ of the distribution via:

$$\epsilon_{\text{rms}} = \sqrt{x^2_{\text{rms}} x'^2_{\text{rms}} - (xx')^2_{\text{rms}}}. \tag{2.9}$$

This geometric emittance has units of microns: Divergence x'_{rms} is typically on the scale of mrad (10^{-3}) and x in cm (10^{-2}m), with typical values for ϵ_{rms} on the order of $10\,\mu$m. Emittance plays an important role in beam optics since it relates to conservation laws, further discussed in Chapter 3. It is an observable beam parameter which measures its temperature, or internal energy. Beams with higher emittances have a higher tendency to diverge during propagation. Under changes of beam energy, while the emittance itself is not conserved, the normalized emittance is:

$$\epsilon^* = \beta\gamma\epsilon_{\text{rms}} \tag{2.10}$$

where $\beta\gamma$ here are the relativistic factors. The evolution of the beam envelope through the accelerator along a trajectory s can be expressed in terms of the functions $(\alpha(s), \beta(s), \gamma(s), \epsilon(s))$. The Twiss parameters β and γ relate to the extent of the distribution in phase space along the position and momentum axes, respectively. The rms envelope is obtained evaluating the projections of the ellipse of Eq. (2.7):

$$x_{\text{rms}} = \sqrt{\beta\epsilon_{\text{rms}}}, \tag{2.11}$$

$$x'_{\text{rms}} = \sqrt{\gamma\epsilon_{\text{rms}}}. \tag{2.12}$$

For 86% containment envelopes, four times the rms emittance is used in Eqs. (2.11) and (2.12), corresponding to an ellipse of area $A = 4\pi\epsilon_{\text{rms}}$. The ellipse's vertical orientation angle θ is related to the parameter α:

$$\tan(2\theta) = \frac{2\alpha}{\gamma - \beta}. \tag{2.13}$$

An example phase space beam distribution which is Gaussian in (x, x') is shown in Figure 2.3, with 86% containment bounds for both the position and momentum extent. The Twiss parameter ellipse from Eq. (2.7), of area $A = 4\pi\epsilon_{\text{rms}}$ is superimposed to the distribution in red in the figure.

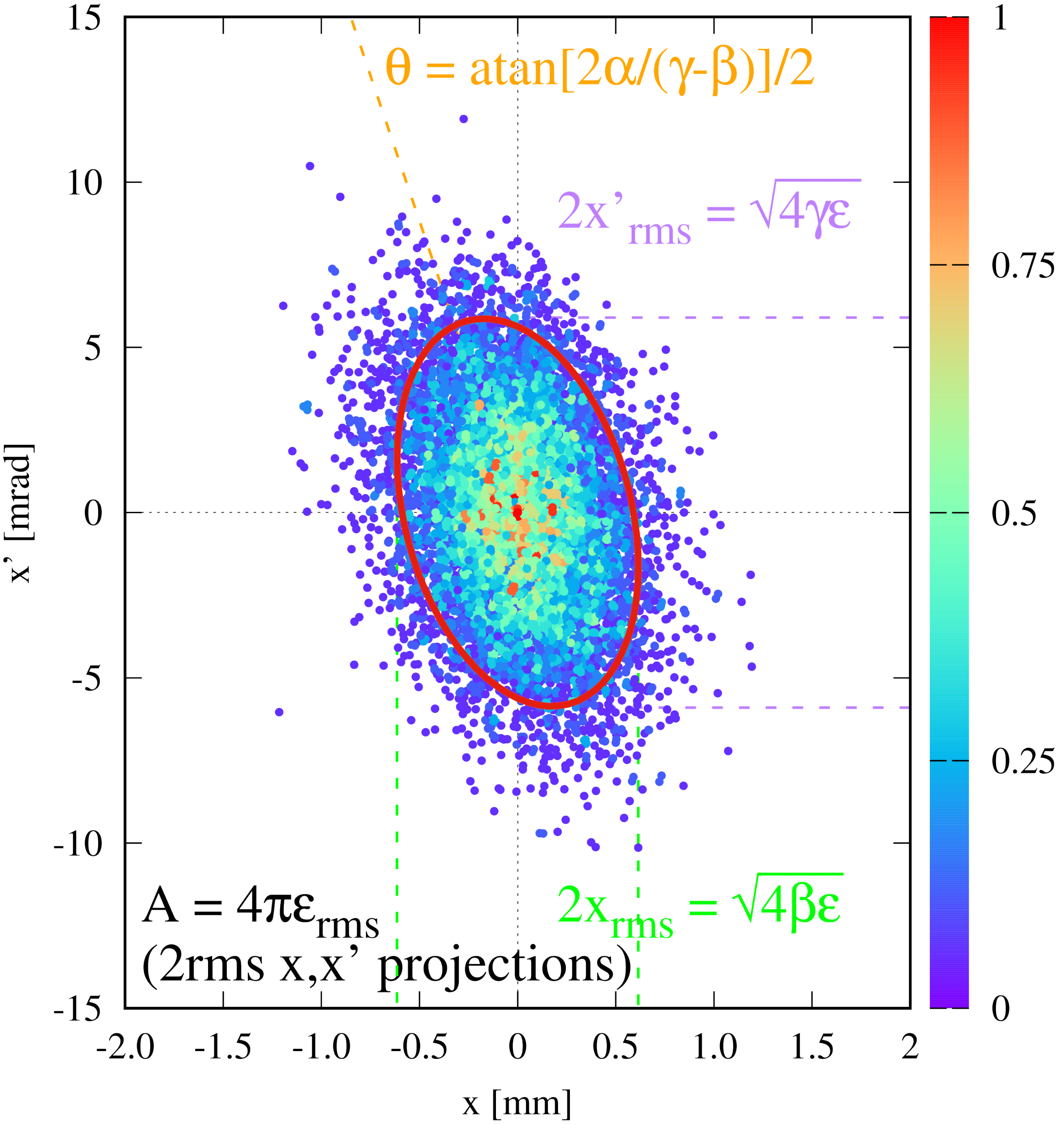

Figure 2.3: Simulated phase space transverse beam distribution showing 10^5 particles. This can be parameterized using the Courant-Snyder ellipse from Eq. (2.7). The 86% x and x' containment lines, in addition to the relationship between ellipse tilt angle and the Courant-Snyder parameters is shown. Normalized relative local particle density shown as a colormap. The ellipse tilt angle θ is measured with respect to the vertical, not horizontal axis.

2.3 Hill Differential Equation

The charged particles that form the beam individually obey the Lorentz force law:

$$\vec{\mathbf{F}} = q(\vec{\mathbf{E}} + \vec{\mathbf{v}} \times \vec{\mathbf{B}}). \tag{2.14}$$

For any particle, x and x' evolve according to these ordinary differential equations:

$$\frac{\mathrm{d}x}{\mathrm{d}s} = x' \tag{2.15}$$

$$\frac{\mathrm{d}x'}{\mathrm{d}s} = |\vec{\mathbf{F}}|. \tag{2.16}$$

Not only do single particles evolve in this manner, but so do the particles in phase space that lie directly on the line defined by the ellipse of Eq. (2.7), for a given emittance. Thus, when discussing the evolution of the 86% containment ellipse ϵ_{rms}, this is what is understood. If the forces are linear, individual particle trajectories within the ellipse do not cross the rms envelope. During its transformation through the various fields, the fraction of particles contained within the ellipse remains constant. If the electromagnetic force terms acting on the particles can be expressed as linearly dependent on the transverse position x:

$$|\vec{\mathbf{F}}| = -K(s)x, \tag{2.17}$$

where s is the Frenet-Serret trajectory along the beam axis of propagation, then Eqs. (2.15) & (2.16) can be arranged as a Hill differential equation[28]:

$$\frac{\mathrm{d}^2x}{\mathrm{d}s^2} + K(s)x = 0. \tag{2.18}$$

Provided known initial conditions, the solution of Eq. (2.18) allows for the computation of the evolution of the beam envelope, as it transits through the fields of the beamlines and accelerators. The study of a beam distribution parameterized by the Twiss parameter ellipse of Eq. (2.7) using Eq. (2.18) with fields (2.17) forms the basis of beam optics analysis for accelerators.

2.4 Matrix Optics and Common Devices

Though there are in principle a limitless number of possible designs for the devices that generate the electromagnetic forces that define beam optics, a select few compose the vast majority of what is presently used in accelerators and beamlines. The effects of those devices on a beam distribution here represented by the initial extent of its envelope in (x_i,x_i') can be handled using the formalism of transfer matrix optics. A beam optical device of nonzero length which produces a linear restoring force in accordance to (2.17) will give a solution to the Hill equation (2.18) which takes the form:

$$\begin{pmatrix} x \\ x' \end{pmatrix} = \begin{pmatrix} m_{11} & m_{12} \\ m_{21} & m_{22} \end{pmatrix} \begin{pmatrix} x_i \\ x_i' \end{pmatrix}. \tag{2.19}$$

The elements m_{ij} define the transfer matrix $\mathbf{M}$ of the system, which transforms the initial beam distribution into its final state, following transit through the field. The coefficients of $\mathbf{M}$ are obtained by solving the Hill equation (2.18) for a given $K(s)$. The simplest case for $\mathbf{M}$ is a field free drift where $K(s)$ vanishes:

$$\frac{\mathrm{d}^2x}{\mathrm{d}s^2} = 0, \tag{2.20}$$

in this case, the solution after a drift length d is trivial, obtained by twice integrating (2.20):

$$\mathbf{M_O} = \begin{pmatrix} 1 & \mathrm{d} \\ 0 & 1 \end{pmatrix}. \tag{2.21}$$

The subscript on $\mathbf{M}$ denotes absence of fields. In the case where the term $K(s)$ is linear and constant over a distance d, the Hill equation resembles:

$$\frac{\mathrm{d}^2x}{\mathrm{d}s^2} + kx = 0. \tag{2.22}$$

The general solution over this distance is a linear combination of sine- and cosine-like functions $S(l)$ and $C(l)$, where l is the length of the field along s:

$$x(l) = S(l)x_i + C(l)x_i'. \tag{2.23}$$

This produces two sets of solutions, which depend upon the sign of the parameter k. If $k > 0$, the solutions are harmonic:

$$S(l) = \frac{1}{\sqrt{k}} \sin(l\sqrt{k}), \tag{2.24}$$

$$C(l) = \cos(l\sqrt{k}), \tag{2.25}$$

while they are hyperbolic if $k < 0$:

$$S(l) = \frac{1}{\sqrt{|k|}} \sinh(l\sqrt{|k|}), \tag{2.26}$$

$$C(l) = \cosh(l\sqrt{|k|}). \tag{2.27}$$

In matrix form, the solutions are respectively[28]:

$$\mathbf{M_F} = \begin{pmatrix} \cos(l\sqrt{k}) & \frac{1}{\sqrt{k}}\sin(l\sqrt{k}) \\ -\sqrt{k}\sin(l\sqrt{k}) & \cos(l\sqrt{k}) \end{pmatrix}, \tag{2.28}$$

$$\mathbf{M_D} = \begin{pmatrix} \cosh(l\sqrt{|k|}) & \frac{1}{\sqrt{|k|}}\sinh(l\sqrt{|k|}) \\ \sqrt{|k|}\sinh(l\sqrt{|k|}) & \cosh(l\sqrt{|k|}) \end{pmatrix}. \tag{2.29}$$

The transfer matrices (2.28) & (2.29) correspond to the case of a quadrupole field which can either be magnetic or electric. Cases with $k > 0$ cause the field to focus, meaning the beam converges towards the reference particle. The field defocuses if $k < 0$, implying divergent motion away from the reference. The amplitude of the quadrupole field arises from a potential whose amplitude has the form:

$$\phi_Q = \frac{k}{2}(x^2 - y^2). \tag{2.30}$$

A fundamental feature of quadrupoles is that they focus in one dimension while defocusing in the other. This is ultimately a consequence of Poisson's equation for free space:

$$\nabla^2 \phi = 0 \tag{2.31}$$

for which the potential (2.30) is a solution. For this reason, transport systems are usually constructed with sequential quadrupoles of alternating polarity. This balances the focusing and defocusing effects to the beam distribution, keeping the envelope under control. In practice, use of electrostatic quadrupoles is typical in low energy sections for nonrelativistic beams, while magnetic quadrupoles are used in medium and high energy beamlines, where β (velocity) is non-negligible. As a result, low energy sections typically operate electrostatic quadrupoles with electrodes at up to a few kilovolts, while high energy beamlines employ magnetic quadrupoles with currents typically in the range of dozens of amperes. In either case, the constant k in Eq. (2.30) takes on different definitions:

$$k_e \approx \frac{V_Q}{a^2 V_0}, \tag{2.32}$$

$$k_m = \frac{B'}{B\rho}. \tag{2.33}$$

The nonrelativistic limit is shown for k_e, V_Q is the quadrupole electrode voltage, V_0 is the beam extraction voltage and a is the quadrupole aperture[29]. For the magnetic case, k_m, B' is the field gradient and the denominator corresponds to the beam rigidity $(B\rho)$. The focal length of quadrupoles with transfer matrices (2.28) or (2.29) can be found by allowing $l \to 0$ while holding the product kl constant, which produces a thin lens approximation:

$$\lim_{l \to 0} \mathbf{M_F} = \begin{pmatrix} 1 & 0 \\ -kl & 1 \end{pmatrix}, \tag{2.34}$$

$$\lim_{l \to 0} \mathbf{M_D} = \begin{pmatrix} 1 & 0 \\ kl & 1 \end{pmatrix}, \tag{2.35}$$

where the product kl is held constant for both limits. The transfer matrices (2.34) and (2.35) are identical to that of a lens in ray optics:

$$\mathbf{M}_{\pm} = \begin{pmatrix} 1 & 0 \\ \mp\frac{1}{f} & 1 \end{pmatrix} \tag{2.36}$$

implying the focal length of thin electromagnetic quadrupoles arising from the potential (2.30) is:

$$f = \frac{1}{kl}, \tag{2.37}$$

where the strength parameter k is either from Eqs. (2.32) or (2.33) depending on the nature of the field. An object, in this case a beam distribution at a position s_0 will be imaged by a quadrupole at a point s_1 according to the thin lens equation:

$$\frac{1}{s_0} + \frac{1}{s_1} = \frac{1}{f}. \tag{2.38}$$

In addition, the net focal effect upon the beam of two adjacent quadrupoles with foci f_1 and f_2 is:

$$\frac{1}{f} = \frac{1}{f_1} + \frac{1}{f_2} \tag{2.39}$$

which assumes the lenses are exactly adjacent. In the more realistic event that they are separated by a drift, the resulting arrangement is referred to as a FODO cell, since it consists of a focusing quad (F), a defocusing quad (D) separated by drifts (O). Groups of FODO cells, also referred to as doublets can be used to achieve periodic transport of a beam, as shown in Figure 2.4. The compound transfer matrix of a single doublet is:

$$\mathbf{M}_{FODO} = \mathbf{M}_O\mathbf{M}_D\mathbf{M}_O\mathbf{M}_F \tag{2.40}$$

and the condition for periodic transport can be expressed as:

$$\begin{pmatrix} x_i \\ x_i' \end{pmatrix} = \mathbf{M}_{FODO} \begin{pmatrix} x_i \\ x_i' \end{pmatrix}. \tag{2.41}$$

The matrix (2.40) is obtained using the transfer matrices of the FODO components in Eqs. (2.28), (2.29) and (2.21), meaning an analytic solution can be found for (2.41). Such an analysis is at the heart of beam transport and tune design.

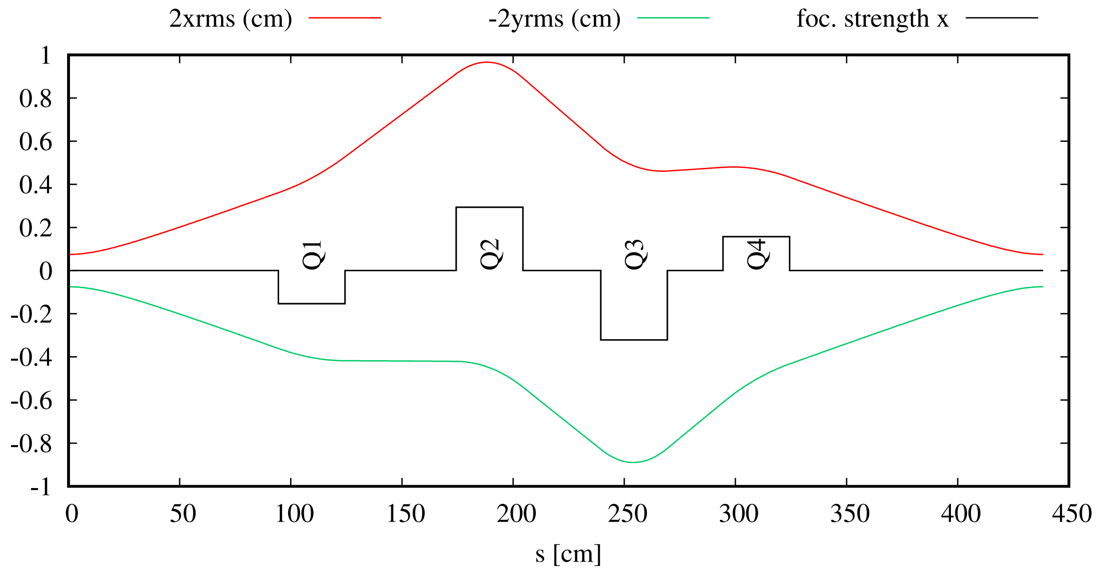

Figure 2.4: 2 rms (x, y) containment envelopes for a beam of $^{14}\mathrm{N}^{+}$ at an energy of 21 MeV ($\beta = 5.6\%$). The beamline sequence consists of two successive FODO cells, or quadrupole doublets, which have been tuned to produce a focus-to-focus condition, imaging the starting beam distribution at the endpoint of the axis s. The horizontal (x) relative focal strength of each device is shown in black, indicating the quadrupole locations. The vertical (y) envelope is shown as negative for neatness of plotting.

2.5 Dispersion and Chromaticity

When a single charged particle transits through a static and uniform magnetic field in a vacuum, the resulting trajectory is circular per the Lorentz Force law (2.14). The same situation but with a population of ions distributed about a reference particle with an inherent energy spread will cause dispersion: Particles with above or below average beam velocity will have trajectories with different radii of curvature through the field. This is problematic for the use of downstream optics, for example quadrupoles whose focal strengths per Eqs. (2.32) and (2.33) depend on the beam velocity. In the electrostatic case this dependence is indirect through the beam extraction voltage, while in the magnetic case, the rigidity of a beam is a measure of its momentum via:

$$B\rho = \frac{P_0}{q}, \tag{2.42}$$

where q is the charge. In both cases, the dispersion can be treated via Hill's equation, by adding a momentum dependent term[30]:

$$\frac{\mathrm{d}^2 x(s)}{\mathrm{d}s^2} + K(s)x(s) = \frac{1}{\rho(s)}\frac{\Delta P(s)}{P_0}. \tag{2.43}$$

P_0 and $\Delta P(s)$ are the reference particle momentum and the bunch momentum spreads, respectively and $\rho(s)$ is the reference radius of curvature through the field. This inhomogeneous form of Hill's equation generates an additional term which is linearly added to the homogeneous solution x_0:

$$x(s) = x_0 + D(s)\frac{\Delta P(s)}{P_0}. \tag{2.44}$$

The function $D(s)$ has the definition:

$$D(s) = \frac{\Delta x(s)}{(\Delta P(s)/P_0)} \tag{2.45}$$

and quantifies the dispersion of the beam. It is a ratio of the lateral deflection $\Delta x(s)$ that an off-momentum particle with $P(s) = P_0 + \Delta P(s)$ experiences after a bending field, whether electric or magnetic. The units of $D(s)$ are that of size, typically meters or centimeters. Once the dispersion is nonzero in a beam, it will evolve per:

$$\frac{\mathrm{d}^2}{\mathrm{d}s^2}D(s) + K(s)D(s) = \frac{1}{\rho}, \tag{2.46}$$

whose solution has the form:

$$D(s) = S(s)\int_0^s \frac{C(\chi)}{\rho(\chi)}\mathrm{d}\chi - C(s)\int_0^s \frac{S(\chi)}{\rho(\chi)}\mathrm{d}\chi. \tag{2.47}$$

The improper integrals in Eq. (2.47) involve functions $S(s)$ and $C(s)$ which are sine and cosine functions if $K(s) > 0$ and are hyperbolic otherwise. As an example, a dipole bending magnet's vertical magnetic field lines disperse the beam horizontally, resulting in $K(s) = 1/\rho^2$, where ρ is the radius of curvature of the reference particle. The transfer matrix of such a dipole, per Eq. (2.28), the linear $K(s)$ solution to Hill's equation, is[28]:

$$\mathbf{M_{Dip}} = \begin{pmatrix} \cos\frac{l}{\rho} & \frac{1}{\rho}\sin\frac{l}{\rho} \\ -\frac{1}{\rho}\sin\frac{l}{\rho} & \cos\frac{l}{\rho} \end{pmatrix}. \tag{2.48}$$

The corresponding value of the dispersion and its first derivative are, for a dipole:

$$D(s) = \rho\big(1 - \cos\frac{l}{\rho}\big) \tag{2.49}$$

$$D'(s) = \sin\frac{l}{\rho}. \tag{2.50}$$

A beam following a trajectory s, for which:

$$D(s) = 0, \tag{2.51}$$

$$D'(s) = 0, \tag{2.52}$$

is free of dispersion and will maintain this condition until it interacts with a dispersive element, such as a dipole. Quadrupole lenses which are used to transversely focus or defocus the beam will not initiate dispersion, though if it is nonzero prior to transiting through the quadrupole, there will result a change in the focal effect upon the beam, which in turn will change the dispersion. This takes place because the high and low energy sides of the beam will possess separate foci.

The condition where the focal length of optical devices is spread across a region $f \pm \Delta f$ is known as chromaticity[30, 31], arising from the Greek *chromos* for color, denoting energy dependent focal effects. In a charged particle beam, this is unwanted as it degrades the ability to precisely control its envelope. The Twiss ellipse of Eq. (2.7) assumes uncorrelated transverse and longitudinal distributions. If the dispersion is nonzero but is not accounted for, the Twiss parameter fit for $(\alpha, \beta, \gamma, \epsilon)$ will not represent the true beam distribution, which will have underlying correlations between (x, x') and $(z, \Delta P)$. The evolution of the fitted, dispersion free ellipse will be found not to agree with the measurable beam distribution downstream; control of the beam has been lost. To counteract this, it is possible to pair quadrupoles with dispersive elements to produce a net arrangement which will be fully achromatic with $D(s) = D'(s) = 0$. Thus, to maintain control of the beam, it is desired to keep it doubly achromatic, meaning tunes including bend segments are typically designed with this condition in mind.

2.6 Nonlinearities and Mismatches

The devices discussed thus far have been represented by idealized fields producing linear forces. In reality, this would require electrodes of infinite length[32]. In practice, devices have higher than first order dependency, though their design is aimed at suppressing, as much as possible, higher order contributions near-axis. As an example, a quadrupole with imperfect electrode shapes can be represented by a potential[33]:

$$\phi_Q = \frac{k}{2}(x^2 - y^2) - \frac{k''}{24}(x^4 - y^4) + \frac{k''''}{720}(x^6 - y^6) - \cdots \tag{2.53}$$

Forces generated from the gradient of (2.53) inherit coordinate dependencies as illustrated in Figure 2.5. While the linear contribution is dominant for small transverse displacements from the beam axis, as the distance increases higher order contributions may grow significantly. In this case, the forces acting upon the bunch become nonlinear, which introduces distortions in the phase space distribution of the particles. In Figure 2.6, a simulated third order distortion has been introduced to an initial distribution represented by the red ellipse. The net effect of the distortion is to increase the emittance of the distribution by way of filamentation. As a consequence,

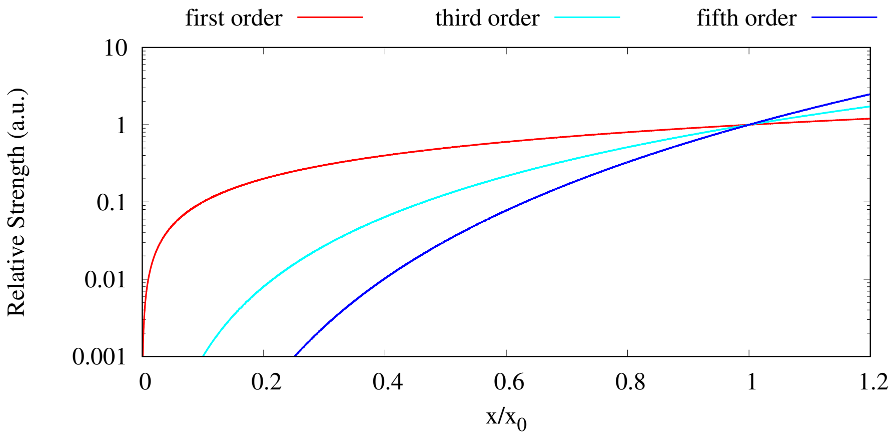

Figure 2.5: Relative contribution of the linear, third order and fifth order coordinate dependencies from the forces arising from the gradient of the potential (2.53). The coordinate x/x_0 measures the transverse displacement away from the Frenet-Serret trajectory s. The point x_0 here illustrates the transverse position where first, third and fifth order are of equal strength. Good accelerator tunes aim to keep the transverse envelope contained in the region where only first order terms dominate.

when one recomputes the Twiss parameter fit, the purple ellipse is obtained. Particles furthest away from the dense core of the beam will no longer follow the intended linear evolution through phase space and can be expected to inherit further nonlinearities, increasing the emittance still. The distribution shown in Fig. 2.6 is mismatched with respect to the design assumption (red ellipse) and will likely suffer from transmission

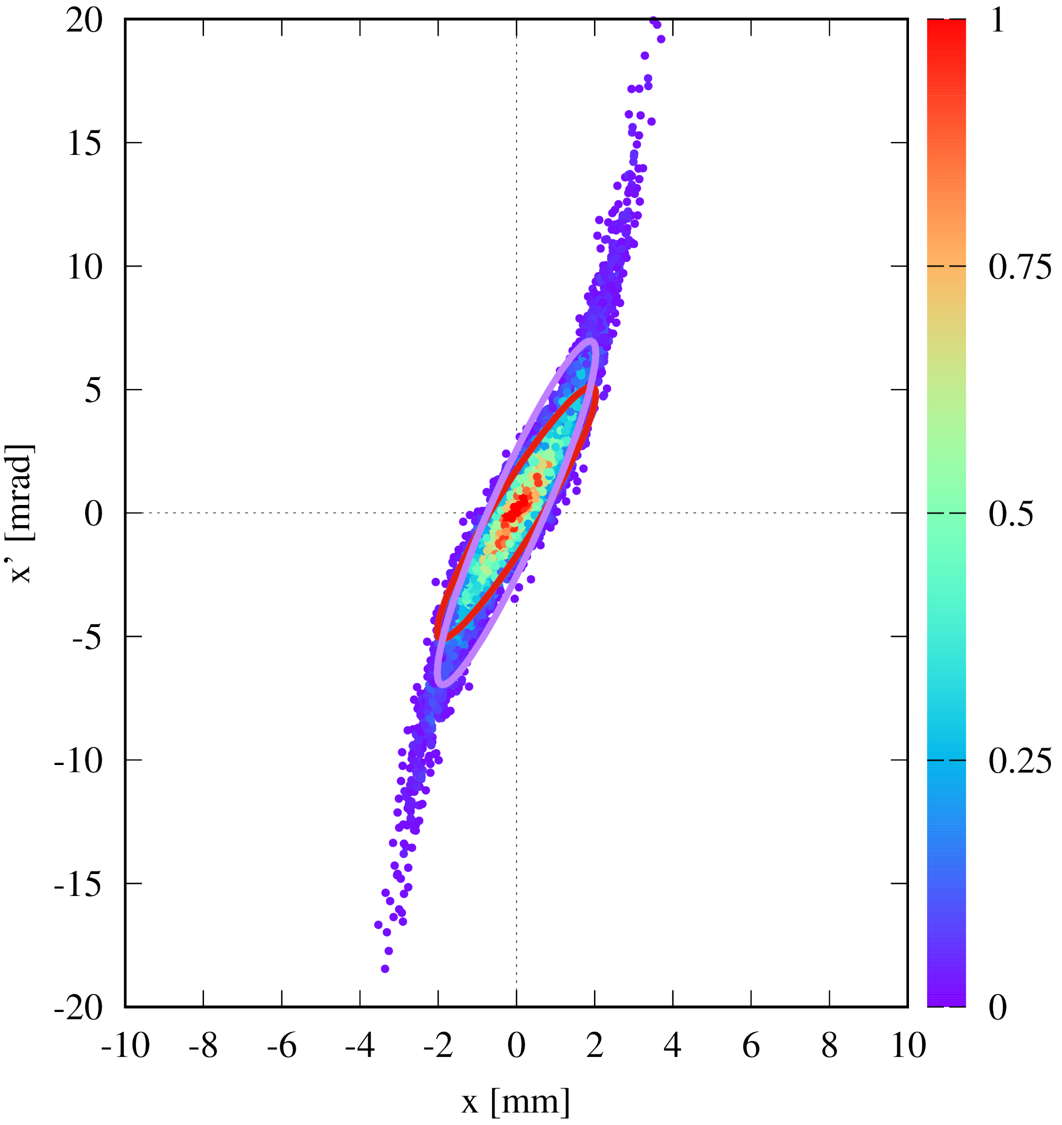

Figure 2.6: An original phase space beam distribution represented by the red ellipse has suffered a third order aberration, resulting in the displayed particle density distribution. The perturbed distribution is fit to an ellipse per Eqs. (2.7) and (2.9), resulting in a mismatch condition in the tune. Normalized local particle density shown as a colormap.

losses downstream as extremal particles collide with apertures. Bovet[34] defines a mismatch parameter[1] $\mathcal{D}$ for two ellipses described by Twiss parameters according to Eq. (2.7):

$$\mathcal{D} = \frac{1}{2}(\beta_2\gamma_1 + \gamma_2\beta_1 - 2\alpha_1\alpha_2). \tag{2.54}$$

Looking back at the Twiss parameter ellipse from Eq. (2.8), this produces a value of exactly $\mathcal{D} = 1$ for maximum overlap: $(\alpha_1, \beta_1, \gamma_1) = (\alpha_2, \beta_2, \gamma_2)$. For the special case of two ellipses of common area S, centered at the same point, whose orientations and semi-axes may differ, the common overlap area S_C is:

$$\frac{S_C}{S} = \frac{4}{\pi}\sqrt{\arctan(\mathcal{D} - \sqrt{\mathcal{D}^2 - 1})}. \tag{2.55}$$

which is unity if $\mathcal{D} = 1$ and decreases asymptotically towards zero as the mismatch parameter increases. The formulas (2.54) and (2.55) allow for the quantification of a tune mismatch, providing a minimizable parameter for optimization computations[13]. In Figure 2.7, a general transformation error is shown. It is assumed that the quadrupole from Eq. (2.28), possessing an unknown strength parameter error, should transform (**P1**,**P2**) into (**P1'**, **P2'**), but the result is actually (**E1**, **E2**). These depend in turn on the error upon the strength parameter k, but they both scale with the phase space coordinates. The more eccentric distribution (Fig. 2.8, red), in presence of a field error, overlaps less of the tune assumption than the rounder distribution (same fig., blue).

In practice, observation of a mismatch condition as in Figure 2.6 at a beam diagnostic would require corrective tuning. This intervention would aim to restore the desired beam profile (red ellipse). However, such aberrations cannot be undone without resorting to specialized corrective optics such as sextupole magnets, which can reverse the third order effect. Should such a device not be available, the only way to avoid mismatches arising from nonlinearities is to ensure the beam envelope remains confined to the region near-axis, where the dominant effects are linear and higher order contributions are suppressed. The added criterion of keeping envelopes confined to this region is an important consideration when computing and analyzing beams and tunes through beamlines and accelerators.

---

[1] In this dissertation, Bovet's parameter $\mathcal{D}$ is presented in cursive to differentiate it from the beam dispersion D.

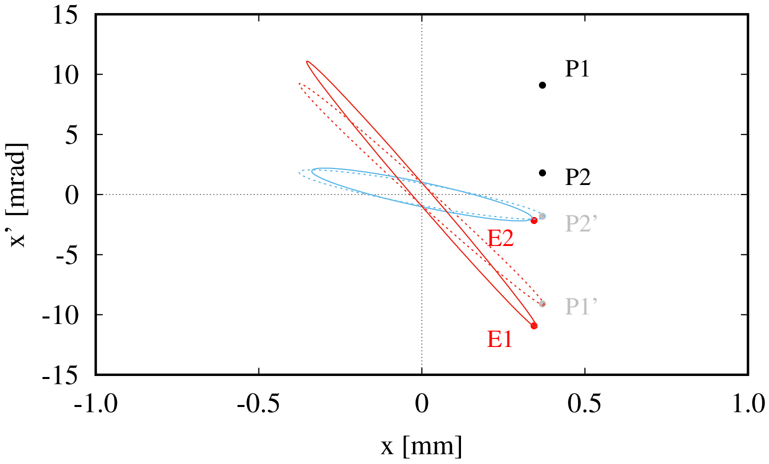

Figure 2.7: Input ellipses whose points furthest from the origin are **P1** and **P2** have been transformed by a quadrupole with a field error. The tune assumption is that (**P1**,**P2**) are transformed to (**P1'**,**P2'**), but in reality they have been transformed into (**E1**,**E2**).

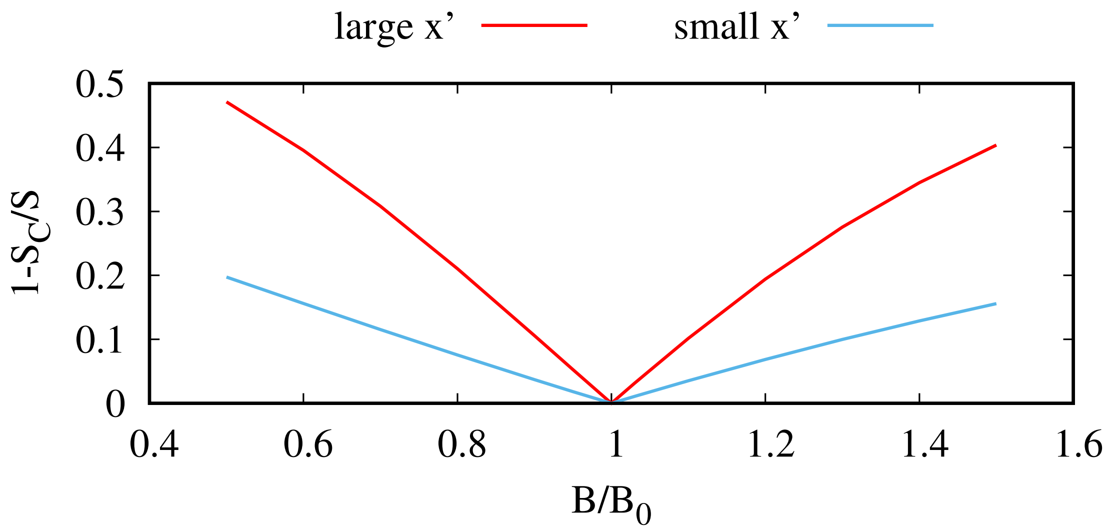

Figure 2.8: Ratio of area overlap between actual and expected ($B = B_0$) ellipses after transformation through a quadrupole with a field error $B = B_0 + \Delta B$. The x-axis shows the quadrupole field normalized to the tune expectation, while the y-axis values are that of Eq. (2.55). For a given emittance, distributions with a larger value of Twiss-α for a given β-function are more sensitive to such errors. Distributions which are less eccentric and inclined (small x') will suffer from lesser mismatches.

2.7 Energy Gain and Transit Times

Assuming the electric field through which the beam travels has a longitudinal component, this will change the particles' kinetic energy. The magnetic field does not contribute to energy gain, though magnetic fields will cause deflection per Eq. (2.14). For this reason, accelerating structures are typically designed to minimize the influence of the magnetic field near to the beam axis. The energy of each particle after transit through a field of length $2L$, symmetric about $s = 0$ is:

$$E(s) = E_0 + q\int_{-L}^{L} E_z(s, t(s))\mathrm{d}s, \tag{2.56}$$

where $E_z(s, t(s))$ is the time-dependent longitudinal component of the electric field along the reference trajectory. As the beam has a nonzero extent in phase space, each particle therefore experiences slightly different conditions during field transit. From this results a time and energy spread in the positions and momenta of particles exiting the field, which must be kept under control to avoid transmission losses. In practice, the longitudinal bunch length is kept small compared to $\beta\lambda$, where λ is the rf wavelength of the field and β is the velocity. This minimizes nonlinearities arising from either the spatial or time-dependent components of the accelerating field. This electric field $E_z(s, t(s))$ of length $2L$ is spatially symmetric about a central point and has the boundary conditions $E_z(\pm\infty) = 0$, such that it causes an energy gain:

$$\begin{aligned}
\Delta E &= q\int_{-L}^{L} E_z(s, t(s))\mathrm{d}s && (2.57)\\
&= q\int_{-L}^{L} E_z(s)\cos(\omega t(s) + \phi)\mathrm{d}s && (2.58)\\
&= q\int_{-L}^{L} E_z(s)\Bigg(\cos(\omega t(s))\cos\phi - \sin(\omega t(s))\sin\phi\Bigg)\mathrm{d}s. && (2.59)
\end{aligned}$$

The Transit Time Factor (TTF), usually denoted T[27] is an efficiency ratio arising from the consequence that during transit through the field, the time variation of $E_z(s, t(s))$ causes the energy gain to be less than if the field had been time-independent:

$$\Delta E = qT\cos\phi\int_{-L}^{L} E_z(s)\mathrm{d}s, \tag{2.60}$$

where the transit time factor is defined as:

$$T = \frac{\int_{-L}^{L} E_z(s)\cos(\omega t(s))\mathrm{d}s}{\int_{-L}^{L} E_z(s)\mathrm{d}s} - \tan\phi \frac{\int_{-L}^{L} E_z(s)\sin(\omega t(s))\mathrm{d}s}{\int_{-L}^{L} E_z(s)\mathrm{d}s}. \tag{2.61}$$

If the field $E_z(s)$ is even about a central point[27], the second term in Eq. (2.61) vanishes due to the odd nature of the sine function. In this case, the TTF is:

$$T = \frac{\int_{-L}^{L} E_z(s)\cos(\omega t(s))\mathrm{d}s}{\int_{-L}^{L} E_z(s)\mathrm{d}s}. \tag{2.62}$$

Equation (2.62) renders explicit that T is an efficiency factor bounded in [-1,1]. For maximum energy gain at a given field intensity $E_z(s)$, it is necessary to maximize the integral in the numerator, which means changing the field's amplitude or phase. Use of the TTF in turn allows to express the energy gained as:

$$\Delta E = qV_0 T\cos\phi. \tag{2.63}$$

The quantity V_0 is the integral term in Eq. (2.60), which when multiplied by the transit efficiency T is an effective voltage that the particle experiences transiting the gap. This accounts for the diminished accelerating efficiency due to the rf time dependency of the field. Computing ΔE using Eq. (2.63) avoids the need to constantly solve for $t(s)$, which increases the complexity of the problem. The advantage of using the TTF is that it only requires a single evaluation of $t(s)$ for the reference particle in a given field, to find the value of T.

2.8 Multigap Accelerating Fields

An example of an electric field whose effect upon a beam is well represented by the TTF approach is that of a two gap resonant rf cavity[35], shown in Figure 2.9, including its on-axis electric field $E_z(s)$. This cavity belongs to the ISAC SCRF booster[36], whose output beam energy is operationally computed using Eq. (2.63). Since the cavity is formed of two gaps of identical length L, the electric field can be separated evenly about a middle point, meaning T will be expressible as Eq. (2.62).

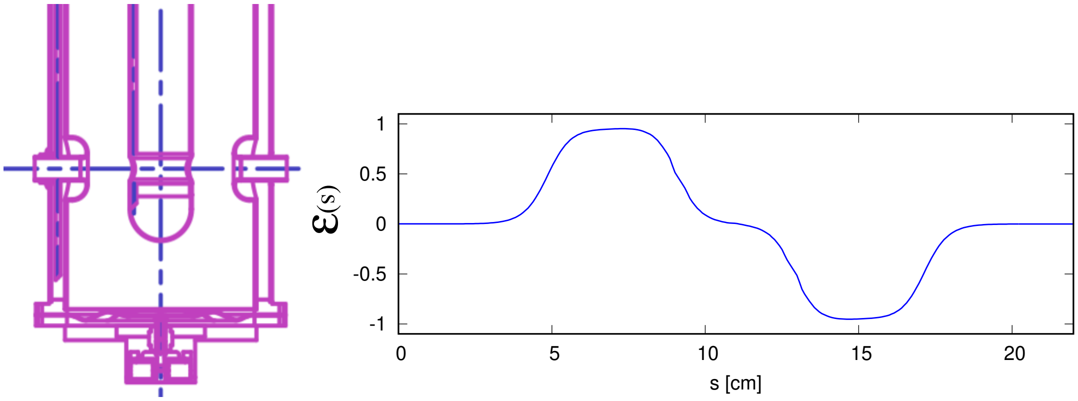

Figure 2.9: **Left:** Example cutaway of a two gap resonant rf cavity. The geometric centerpoint is indicated with the dotted blue lines. Beam propagates along the blue horizontal line. The central pillar of the cavity is electrically grounded, so are the exterior walls. **Right:** Normalized values of $E_z(s)$ denoted $\mathcal{E}(s)$ on-axis through the cavity. Drawing obtained from TRIUMF Design Office. Field data obtained from R. Laxdal, TRIUMF.

The energy gain ΔE across the both gaps will be:

$$\Delta E_{2\text{gap}} = \Delta E_1 + \Delta E_2, \tag{2.64}$$

$$= qV_0T_1\cos\phi_1 + qV_0T_2\cos\phi_2. \tag{2.65}$$

The effective voltage V_0 across each gap is identical for the cavity in Fig. 2.9. Moreover, the energy gain in each gap is small enough to apply a constant energy approximation, in which the reference particle velocity is assumed to be constant[27, 37], meaning $T_1 \approx T_2 = T_{\text{gap}}$:

$$\Delta E_{2\text{gap}} \approx 2qV_0T_{\text{gap}}\cos\phi, \tag{2.66}$$

with T_{gap} evaluated across a single cavity gap. Operators control the cavity field amplitude, which scales V_0, in addition to the rf phase ϕ. In this case, computing the transit time factor is advantageous, since one can then obtain the cavity output beam energy without evaluating differential equations, beyond finding T_{gap} once. About this last point, Wangler writes[27]:

”The phase and the transit-time factor depend on the choice of the origin. It is convenient to simplify the transit-time factor, and remove its dependence on the phase, by choosing the origin at the electrical center. [the longitudinal electric field] *is usually at least approximately an even function about a geometric center of the gap.”*

If the total number of gaps in the cavity increases, the factors T across each gap can start to appreciably differ. Multi-gap cavities may also feature variable gap lengths, meaning the electric field $E_z(s)$ across each gap will also differ in profile, compromising the simplicity of the TTF's behaviour. Such a field is shown in Figure 2.10, corresponding to a 9 gap accelerating cavity belonging to the ISAC-DTL[38]. For the aforementioned reasons, operational DTL energy change computations cannot make use of Eq. (2.66). In this case, or more generally for an n-gap cavity:

$$\Delta E_{\text{ngap}} = q \sum_{i=1}^{n} V_i T_i \cos \phi_i. \tag{2.67}$$

The behaviour of the above energy gain can become quite complicated, since a change of initial phase ϕ_1 or of effective voltage amplitude V_1 for the first gap may cause a considerable change in the profile of $t(s)$ downstream. Evaluation of Eq. (2.67) requires solving the full TTF from Eq. (2.61), or referring to pre-computed single gap factors and adding them. Despite this, the TTF approach produces a discontinuous energy gain, which is unphysical! To obtain the continuous evolution of the beam energy along a cavity such as Fig. 2.10, one must solve:

$$E(s) = E_0 + q \int E_z(s) \cos(\omega t(s) + \phi) \mathrm{d}s, \tag{2.68}$$

whose solution depends on the field amplitude, ϕ and $t(s)$. Figure 2.11 shows reference particle velocity profiles through the aforementioned field. The starting rf phase is identical, but different field scaling parameters $V_S1 < V_S2 < V_S3$ have been used, demonstrating the cavity's nonlinear output velocity response. Simulating continuous beam envelopes undergoing energy gain within such cavities requires making use of a method which is capable of efficiently solving the equations of motion for relativistic charged particles, obtaining $t(s)$ which in turn will enable evaluation of Eq. (2.68).

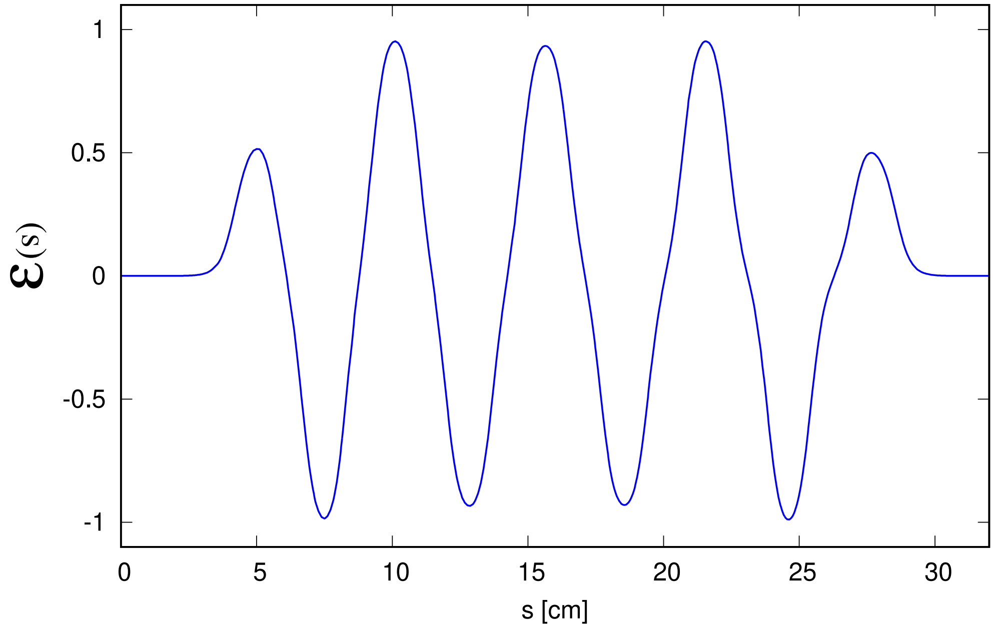

Figure 2.10: Simulated normalized $E_z(s)$ field denoted $\mathcal{E}(s)$ for the first multigap accelerating cavity of the ISAC-DTL. The cavity consists of nine separate gaps with an operational design input E/A of 0.153 MeV/u and an output E/A of 0.238 MeV/u. Normalization of the field intensity to the maximum value in the set bounds the function to [-1,1], allowing for the use of a scaling parameter to represent changes of rf amplitude.

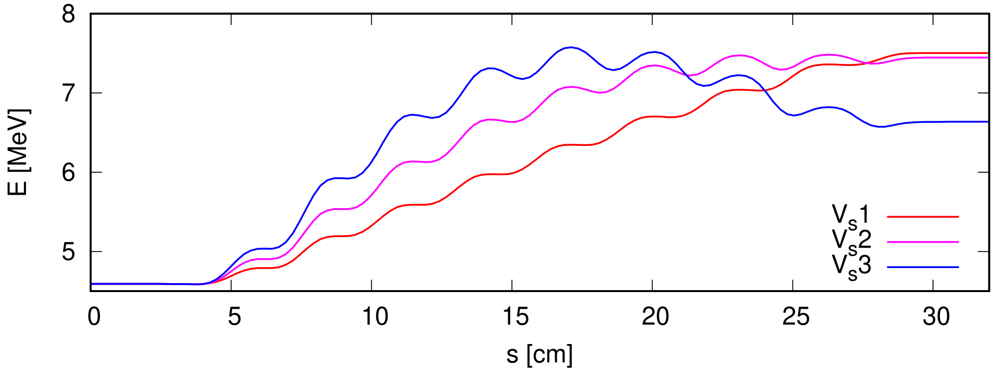

Figure 2.11: Reference particle energy profiles through the first ISAC-DTL accelerating field (Fig. 2.10), at three on-axis field scaling factors $V_s1 < V_s2 < V_s3$ and identical ϕ_0. The cavity output energy is nonlinear to field scaling, with in this case the lowest on-axis scaling factor producing the greatest output reference particle energy. Larger initial acceleration causes progressive phase slippage along the structure, eventually leading to considerable deceleration forces, which reduces the output energy.

Chapter 3

Hamiltonian Envelope Dynamics and `TRANSOPTR`

Originally developed at Chalk River Nuclear Laboratories by Hutcheon & Heighway in the late 70's[39] `TRANSOPTR` is a first order transport code based upon the sigma matrix formalism developed by Brown[40] and Sacherer[41]. The Courant-Snyder Hamiltonian[42] for a relativistic charged particle is used to track the evolution of the rms envelopes through the fields of the accelerator. Since its initial development, it has been extensively developed and adapted for usage at TRIUMF, by Baartman *et al*[13]. Over decades of development, the TRIUMF Beam Physics department has extended `TRANSOPTR` to allow inclusion of various facilities including the 520 MeV cyclotron injection line and inflector[43]. The code has also been used to model and study the newer TRIUMF electron linac and transport lines[44]. `TRANSOPTR` notably avoids use of transit time factor approximations, instead directly integrating the energy gain from the field. However, as a result of various historical and practical development realities, the code was never fully extended to cover the ISAC linear accelerators. This chapter presents the Hamiltonian formalism employed by `TRANSOPTR` and the infinitesimal transfer matrices that are needed to compute beam envelopes in the ISAC linear accelerator. As part of this work, `TRANSOPTR` was further extended with an RFQ capability and published in *Physical Review Accelerators and Beams*[14], which is presented in Section 3.7. Additionally, the envelope code's DTL simulation, a novel application, was implemented using the axial electric field capability shown in Section 3.6.

3.1 Courant-Snyder Hamiltonian and Beam Matrix Formalism

A general, time dependant electromagnetic field is represented by the effect of both a scalar and vector, ϕ and $\vec{A}$, both functions of space and time. In the Frenet-Serret coordinate system, the equations of motion for relativistic massive particles transiting such fields are obtained with the Courant-Snyder Hamiltonian[42], with independent variable s[45]:

$$H_s = -qA_s - \left(1 + \frac{x}{\rho}\right)\sqrt{\left(\frac{E - q\phi}{c}\right)^2 - m^2c^2 - (P_x - qA_x)^2 - (P_y - qA_y)^2}, \quad (3.1)$$

where the vector potential has been decomposed into its three constituent spatial components, while the scalar potential is subtracted directly from the canonical energy E. The particle is assumed to have mass m and charge q, while c is the speed of light in a vacuum. In the case of a linear accelerator, $\rho = \infty$. The Hamiltonian (3.1) provides information for a single reference particle around which the Frenet-Serret frame is built, however it is desired to understand the evolution of the beam distribution, composed of countless particles. First consider the six phase space coordinates for a single particle in column vector form:

$$\mathbf{X} = \left(x, P_x, y, P_y, z, P_z\right)^T. \quad (3.2)$$

The phase space coordinate of each particle in the ensemble is represented by a state-vector of the form in Eq. (3.2). The first order moments produce the centroids of the distribution with N particles:

$$\langle \mathbf{X} \rangle = \frac{1}{N}\sum_{n=1}^{N} \mathbf{X}. \quad (3.3)$$

Second moments are defined by the covariance matrix, which is commonly denoted as $\boldsymbol{\sigma}$. It is also referred to in accelerator physics as the beam matrix. Assuming the first moments are zero, the matrix $\boldsymbol{\sigma}$ is defined as:

$$\boldsymbol{\sigma} \equiv \frac{1}{N}\sum_{n=1}^{N} \mathbf{X}\mathbf{X}^{T}, \tag{3.4}$$

with the superscript T here denoting transposition. For example, if the phase space distribution function is f, the $\boldsymbol{\sigma}$-matrix element σ_{11} is defined as:

$$\sigma_{11} = \int \cdots \int_{V_6} x^2 f(x, P_x, y, P_y, z, P_z)\mathrm{d}x \cdots \mathrm{d}P_z \tag{3.5}$$

with the integration spanning the extent of the six canonical phase space coordinates. Obtaining values for the $\boldsymbol{\sigma}$-matrix at each step along the reference particle's trajectory will provide a description of the rms values of the beam envelopes. `TRANSOPTR` is a linear envelope code, meaning it can evaluate Hamilton's equations of motion:

$$x' = \frac{\partial H}{\partial P_x}, \tag{3.6}$$

$$P_x' = -\frac{\partial H}{\partial x}, \tag{3.7}$$

to first order in the canonical coordinates, only. Knowing that these equations themselves involve first order derivatives of a Hamiltonian, using one with up to second order coordinate dependence will produce the linear component of the motion. For this, the Hamiltonian (3.1) is expanded in a series up to second order:

$$H_s = H_0 + \sum_i \frac{\partial H}{\partial x_i}\Big|_0 x_i + \frac{1}{2}\sum_{i,j} \frac{\partial^2 H}{\partial x_i \partial x_j}\Big|_0 x_i x_j + ... \tag{3.8}$$

where the summation indices i, j are over the 6 canonical coordinates. The constant term H_0 vanishes upon evaluation of first order derivatives. In the co-moving Frenet-Serret frame, the first order term corresponds to the motion of the reference particle. Setting these to zero means the reference particle is always on the optical axis of symmetry. With this choice, the Hamiltonian describing the particle distribution is only dependent upon the second order terms of $x_i x_j$, which correspond to the second moments in the beam matrix $\boldsymbol{\sigma}$. The Hamiltonian now has the form:

$$H_s = Ax^2 + BxP_x + Cxy + DxP_y + ... + KP_z^2. \tag{3.9}$$

The linear coefficients contain the second order partial derivatives of the Hamiltonian in Equation (3.8). After evaluating Hamilton's equations on the above, the resulting system of equations can concisely be expressed as:

$$\frac{\mathrm{d}\mathbf{X}}{\mathrm{d}s} = \mathbf{F}(s)\mathbf{X}, \tag{3.10}$$

where $\mathbf{X}$ is the column vector from Equation (3.2) and the matrix $\mathbf{F}(s)$, also known as the infinitesimal transfer matrix[45], contains the second derivative terms:

$$\mathbf{F}(s) = \begin{pmatrix} \frac{\partial^2 H}{\partial P_x \partial x} & \frac{\partial^2 H}{\partial P_x^2} & \cdots & \frac{\partial^2 H}{\partial P_x \partial P_z} \\ -\frac{\partial^2 H}{\partial x^2} & -\frac{\partial^2 H}{\partial x \partial P_x} & \cdots & -\frac{\partial^2 H}{\partial x \partial P_z} \\ \frac{\partial^2 H}{\partial P_y \partial x} & \frac{\partial^2 H}{\partial P_y \partial P_x} & \cdots & \frac{\partial^2 H}{\partial P_y \partial P_z} \\ -\frac{\partial^2 H}{\partial y \partial x} & -\frac{\partial^2 H}{\partial y \partial P_x} & \cdots & -\frac{\partial^2 H}{\partial y \partial P_z} \\ \frac{\partial^2 H}{\partial P_z \partial x} & \frac{\partial^2 H}{\partial P_z \partial P_x} & \cdots & \frac{\partial^2 H}{\partial P_z^2} \\ -\frac{\partial^2 H}{\partial z \partial x} & -\frac{\partial^2 H}{\partial z \partial P_x} & \cdots & -\frac{\partial^2 H}{\partial z \partial P_z} \end{pmatrix}. \tag{3.11}$$

In all, there are 36 equations, involving the set of all second order partial derivatives of H_s with respect to the 6 canonical coordinates. Due to the symmetry of mixed partial derivatives, there are 21 independent terms in $\mathbf{F}(s)$. Two supplemental equations must be solved for energy and time:

$$\frac{\mathrm{d}E_0}{\mathrm{d}s} = \frac{\partial H}{\partial t}, \tag{3.12}$$

$$\frac{\mathrm{d}t_0}{\mathrm{d}s} = -\frac{\partial H}{\partial E} = \frac{E_0}{P_0} = \frac{1}{\beta_0 c}, \tag{3.13}$$

bringing the total to 23. It is also important to note that scalar potential ϕ directly modify the canonical definition of the energy, to first order:

$$c^2 P\Delta P = \big(E - q\phi\big)\Delta E. \tag{3.14}$$

This treatment enables the straightforward integration of the reference particle energy from the longitudinal component of a longitudinal electric field over a distance $[0, L]$:

$$E(s) = E_0 + q\int_0^L E_Z(s)\cos(\omega t(s) + \phi_0)\mathrm{d}s. \tag{3.15}$$

Here, $\mathrm{E}_Z(s)$ is the z-component of the electric field arising from ϕ. Importantly, this means that the case of linear accelerators can be treated directly from the fields, without resorting to a transit-time factor approximation. This is advantageous since it allows for a simulation which accepts as input parameters both the field scaling amplitude and the rf phase, the same tuning parameters of an rf cavity. The evolution along the Frenet-Serret reference orbit of the $\boldsymbol{\sigma}$-matrix is found by taking the s-derivative of Eq. (3.4) and using Eq. (3.10), which produces the envelope equation[46]:

$$\frac{\mathrm{d}\boldsymbol{\sigma}}{\mathrm{d}s} = \mathbf{F}(s)\boldsymbol{\sigma} + \boldsymbol{\sigma}\mathbf{F}(s)^T. \tag{3.16}$$

`TRANSOPTR` numerically integrates Eq. (3.16) provided given initial boundary conditions on $\boldsymbol{\sigma}$. The transfer matrix $\mathbf{M}$ of an infinitesimal length ds is also computed and it relates to the $\mathbf{F}$ matrix as:

$$\mathbf{M}_{\mathrm{d}s} = \mathbf{I} - \mathbf{F}\mathrm{d}s. \tag{3.17}$$

Where $\mathbf{I}$ is the identity. The matrix $\mathbf{M}$, obtained by solving the equations of motion, acts upon the initial $\boldsymbol{\sigma}$-matrix of the beam, representing a point-to-point transformation:

$$\boldsymbol{\sigma_f} = \mathbf{M}\boldsymbol{\sigma_i}\mathbf{M}^T. \tag{3.18}$$

The contact transformation (3.18) is area preserving and can be inverted since the matrix $\mathbf{M}$ is symplectic:

$$\boldsymbol{\sigma_i} = \mathbf{M}^{-1}\boldsymbol{\sigma_f}(\mathbf{M}^{-1})^T. \tag{3.19}$$

The transfer matrix $\mathbf{M}$ evolves as:

$$\frac{\mathrm{d}\mathbf{M}}{\mathrm{d}s} = \mathbf{F}(s)\mathbf{M}. \tag{3.20}$$

Coordinates 5 and 6 in `TRANSOPTR` are defined as $(z, P_z) = (-\beta c\Delta t,\, \Delta E/(\beta c))$. Both are evaluated relative to the reference particle time and energy. The scaling factor βc converts coordinate 5 to the rms bunch length relative to the reference particle. Likewise, coordinate 6 is the rms longitudinal momentum spread[44]. But it must be made clear that from the Hamiltonian standpoint, the canonical pair is time and energy, not longitudinal distance and momentum. Acceleration is dealt with by scaling the initial momenta (P_x, P_y, P_z) by the initial total momentum P_0, followed by integration through the accelerating fields. Once this is complete, the output momenta are re-converted to angles by a scaling factor P_0/P_f, in other words the ratio of initial to final momentum[44, 47].

3.2 Liouville's Theorem and Emittance

If the forces $\vec{\mathbf{F}}$ which act upon the 6 dimensional beam density distribution function $f(x, P_x, y, P_y, z, P_z)$ are such that the work done around a closed path through configuration space is zero:

$$\oint \vec{\mathbf{F}} \cdot \mathrm{d}\vec{l} = 0, \tag{3.21}$$

the system is said to be conservative along with $\vec{\mathbf{F}}$[42]. Under the influence of such a force, the total time derivative of the density function is:

$$\frac{\mathrm{d}f}{\mathrm{d}t} = \{f, H\} + \frac{\partial f}{\partial t}, \tag{3.22}$$

where H is the Hamiltonian and the operator $\{,\}$ denotes the Poisson bracket:

$$\{f, H\} = \sum_{i=1}^{3} \left(\frac{\partial f}{\partial q_i}\frac{\partial H}{\partial p_i} - \frac{\partial f}{\partial p_i}\frac{\partial H}{\partial q_i} \right). \tag{3.23}$$

Here, the notation (q_i, p_i) for the canonically conjugate position momentum pairs has been used, with the index i summing over the three spatial coordinates (x, y, z). The presence of the Poisson bracket in Eq. (3.23) arises due to the implicit time dependence of the canonical coordinates: (q_i, p_i) themselves change over time, moving through the system's phase space, while the density distribution f may also explicitly change over time. However, if the forces are conservative, Eq. (3.21) applies to all particles composing f and no particles can escape the system, meaning the total population N is unchanged. In addition, the motion of particles inside such fields can be decomposed into a series of point-to-point transfer matrices according to Eq. (3.17), also known as contact transformations, which are volume preserving. Thus, together with the fact that N is constant, it follows that[42]:

$$\frac{\mathrm{d}f}{\mathrm{d}t} = 0. \tag{3.24}$$

Then, Eq. (3.22) reduces to:

$$\frac{\partial f}{\partial t} = -\{f, H\}. \tag{3.25}$$

The statement (3.25) is Liouville's theorem: A function $f(x, P_x, y, P_y, z, P_z)$, where each coordinate has time-dependency, is incompressible when its Poisson bracket with the Hamiltonian is zero, i.e. if it is a constant of the motion. Under those circumstances the emittance is a conserved quantity, since it is by definition the hypervolume of the distribution f:

$$\epsilon_6 = \int \cdots \int_{V_6} f(x, P_x, y, P_y, z, P_z)\mathrm{d}x \cdots \mathrm{d}P_z. \tag{3.26}$$

If the Poisson bracket $\{f, H\} = 0$, f is unchanging with the Hamiltonian and the integral (3.26) does not change either. For time-dependent potentials which do change the Hamiltonian, then a change in emittance can be expected, as is the case in accelerating rf cavities. This can also be appreciated by looking at the transverse beam divergence, which was normalized to the total momentum with the paraxial approximation:

$$x' = \frac{P_x}{P_0} = \frac{P_x}{\beta\gamma mc}. \tag{3.27}$$

Thus the divergence has $(\beta\gamma)^{-1}$ dependency Additionally, m represents the reference particle's rest mass. This causes x' to change along with the beam velocity. This effect can be accounted for by defining the normalized emittance ϵ^* of the beam, which is conserved under acceleration:

$$\epsilon^* = \beta\gamma\epsilon. \tag{3.28}$$

The inclusion of the relativistic parameter compensates the paraxial approximation discussed in Sec. 2.2, as P_0 changes. In the laboratory frame, an accelerating beam appears to shrink in transverse extent, though really this is a velocity dependent effect, not an underlying change to the distribution f in the Frenet-Serret frame.

3.3 Drift and Quadrupole Infinitesimal Transfer Matrices

Mirroring Section 2.4, the F-matrix for a field free drift space can be obtained by first setting the curvature $\rho = \infty$ in the Hamiltonian (3.1), while also setting all components of the scalar and vector potentials to zero:

$$H_s = -\sqrt{\left(\frac{E}{c}\right)^2 - m^2c^2 - P_x^2 - P_y^2}. \tag{3.29}$$

To minimize clutter, the parameter m is the rest mass of the reference particle everywhere in this work. By noting that in this case the reference particle momentum is:

$$P_0 = \sqrt{\left(\frac{E}{c}\right)^2 - m^2c^2}, \tag{3.30}$$

one can re-express the Hamiltonian (3.29) in terms of P_0, which greatly exceeds both P_x and P_y in magnitude, expanding to second order in the coordinates:

$$H_s = -P_0\sqrt{1 - \frac{P_x^2 + P_y^2}{P_0^2}} \approx -P_0 + \frac{P_x^2 + P_y^2}{2P_0}. \tag{3.31}$$

The above describes a beam drifting through space. In order to obtain the F-matrix, the second mixed partial derivatives of H_s are evaluated per Eq. (3.11):

Drift

$$\mathbf{F}(s) = \begin{pmatrix} 0 & \frac{1}{P_0} & 0 & 0 & 0 & 0 \\ 0 & 0 & 0 & 0 & 0 & 0 \\ 0 & 0 & 0 & \frac{1}{P_0} & 0 & 0 \\ 0 & 0 & 0 & 0 & 0 & 0 \\ 0 & 0 & 0 & 0 & 0 & \frac{1}{\gamma^2 P_0} \\ 0 & 0 & 0 & 0 & 0 & 0 \end{pmatrix}. \tag{3.32}$$

In this case, the F-matrix for a drift is trivial owing to the simplicity of the Hamiltonian. Considering a quadrupole, recalling the potential from Eq. (2.30):

$$\phi_Q = \frac{k}{2}(x^2 - y^2),$$

the Hamiltonian with this potential is, in the case of an electrostatic quadrupole where the vector potential components are zero:

$$H_s = -\sqrt{\left(\frac{E - q\phi_Q}{c}\right)^2 - m^2c^2 - P_x^2 - P_y^2}. \tag{3.33}$$

The term ϕ_Q possesses second order coordinate dependency. Expanding the term in parenthesis in (3.33), we obtain:

$$\left(\frac{E - q\phi_Q}{c}\right)^2 = \frac{E^2}{c^2} - \frac{2Eq\phi_Q}{c^2} + \mathcal{O}(x^4, y^4). \tag{3.34}$$

The linear, near-axis forces are desired, meaning up to second order in the Hamiltonian is needed. The fourth order terms in Eq. (3.34) are truncated and H_s becomes:

$$H_s \approx -\sqrt{P_0^2 - \frac{2Eq\phi_Q}{c^2} - P_x^2 - P_y^2}. \tag{3.35}$$

The reference particle momentum is given by Eq. (3.30) and is factored from the square root, producing:

$$H_s \approx -P_0\sqrt{1 - \frac{2Eq\phi_Q}{c^2 P_0^2} - \frac{P_x^2 + P_y^2}{P_0^2}} = -P_0\sqrt{1-\epsilon}, \tag{3.36}$$

where the expansion parameter ϵ contains the last two terms in the square root of Eq. (3.36) and is a small quantity. Expanding to second order:

$$H_s \approx -P_0 + \frac{Eqk}{2c^2 P_0}(x^2 - y^2) + \frac{P_x^2 + P_y^2}{2P_0}. \tag{3.37}$$

This expression is the quadraticized Hamiltonian for a quadrupole field and has the form of Eq. (3.9). This will make evaluating second partial derivatives of the canonical coordinates, needed for the F-matrix, trivial when compared to the full Hamiltonian which introduces square root dependency. The quadrupole field F-matrix is:

Quadrupole (Electrostatic or Magnetic)

$$\mathbf{F}(s) = \begin{pmatrix} 0 & \frac{1}{P_0} & 0 & 0 & 0 & 0 \\ -\frac{Eqk}{c^2 P_0} & 0 & 0 & 0 & 0 & 0 \\ 0 & 0 & 0 & \frac{1}{P_0} & 0 & 0 \\ 0 & 0 & \frac{Eqk}{c^2 P_0} & 0 & 0 & 0 \\ 0 & 0 & 0 & 0 & 0 & \frac{1}{\gamma^2 P_0} \\ 0 & 0 & 0 & 0 & 0 & 0 \end{pmatrix}. \tag{3.38}$$

Both (3.37) and (3.38) apply for either magnetic or electrostatic quadrupoles, depending on the definition of the strength parameter k, from Eqs. (2.32) and (2.33).

3.4 Beam Eccentricity

If the inter-quadrupole drift distances exceed a certain distance, Liouville's theorem together with the conservation of momentum dictate that the phase space distribution will shear in position-momentum space, becoming more highly eccentric, shown in Figure 3.1. This in turn will produce tunes more highly sensitive upon precise quadrupole settings, as will be discussed in the next chapter. The correlation coefficient between canonical coordinate pairs, or rather their beam matrix elements, can be expressed as:

$$\boxed{r_{12} = \frac{\boldsymbol{\sigma}_{12}}{\sqrt{\boldsymbol{\sigma}_{11}\boldsymbol{\sigma}_{22}}}} \tag{3.39}$$

By definition, r_{12} is bound in [-1,1]. The correlation coefficient provides a measure of the evolution of the (x, P_x) eccentricity of the beam distribution along the reference

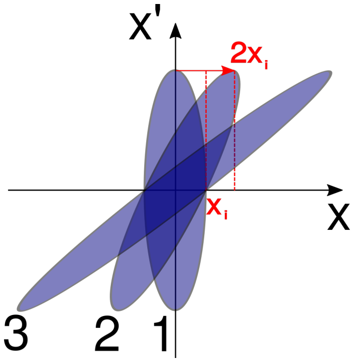

Figure 3.1: A hypothetical phase space ellipse (**1**) initially with α=0 and a half-width x_i, drifts a distance d causing it to double in size (**2**). A particle initially at the peak of the ellipse (0,$\sqrt{\gamma_x \epsilon_x}$), will travel a transverse distance $2x_i$ along the x-axis as the beam doubles in size. If the drift distance is larger, more shearing will result, broadening the extent of the distribution in phase space (**3**). The eccentricity is a proxy for this process, represented by the (x, P_x) correlation coefficient.

orbit. Consider the evolution of $\boldsymbol{\sigma}_{11}$ along s:

$$\boldsymbol{\sigma}_{11} = \langle x^2 \rangle = \int x^2 f(x, P_x, \ldots, P_z) \mathrm{d}x \mathrm{d}P_x \ldots \mathrm{d}P_z \tag{3.40}$$

$$\frac{\mathrm{d}\boldsymbol{\sigma}_{11}}{\mathrm{d}s} = 2 \int x x' f(x, P_x, \ldots, P_z) \mathrm{d}x \mathrm{d}P_x \ldots \mathrm{d}P_z. \tag{3.41}$$

The envelope in a drift is, per Eqs. (3.16) and (3.32):

$$\frac{\mathrm{d}\boldsymbol{\sigma}}{\mathrm{d}s} = \frac{1}{P_0} \begin{pmatrix} 2\boldsymbol{\sigma}_{12} & \boldsymbol{\sigma}_{22} \\ \boldsymbol{\sigma}_{22} & 0 \end{pmatrix}. \tag{3.42}$$

Here, we assume that the (x, P_x) distribution starts at a waist, with the initial value for $\boldsymbol{\sigma}_{12}$ being 0. Additionally, $\boldsymbol{\sigma}_{22}$ remains unchanging during a drift in free space. Integrating the terms of Eq. (3.42) over s, the correlation coefficient from Eq. (3.39) can be re-expressed over a drift as:

$$r_{12}(s) = \frac{s}{\sqrt{s^2 + C}}, \tag{3.43}$$

$$C = \frac{P_0^2 \boldsymbol{\sigma}_{11\mathrm{i}}}{\boldsymbol{\sigma}_{22}}, \tag{3.44}$$

where $\boldsymbol{\sigma}_{11\mathrm{i}} = \langle x^2 \rangle|_{s=0}$. The second term in the denominator of (3.43) is a constant, depending on the value of $\boldsymbol{\sigma}_{11\mathrm{i}}$. As s grows, $r_{12}(s)$ asymptotically approaches unity. From the waist, beam doubles in transverse size over a distance:

$$s_{2x} = P_0 \sqrt{\frac{\boldsymbol{\sigma}_{11\mathrm{i}}}{\boldsymbol{\sigma}_{22}}} \tag{3.45}$$

and the correlation coefficient at that position has a value:

$$r_{12}(s_{2x}) = \sqrt{\frac{3}{4}} \approx 0.866. \tag{3.46}$$

Before this point, the envelope's shape can be qualitatively described as curved, while downstream the shape increasingly resembles a straight line, corresponding to a single particle trajectory with momentum $P_x = \sqrt{\boldsymbol{\sigma}_{22}}$, shown in Figure 3.2.

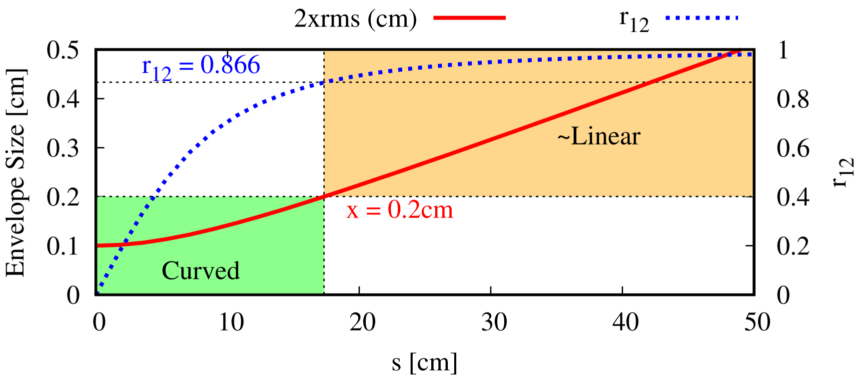

Figure 3.2: An $A/q=6$ beam starting from a round waist with a size of 0.1 cm and divergence of 10 mrad at $E/A=0.153$ MeV/u doubles in size over a distance $s=17.3$ cm per Eq. (3.45).

3.5 Dipole Magnets and Spherical Benders

Transit through a dispersive element with edge angles, shown in Figure 3.3 is broken into three segments in `TRANSOPTR`: initial edge interaction, transit and exit edge interaction. The one-way edge field interaction at an angle α with a dipole possessing a reference radius of curvature ρ is described by the F-matrix[40]:

Bending Edge Angle Field Interaction

$$\mathbf{F}(s) = \begin{pmatrix} 1 & 0 & 0 & 0 & 0 & 0 \\ \frac{\tan\alpha}{\rho} & 1 & 0 & 0 & 0 & 0 \\ 0 & 0 & 1 & 0 & 0 & 0 \\ 0 & 0 & -\frac{\tan(\alpha-\psi)}{\rho} & 1 & 0 & 0 \\ 0 & 0 & 0 & 0 & 0 & 0 \\ 0 & 0 & 0 & 0 & 0 & 0 \end{pmatrix}. \tag{3.47}$$

This matrix is not obtained from a Hamiltonian, but rather from an impulse approximation, over a single step. The edge angle interaction produces a transverse focal effect. Regarding the function ψ, Brown notes[48] ” *The quantity ψ is the correction to the transverse focal length when the finite extent of the fringing field is included.*”

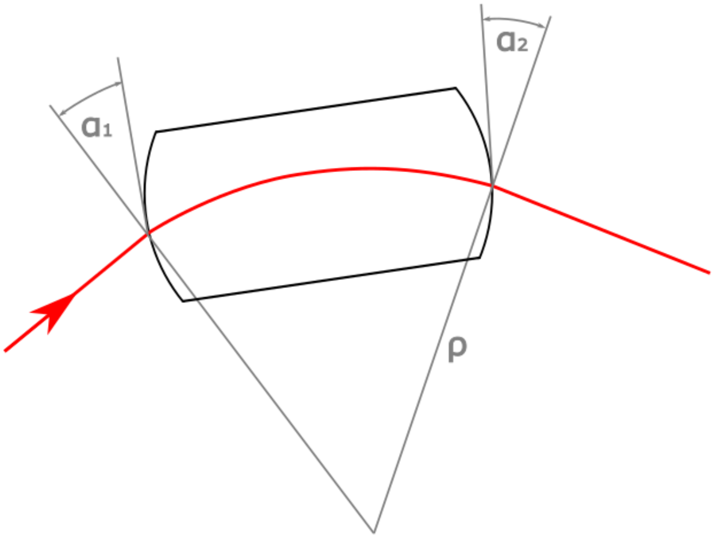

Figure 3.3: Illustration of a reference trajectory (red), through a uniform dipole field (contained within black lines) featuring edge angles α_1 and α_2 normal to the reference particle trajectory (red). The reference orbit radius of curvature is ρ. `TRANSOPTR` handles this sequence in three parts: edge angle interaction, dipole drift & exit edge angle interaction.

The parameter ψ is defined as:

$$\psi = Khg \sec\alpha(1 + \sin^2\alpha), \tag{3.48}$$

with $h = 1/\rho$, the inverse reference radius of curvature and g being the distance between magnet poles defining the gap. The parameter K is defined as:

$$K = \int_{-\infty}^{\infty} \frac{B_y(z)[B_0 - B_y(z)]}{gB_0^2} \mathrm{d}z \tag{3.49}$$

which itself must be calculated from the field. The parameter $B_y(z)$ in the integral is defined by Brown as[48] "*the magnitude of the fringing field on the magnetic mid* *plane at a position z. z is the perpendicular distance measured from the entrance face of the magnet to the point in question.* B_0 *is the asymptotic value of* $B_y(z)$ *well inside the magnet entrance. Typical values of K for actual magnets may range from 0.3 to 1.0 depending upon the detailed shape of the magnet profile and the location of the energizing coils.*" In particular, the edge angle field interaction F-matrix is similar to that of a quadrupole, producing a transverse focal effect.

Dispersive transit through the bending field is now considered, first looking at the case of an electrostatic bender with spherical electrodes. The bend radius is A in the bending plane and A_y in the non bending plane[49], which in the spherical case are equal. The reference orbit curvature is $h=1/A=1/A_y$. The scalar potential for the bender is:

$$\phi_B = 1 - 1/\sqrt{1+2hx+h^2x^2+h^2y^2}, \tag{3.50}$$

$$\phi_B = hx - h^2x^2 + \frac{h^2y^2}{2} + h^3x^3 - \frac{3h^3xy^2}{2} + \cdots \tag{3.51}$$

Where the potential has been expanded in (3.51). The latter can be placed in the Hamiltonian (3.1), which must be converted to curvilinear coordinates, shown in[49]. For the general case where $A \neq A_y$, the quadraticized electrostatic bender Hamiltonian, to second order is:

$$H_{\mathrm{BE}} = \frac{P_x^2}{2} + \frac{P_y^2}{2} + \frac{P_\tau^2}{2\gamma^2} - \frac{2-\beta^2}{A}xP_\tau + \frac{\xi^2}{2A^2}x^2 + \frac{\eta^2}{2A^2}y^2. \tag{3.52}$$

The Hamiltonian (3.52) uses the longitudinal canonical coordinate pair $\tau = s - \beta ct$ and $P_\tau = \Delta E/(\beta c)$. Further, the parameters ξ and η are defined:

$$\xi^2 + \eta^2 = 2 - \beta^2, \tag{3.53}$$

$$\eta^2 = A/A_y. \tag{3.54}$$

The resulting F-matrix is:

Spherical Electrostatic Bender

$$\mathbf{F}(s) = \begin{pmatrix} 0 & \frac{1}{P_0} & 0 & 0 & 0 & 0 \\ -\frac{\xi^2}{A^2 P_0} & 0 & 0 & 0 & 0 & \frac{2-\beta}{AP_0} \\ 0 & 0 & 0 & \frac{1}{P_0} & 0 & 0 \\ 0 & 0 & \frac{\eta^2}{A^2 P_0} & 0 & 0 & 0 \\ -\frac{2-\beta}{AP_0} & 0 & 0 & 0 & 0 & \frac{1}{\gamma^2 P_0} \\ 0 & 0 & 0 & 0 & 0 & 0 \end{pmatrix}. \tag{3.55}$$

For low energy cases with spherical electrodes of equal radii in both planes, $\eta = 1$. The matrix (3.55) possesses nonzero terms which will introduce correlations between (x, P_x) in the dispersive plane and (z, P_z). Envelope equation solutions after this element will inherit these correlations unless corrected for with downstream elements. The case of a dipole bending magnet with mid-plane symmetry is treated in[50]. Unlike the electrostatic bender, for a magnetic dipole coordinate 5 is defined according to the standard $(z, P_z) = (-\beta c \Delta t, \Delta E/(\beta c))$. After expansion to second order, the Hamiltonian:

$$H_s = \frac{P_x^2}{2P_0} + \frac{P_y^2}{2P_0} + \frac{P_z^2}{2\gamma^2 P_0} + \frac{1-n}{2\rho^2 P_0} x^2 + \frac{n}{2\rho^2 P_0} y^2 - \frac{x P_z}{\rho P_0} \tag{3.56}$$

is obtained. The parameter ρ is the reference radius of curvature through the field B_0 felt by the reference particle, while n is the field index:

$$n = \frac{\rho}{B_0} \frac{\partial B}{\partial x}\bigg|_{x=0}, \tag{3.57}$$

which is trajectory dependent and is computed for the reference particle. After evaluation of the second order partial derivatives of the Hamiltonian, the F-matrix is obtained:

Magnetic Dipole Bender

$$\mathbf{F}(s) = \begin{pmatrix} 0 & \frac{1}{P_0} & 0 & 0 & 0 & 0 \\ -\frac{1-n}{\rho^2 P_0} & 0 & 0 & 0 & 0 & \frac{1}{\rho P_0} \\ 0 & 0 & 0 & \frac{1}{P_0} & 0 & 0 \\ 0 & 0 & -\frac{n}{\rho^2 P_0} & 0 & 0 & 0 \\ -\frac{1}{\rho P_0} & 0 & 0 & 0 & 0 & \frac{1}{\gamma^2 P_0} \\ 0 & 0 & 0 & 0 & 0 & 0 \end{pmatrix}. \tag{3.58}$$

Note the similarities between the above F-matrix and that of the electrostatic spherical bender (3.55). Just as the latter, the magnetic dipole with mid-plane symmetry introduces dispersion and produces chromatic couplings which must be corrected. It is noted that for magnetic dipoles, it is necessary to measure the field to extract the requisite parameters for the F-matrix. Alternatively, these can also be obtained through field simulations.

3.6 Axially Symmetric Accelerating Fields

For axially symmetric, time dependent electric fields, the F-matrix (3.11) can be obtained by using a vector and scalar potential A_s and Φ, shown by Baartman[44]:

$$A_s(x,y,s,t) = \mathcal{E}(s)\left(1 - \frac{\omega^2}{c^2}\frac{x^2+y^2}{4}\right)\frac{\sin(\omega t + \theta)}{\omega} \tag{3.59}$$

and

$$\Phi(x,y,s,t) = \frac{d\mathcal{E}(s)}{ds}\cos(\omega t + \theta)\frac{x^2+y^2}{4}. \tag{3.60}$$

The function $\mathcal{E}(s)$ is the intensity of the longitudinal component of the electric field, measured on-axis. The angular frequency is related to the rf frequency by $\omega = 2\pi f$

and the parameter θ here denotes an rf phase offset. This parametrization is particularly useful since values for $\mathcal{E}(s)$ can either be obtained by rf cavity measurements or computed with a field simulation code. The second order linearized Hamiltonian is:

$$H_s = \frac{P_x^2}{2P_0} + \frac{P_y^2}{2P_0} + \frac{P_z^2}{2\gamma^2 P_0} + \frac{q}{2\beta c}\left(\mathcal{E}'C - \mathcal{E}S\frac{\omega\beta}{c}\right)\frac{r^2}{2} + \frac{2q\mathcal{E}C}{\beta c}\frac{zP_z}{2\gamma^2 P_0} - \frac{q\mathcal{E}\omega S}{\beta^2 c^2}\frac{z^2}{2}, \tag{3.61}$$

where $S = \sin(\omega t_0 + \theta)$ and $C = \cos(\omega t_0 + \theta)$. The symmetries of the axial field mean all the dynamics, including the effects of transverse rf focusing, are produced to first order with the above Hamiltonian. Moreover, it provides the means to simulate rf linear acceleration without resorting to TTF approximations. Instead, both the field amplitude and phase are required as input parameters, exactly the same tuning parameters available to operators in the control room. `TRANSOPTR` simply integrates the equations of motion using those as initial conditions. The Hamiltonian (3.61) produces the F-matrix:

Axially Symmetric Linac Field

$$\mathbf{F}(s) = \begin{pmatrix} 0 & \frac{1}{P_0} & 0 & 0 & 0 & 0 \\ \mathcal{A}(s) & 0 & 0 & 0 & 0 & 0 \\ 0 & 0 & 0 & \frac{1}{P_0} & 0 & 0 \\ 0 & 0 & \mathcal{A}(s) & 0 & 0 & 0 \\ 0 & 0 & 0 & 0 & \frac{\beta'}{\beta} & \frac{1}{\gamma^2 P_0} \\ 0 & 0 & 0 & 0 & \mathcal{B}(s) & -\frac{\beta'}{\beta} \end{pmatrix} \tag{3.62}$$

Given its vanishing contribution to the beam dynamics, the vector potential component which represents the magnetic field has been neglected. Further, for the linear component of the transverse beam envelope as used in `TRANSOPTR`, only the derivative of the electric field $\mathcal{E}'$(s) is needed off axis, in the form of the function $\mathcal{A}$(s), while the field's amplitude is required for the longitudinal computation, via the term $\mathcal{B}$(s):

$$\mathcal{A}(s) = -\frac{q}{2\beta c}\left(\mathcal{E}'(s)C - \mathcal{E}(s)S\frac{\omega\beta}{c}\right), \tag{3.63}$$

$$\mathcal{B}(s) = \frac{q\mathcal{E}(s)\omega S}{\beta^2 c^2}. \tag{3.64}$$

Implementation of the ISAC-DTL in `TRANSOPTR` therefore requires knowledge of $\mathcal{E}(s)$. The energy of the reference particle is evaluated at each step:

$$E(s) = E_0 + qV_s \int \tilde{\mathcal{E}}(s)\cos(\omega t(s) + \phi)\mathrm{d}s, \tag{3.65}$$

where V_s is a scaling factor for the normalized on-axis electric field profile $\tilde{\mathcal{E}}(s)$, bound in [-1,1]. It is noteworthy that V_s and ϕ are the parameters which operators control when tuning the machine.

3.7 2-Term RFQ Linear Accelerator

`TRANSOPTR` lacked the ability to simulate a time-dependent modulated quadrupole field, arising from electrodes as shown in Figure 3.4. Implementation first required obtaining the infinitesimal transfer matrix describing its dynamics. The first two terms of the Kapchinsky and Teplyakov infinite series potential for a modulated quadrupole[51] are[27, 52]:

$$\phi_{\text{2RFQ}} = \frac{V_0}{2}\left(A_{01}(x^2 - y^2) + A_{10}I_0(k\sqrt{x^2+y^2})\cos(\psi(s))\right)\sin(\omega t + \theta). \tag{3.66}$$

which defines the transverse focusing and longitudinally accelerating electric fields. The vane voltage is V_0, RFQ design wavenumber k, aperture a and modulation factor[1] m. Additionally:

$$A_{01} = \frac{1}{a^2}\frac{I_0(ka) + I_0(mka)}{m^2 I_0(ka) + I_0(mka)}, \tag{3.67}$$

$$A_{10} = \frac{m^2 - 1}{m^2 I_0(ka) + I_0(mka)}. \tag{3.68}$$

---

[1] not to be confused with the reference particle rest mass

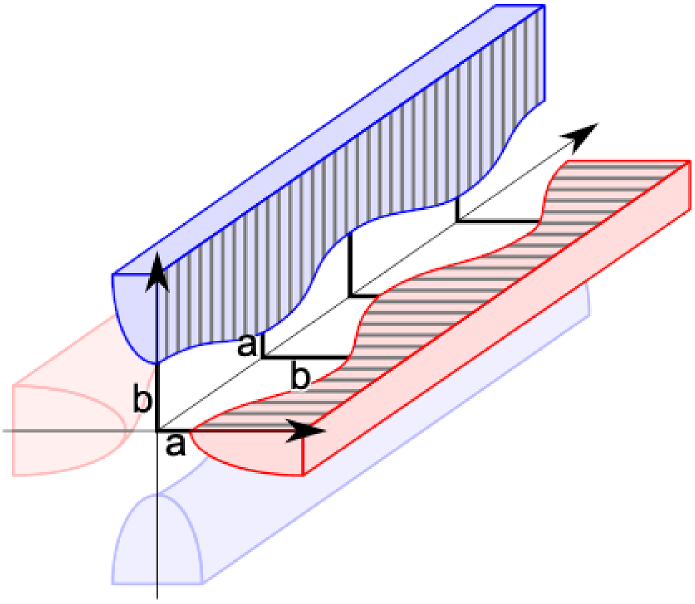

Figure 3.4: Cutaway view of the 4-vanes of an RFQ accelerator[53], showing the transverse and longitudinal modulations. A time-varying voltage induced on the vanes produces an electric field which alternatingly accelerates beam longitudinally, then focuses it transversely. Charged particles of correct injection properties and phase (timing) will both gain energy and remain proximal to each other during acceleration. By convention, half of a longitudinal modulation corresponds to one RFQ cell.

The quadrupole component of the potential (3.66) is represented by the term involving A_{01}, the transverse focusing efficiency, while the energy gain component is A_{10}, the longitudinal accelerating efficiency. RFQ codes like `PARMTEQ` perform a cell-by-cell integration, where the longitudinal coordinate is defined on a [0,2π] interval. In the `TRANSOPTR` case, since a continuous integration in being performed through the accelerator, the function $\psi(s)$, the spatial phase of the potential, is introduced and defined as:

$$\psi(s) = \int_0^s k(\xi)d\xi = \int_0^s \frac{ds}{\beta(s)}, \tag{3.69}$$

with:

$$k(s) = \frac{2\pi}{\beta(s)\lambda}. \tag{3.70}$$

The function $k(s)$ is the continuous longitudinal vane modulation wavenumber. Simply coding the product of the variables ks in TRANSOPTR will fail, since it will render accelerating synchronism impossible. Instead, the function $\psi(s)$ from Eq. (3.69) substitutes the product ks and the cosine term from Eq. (3.66) becomes $\cos\psi(s)$. The two-term potential expansion produces an RFQ field which correctly describes near-axis dynamics, for $r \ll a$. The potential (3.66) is inserted in the Courant-Snyder Hamiltonian (3.1) with $\rho = \infty$ and all vector potential components set to zero:

$$H_s(t,-E) = -\sqrt{\left(\frac{E - q\phi_{2\mathrm{RFQ}}}{c}\right)^2 - m^2c^2 - P_x^2 - P_y^2}. \tag{3.71}$$

From Eq. (3.71) a linearized Hamiltonian, with up to second order coordinate dependence is extracted[14]:

$$H_s(z,P_z) = \left(\frac{E_0}{\beta c} - P_0\right) + \frac{P_x^2}{2P_0} + \frac{P_y^2}{2P_0} + \frac{P_z^2}{2\gamma^2 P_0} + \frac{\mathcal{A}_+}{2}x^2 + \frac{\mathcal{A}_-}{2}y^2 + \mathcal{B}(s)zP_z + \frac{\mathcal{C}}{2}z^2. \tag{3.72}$$

The F-matrix for a two-term RFQ field is:

Radiofrequency Quadrupole (2-term potential)

$$\mathbf{F}(s) = \begin{pmatrix} 0 & \frac{1}{P_0} & 0 & 0 & 0 & 0 \\ -\mathcal{A}_+ & 0 & 0 & 0 & 0 & 0 \\ 0 & 0 & 0 & \frac{1}{P_0} & 0 & 0 \\ 0 & 0 & -\mathcal{A}_- & 0 & 0 & 0 \\ 0 & 0 & 0 & 0 & \mathcal{B} & \frac{1}{\gamma^2 P_0} \\ 0 & 0 & 0 & 0 & -\mathcal{C} & -\mathcal{B} \end{pmatrix}, \tag{3.73}$$

with the functions:

$$\mathcal{A}_{\pm} = \frac{qV_0 \sin(\omega t_0 + \phi)\,(k^2 A_{10} \cos\psi \pm 4A_{01})}{4\beta c} \tag{3.74}$$

$$\mathcal{B} = \frac{qV_0 A_{10}\,(k \sin\psi \sin(\omega t_0 + \phi) + (\omega/(\beta c)) \cos\psi \cos(\omega t_0 + \phi))}{2\beta^2\gamma^3 mc^2} \tag{3.75}$$

$$\mathcal{C} = \frac{qV_0(\omega/(\beta c))^2 A_{10} \cos\psi\,(qV_0 A_{10}/(\beta^2\gamma^3 mc^2) \cos\psi \cos^2(\omega t_0 + \phi) - 2\sin(\omega t_0 + \phi))}{4\beta c}. \tag{3.76}$$

The RFQ F-matrix superficially resembles that of a quadrupole from (3.38) in the (x, P_x, y, P_y) components, which is sensible as the accelerator consists of modulated quadrupole electrodes. In particular, the transverse focusing term A_{01} from the 2-term potential (3.67) is present only in the terms $\mathcal{A}_{\pm}$, while the longitudinal acceleration efficiency A_{10} of Eq. (3.68) is found in each of $\mathcal{A}$, $\mathcal{B}$ and $\mathcal{C}$, with the last two affecting coordinates 5 and 6. The reference particle energy is computed from the longitudinal component of the electric field:

$$E(s) = E_0 + \frac{qA_{10}kV_0}{2} \sin\psi \sin(\omega t_0 + \phi). \tag{3.77}$$

With this addition[14], `TRANSOPTR` possesses all of the necessary theoretical components to implement a full simulation of the ISAC linear accelerator.

3.8 `TRANSOPTR` Sequence Structure and Capabilities

One of the great strengths of computing the evolution of the $\boldsymbol{\sigma}$-matrix is the relative computational efficiency of only tracking moments of the distribution, as opposed to a statistically significant sample of individuals. `TRANSOPTR` is a beam transport and design code[39], meaning it allows for the simultaneous optimization of both the transport system parameters in addition to constraints upon the $\boldsymbol{\sigma}$-matrix. It is written in `FORTRAN`. A main, user-defined system file contains the transport and acceleration lattice that the code uses for its computations, with each element represented as a subroutine. An example system file (`sy.f`) is shown in Figure 3.5, representing an

RFQ accelerator, surrounded by drift spaces. In the figure, constraints upon the final sigma matrix are specified at the RFQ exit:

- $\mathbf{M}_{55} \longrightarrow 0$,
- $\boldsymbol{\sigma}_{66} \longrightarrow 0$,
- $E_f/A = 0.153\,\mathrm{MeV/u}$,
- RFQ output Twiss parameter match $(-\alpha_i, \beta_i)$ for both (x, y) requested.

If `TRANSOPTR` is called upon to perform a parameter optimization, then an internal optimizer will attempt to establish the user defined constraints. Both the list of parameters to be optimized and their initial values are stored in an initial condition file, which also contains information on the starting $\boldsymbol{\sigma}$-matrix[54]. Twiss parameter matching can also be performed, with `TRANSOPTR` using Bovet's mismatch parameter from Eq. (2.54)[13] as an optimization variable. `TRANSOPTR` currently possesses two main fit routines: downhill simplex, also known as amoeba and simulated annealing[55, 56, 57]. The downhill simplex method is efficient when the number of fit parameters does not exceed roughly four[13], after which successful obtention of a global minimum can become sensitive to the initial values. Simulated annealing is more efficient at searches for large parameter space optima, though it becomes more time consuming as the number of parameters grows. For these reasons, `TRANSOPTR` fits are typically carried out with a maximum of about 10 simultaneous parameters.

The integration step size h must typically be user-defined in many Runge-Kutta methods. This is problematic since there may be time-dependent fields represented in the envelope equation (3.16). In those cases, should the parameter h be required as input, its optimum value would be constrained by time-dependent elements in the system, though this would almost certainly result in an excessive overall number of steps. Conversely, if h is too big, simulation of energy gain would break down due to undersampling of Eq. (3.15). `TRANSOPTR` avoids this conundrum by making use of the Runge-Kutta-Merson method. The algorithm takes 5 samples for a step size

```
      SUBROUTINE TSYSTEM
      COMMON /BLOC1/vane,rfp
      COMMON/SCPARM/QSC,ISC,CMPS
      COMMON/MOM/P,BRHO,pMASS,energk,gsq,ENERGKi,charge,current
      COMMON/PRINT/IPRINT,IQ(8)

      iq(1)=6

      CMPS=0.6
      nscav=100
      endDrift=15.825!cm
      rmsDrift = 8.8814!cm: start of RMS in original PARMTEQ after drift

      call dr(rmsDrift,".")
      call rfq(75,692,vane,760.1206,35.435E+06,rfp,nscav)
      call fit(2,5,5,0.,1.,1)
      call fit(1,6,6,0.,1.,1)
      call dr(endDrift,".")
      energerr=0.153*(PMASS/931.595) - energk
      call fitarb(0.0,energerr,1.,1)

       return
      end
```

Figure 3.5: `TRANSOPTR` system file `sy.f`, in which the elements of the transport or acceleration lattice are coded. `BLOC1`, a common variable block, reads the user specified device specific input parameters. This example shows a simulation including the RFQ subroutine, based on the F-matrix (3.73). The parameters `vane` and `rfp`, representing the vane voltage and rf phase, are supplied by the user prior to execution. These parameters can also be optimized as part of user defined constraint optimization problems in `TRANSOPTR`, for example finding the requisite phase and voltage to achieve a certain output energy. An `ascii` formatted file containing pairs of (s, a, m, k) along the structure is read-in by `TRANSOPTR` and spline interpolated to provide values for the RFQ parameters along the length of the structure. The quantity `PMASS` is the reference particle mass, in MeV/c^2, which in the code is converted into amu.

parameter h[58, 59]:

$$\begin{aligned} k_1 &= hf(x_0, y_0), \quad y_0 = y(x_0), \\ k_2 &= hf\big(x_0 + \tfrac{1}{3}h, y_0 + \tfrac{1}{3}k_1\big), \\ k_3 &= hf\big(x_0 + \tfrac{1}{3}h, y_0 + \tfrac{1}{6}k_1 + \tfrac{1}{6}k_2\big), \\ k_4 &= hf\big(x_0 + \tfrac{1}{2}h, y_0 + \tfrac{1}{8}k_1 + \tfrac{3}{8}k_3\big), \\ k_5 &= hf\big(x_0 + h, y_0 + \tfrac{1}{2}k_1 - \tfrac{3}{2}k_3 + 2k_4\big), \end{aligned} \tag{3.78}$$

along with the two error estimation functions:

$$\begin{aligned} y^1(x_0 + h) &= y_0 + \tfrac{1}{2}k_1 - \tfrac{3}{2}k_3 + 2k_4, \\ y^2(x_0 + h) &= y_0 + \tfrac{1}{6}k_1 + \tfrac{2}{3}k_4 + \tfrac{1}{6}k_5. \end{aligned} \tag{3.79}$$

Instead of requiring h as input, the user must select an error tolerance ϵ. The initial step size is an arbitrary value and an initial guess solution is evaluated. At each step, the quantity:

$$R = 0.2|y^1 - y^2| \tag{3.80}$$

is used as an error estimator for the solution and is compared to ϵ. If R exceeds the tolerance, h is halved, whereas if $R < \epsilon/64$, h is doubled. The step size is chosen when $\epsilon/64 < h < \epsilon$, at each step of the integration. Use in `TRANSOPTR` of this adaptive method[13] allows for a solution of consistent accuracy across elements whose sensitivity upon the step size will vary greatly. For instance, the RFQ simulation from Figure 3.5 was run in order to produce the envelope shown in Fig. 3.6 where a mismatch causes a synchro-betatron oscillation. The integrator has automatically determined the optimum value for each h, having been given a tolerance of $\epsilon = 10^{-4}$. The computation consisted of 28,260 integration steps, which are sufficiently small to capture the transverse effect of individual cell modulations upon the transverse envelopes. This can now be used to compute and optimize beam envelopes through RFQ accelerators, as part of larger transport systems. On a conventional desktop PC, this entire computation took 0.3 seconds. Addition of the RFQ linac to `TRANSOPTR` presents a novel fast envelope simulation capability, in turn enabling efficient parameter scan investigations of rf quadrupoles[60]. The computational efficiency of this approach means tunes can be computed in little time, making the `TRANSOPTR` implementation of an accelerator a powerful asset for machine tuning.

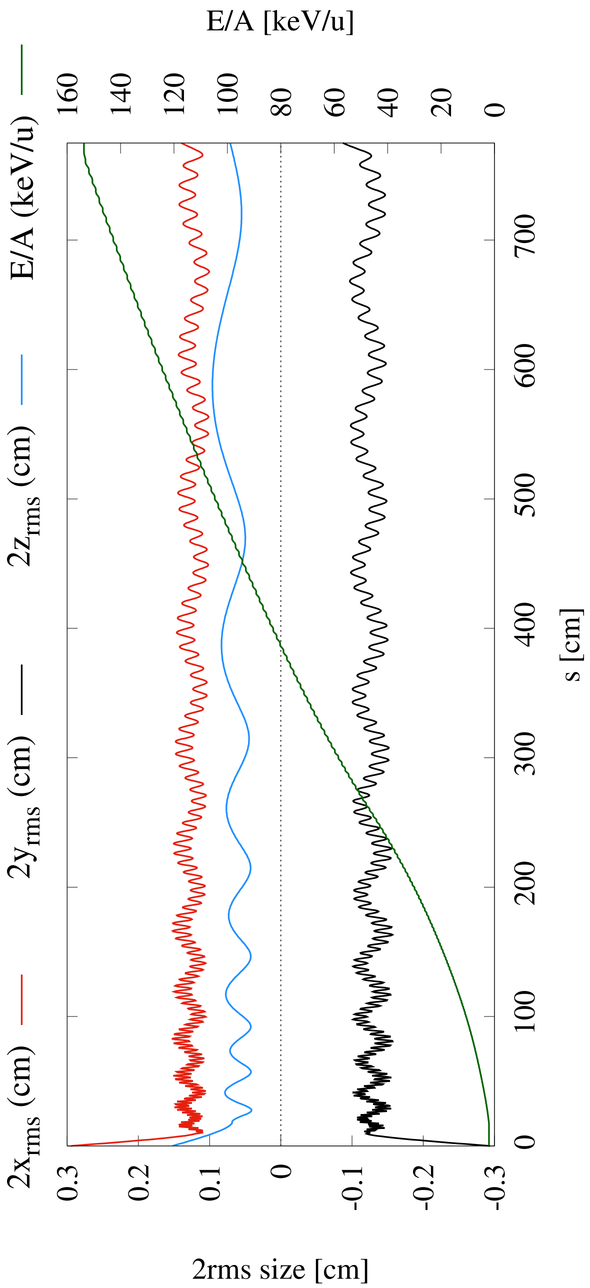

Figure 3.6: `TRANSOPTR` simulation of RFQ acceleration of an ^{14}N^{+} beam at input E/A of 2.04 keV/u ($E = 28.56$ keV) up to an output E/A of 153 keV/u ($E = 2.15$ MeV) in the ISAC-RFQ. The vertical envelope (y) is shown as negative while the horizontal (x) and longitudinal (z) envelopes are positive. The reference particle energy along the linac structure is shown on the top axis.

3.9 TRANSOPTR Use via python

Nascent infrastructure at TRIUMF, part of the high-level applications project, enables `python` based read/write interfacing with the EPICS control system[21]. The TRIUMF Beam Physics department has further developed a `python` wrapped capability to execute `TRANSOPTR`, allowing for the running of envelope simulations as a generic function call. User defined, automatic generation and computation of arbitrary sequences of the ISAC linac in `TRANSOPTR` is enabled thanks to a centralized `XML` repertoire of beam optical device positions along the machine, from which the `TRANSOPTR` files are created. This ensures all simulations are referenced to the same source for element positions and definitions. The `python` framework, dubbed `accpy`, renders straightforward the reading of beam diagnostic data and its use for on-line tune computations. It also enables the loading of `TRANSOPTR` computed tune values into the control system, providing a significant reduction in operational tuning complexity.

The original use case for `TRANSOPTR`, shown in Figure 3.7, assumes a user defines a single system file and keeps using it. The standard initial value file (`data.dat`) is altered as necessary by the user and the simulation is run. The outputs are then read and used elsewhere. If the returned set of optimum setpoints are to be re-incorporated back into the computation, they must be manually typed into `data.dat`. Computation of a full tune for the ISAC linac would involve a sequence file containing well above 100 elements (quadrupoles, bends, rf cavities, etc..), which would be impractical for both the user and the optimizer. Instead, to compute long tunes, it is advantageous to break the problem into smaller, shorter groups of devices. This both diminishes the burden on the Runge-Kutta engine and it also reduces the volume of the parameter space for the optimizer to work with, both speeding up the optimization and increasing its chances of converging. By calling `TRANSOPTR` through `python`, as shown in Figure 3.8, it is much simpler to generate, run and read-in the simulation results, which can then be re-used as part of a further optimization. This way, the sequence

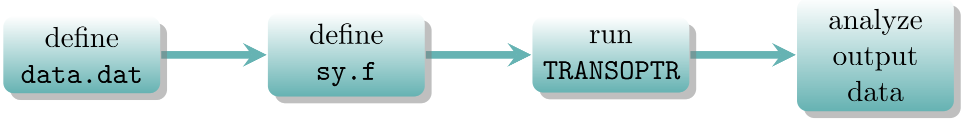

Figure 3.7: Classical use case of `TRANSOPTR`.

can be broken into smaller groups of devices which can easily be handled by optr's optimizer. It also permits the automation of this process. As an example of the power of this technique, `TRANSOPTR` can be used to optimize rf amplitude and phase parameters from the electric fields representing accelerating cavities in the DTL, producing for example maximized energy gain.

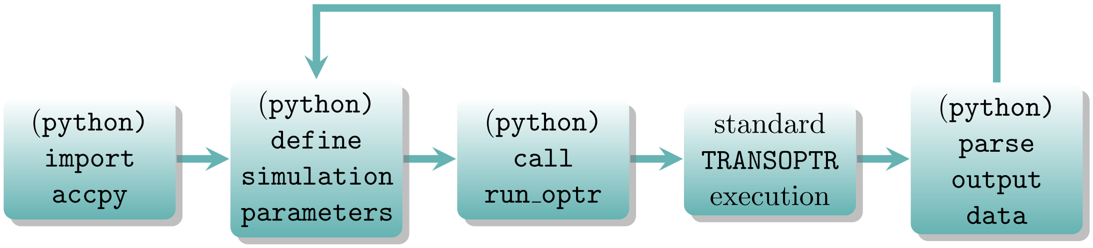

Figure 3.8: `python` wrapped use case for `TRANSOPTR`, called via function `get_optr`. Output data is parsed and returned to program, enabling sequential optimization.

Thus, it is possible to write accelerator tune optimization software in `python`, as well as to integrate this software within contemporary web application frameworks, enabling the development of browser based tuning interfaces.

3.10 Tuning Accelerators with `TRANSOPTR`

Machines such as RIB postaccelerators require constant changes in beam A/q and E/A, which means start-to-end machine re-tuning occurs frequently. At TRIUMF, the tuning methodology for the linac, to date, has been based on the use of *reference* tunes, which for the most part find their origin in multiparticle beam simulations dating to initial design investigations. Following commissioning, the tunes established during initial accelerator runs have been passed along to operators. The field gradients for the optics are translated into control system setpoints, either voltages or currents, and the tunes can be scaled for A/q as needed. Both short and long term changes of conditions require operators adjust these tunes manually over time. Examples of short term changes include the moving of quadrupole lenses along the beamline[61, 62] due to mechanical alterations necessary for maintenance, or changes in ion source extracted beam distribution from one source configuration to the next. Longer term changes include the ISAC experimental hall's foundation settling over time, found to require increasing amounts of corrective steering in the MEBT section[63], which has consequences for the alignment and transmission through the machine. The reliance upon design tunes more than two decades old leads to a status quo where many of the original simulation files are no longer available, or difficult to obtain. The variety of programs needed to simulate subsections of the accelerator also increases the complexity of studying full machine tunes. Over time, this allows the decoupling of accelerator tuning methodology from understanding of the physics at hand. In particular, this is true when tuning is performed with the sole constraint of maximizing beam transmission through each section, by both steering but also detuning quadrupoles. In such a tuning regime, mismatches in the accelerator are not regarded as deviations with respect to expected behaviour, rather they are treated as an expected occurrence; manual tuning palliates this. `TRANSOPTR`'s novel capabilities enable full ISAC-linac envelope simulations and tune optimizations. It is thus feasible to use the envelope code to perform live computations, using real-time machine setpoints and beam diagnostic readings as inputs to both compute the envelopes and perform constrained optimizations. In turn, these model computed optics settings are loaded back to the machine, closing a feedback loop and coupling the model and machine for operation (Figure 3.9). Tune computation in `TRANSOPTR` is accomplished by placing constraints in the system file, representing desired properties of the $\boldsymbol{\sigma}$-matrix at a particular location. As an example, one can request that the matrix element $\boldsymbol{\sigma}_{21} = 0$ by adding the following to `sy.f`:

```
    call fit(1,2,1,0.,1.,1)
```

The first parameter in the `fit` call specified a constraint upon the beam matrix; if 2 is entered, the constraint is upon the transfer matrix. The next two inputs in `fit` specify the matrix element, in this case $\boldsymbol{\sigma}_{21}$, with the fourth input parameter being its fit value, in this case zero. The second to last input is the weight of the fit constraint, while the final input parameter specifies the exponent of the square of the deviations. These constraints upon the envelope define the tune and are generally unchanging from one beam to the next. By coding these constraints directly into the `XML` repository, placing them at the exact location along the beamline where they are invoked, one can automatically generate the `TRANSOPTR` files with the $\boldsymbol{\sigma}$-matrix constraints already in the files and at the correct positions. By defining a standard header structure for these constraints, enabling parsing and interpretation of the `TRANSOPTR` system file by a `python` script, one can also program a sequence of optimizations to be carried

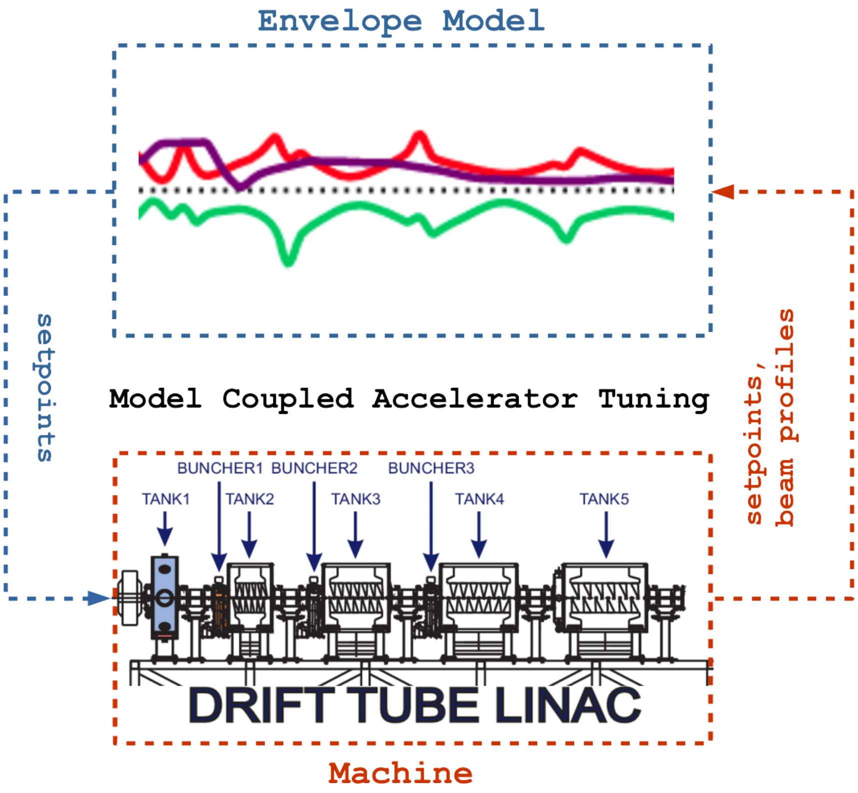

Figure 3.9: Conceptual representation of model coupled accelerator tuning (MCAT): an envelope simulation and optimization is carried out in parallel to machine operation, using diagnostic inputs in real time. The model optima are loaded into the control system, closing a feedback cycle between `TRANSOPTR` and the linac. DTL image obtained by Dr. M. Marchetto, TRIUMF.

out[64]. The header structure is printed as a `FORTRAN` comment in the `TRANSOPTR` source files when they are generated by `python`. Thus, groups of constraints upon the $\boldsymbol{\sigma}$-matrix can be added together at specific locations along the accelerator and associated with an identity. An example `XML` formatted constraint for the ISAC-OLIS beamline is shown in Figure 3.10. `TRANSOPTR` simulations of the OLIS section will contain the constraint at the appropriate location within the file `sy.f`. Sequential tune optimization[64] then proceeds by iteratively running `TRANSOPTR`, activating groups of constraints at each optimization, by uncommenting them. After each execution, the output data from `TRANSOPTR` is parsed by a python function, including the optimum device setpoints. The completed constraint group in the system file is commented and the next set is uncommented. This way, `TRANSOPTR` sequentially works from start to end along the accelerator, optimizing blocks of elements and moving on to the next group of constraints, until the process is finished.

```
<element id="mcat-out-of-olis" type="fortline" s="3334.66*mm" l="0.0*mm">
        <optr>ax=2.0 </optr>
        <optr>bx=65.0</optr>
        <optr>ay=-2.0</optr>
        <optr>by=bx</optr>
        <optr>brfq=1.0 !beta (x,y) for RFQ injection</optr>
        <optr>! MCAT-verb: out-of-olis</optr>
        <optr>!nlines: 3</optr>
        <optr>!call twissmatch(1,ax,bx,1.,1)</optr>
        <optr>!call twissmatch(3,ay,by,1.,1)</optr>
        <optr>!  return</optr>
        <notes>Olivier: Oct 26 2020 - parametrizing ILT tune for MCAT on-line</notes>
</element>
```

Figure 3.10: Example `XML` repository constraint upon the $\boldsymbol{\sigma}$-matrix: A specified Twiss parameter match for (x, y) at the location of profile monitor IOS:RPM8. The `FORTRAN` lines to be added to the `TRANSOPTR` files upon generation are located between the <`optr`> tags. Note that all constraints are commented with the `!` character, meaning the functions are disabled by default and do not hinder normal code operation.

The example in Fig. 3.10 includes two calls to the `TRANSOPTR` subroutine `twissmatch`, which attempts to match the $\boldsymbol{\sigma}$-matrix via the parameter $\mathcal{D}$ from Eq. (2.54). In this example, $\alpha_{x,y} = \pm 2$ and $\beta_x = \beta_y = 65.0\,\mathrm{mm/mrad}$ has been requested. Note that a (commented) `return` statement is included, which will cause the `FORTRAN` interpreter to skip the remainder of the file `sy.f` when the 3 lines of this constraint are activated (uncommented). This saves time otherwise wasted solving the envelope beyond the region of optimization. Using the constraint of Fig. 3.10, the optimum tune is computed algorithmically:

1. From a specified initial $\boldsymbol{\sigma}$-matrix and start/end coordinates along the beamline, the `TRANSOPTR` files are created from the `XML` repository.

2. The `python` function `MCATSequencer` is called, provided with instructions as to which sequence of optimizations to perform using those files.

3. The `TRANSOPTR` optimizations are run step by step by `MCATSequencer`.

4. The optimized values are returned by `MCATSequencer` after each step in the sequence and stored to a `redis` database for future reference.

5. (optional) When all steps are completed, the stored database list of optimized parameters is loaded into the control system.

During Step 2, the instructions which define the sequence of optimizations take the form of a `python` dictionary structured in a manner shown in Figure 3.11. The dictionary `MCATPV` contains keys (hashes) which define the optimization sequence steps and starts at 0. Each entry associated with the key is a list which starts with the human-readable string associated with the constraint group that will be uncommented at execution; the remainder of the list are the optimization variables. The sequence in Fig. 3.11 enables the constraint shown in Fig. 3.10 in `TRANSOPTR` and its optimizer finds values for the specified electrostatic quadrupoles. Finally, in Figure 3.12, a full sequential tune optimization command is defined, listing six separate optimizations to be performed from step '0' to '5'. The `MCATSequencer` function is called, provided this dictionary in addition to a uniform starting voltage (`startvol`), a specified integer maximum number of steps for the optimization and a temperature parameter for the simulated annealing routine. A temperature of zero disables simulated annealing and uses downhill-simplex instead. After execution, the `TRANSOPTR` input parameter file is updated with all optimized parameters. The execution sequence is graphically shown in Fig. 3.13.

The method of model coupled accelerator tuning (MCAT) is thus an alternative to reference tune scaling, capable thanks to `TRANSOPTR` of producing full accelerator tunes from first principles, not requiring previously saved values, only requiring beam initial conditions. As much of the present tuning time at TRIUMF-ISAC is dedicated to manual adjustment of the linac optics, tuning with a fast envelope code should in principle lead to a significant decline in tuning times. By computing the settings necessary to establish desired matching conditions upon the $\boldsymbol{\sigma}$-matrix throughout the lattice using sequential optimization, MCAT potentially reduces the complexity of linac tuning to that of steering the beam through the model optics. For this, model control of the accelerator must first be established.

```
    MCATPV = ({
        '0'     :      ['out-of-olis','IOS:Q4',
        'IOS:Q5','IOS:Q6*0','IOS:Q7','IOS:Q8'],

        '1'     :      ['out-of-olis','IOS:Q4',
        'IOS:Q5*0','IOS:Q6','IOS:Q7','IOS:Q8'],
    })
```

Figure 3.11: `python` dictionary used by `MCATSequencer` to define sequential optimizations, by uncommenting the appropriate lines in `sy.f`, along with lists of parameters to optimize. Two back-to-back optimizations labeled '0' and '1' are shown, both achieving the `out-of-olis` match from Fig. 3.10, with either quadrupoles Q6 or Q5 off, respectively. To each optimization step is associated a list whose first entry is the `MCAT-verb`, a human readable string which corresponds to the `TRANSOPTR` constraints in the `XML` repository. The remaining entries in the list denote quadrupoles slated for `TRANSOPTR` optimization.

```
def mcat_procedure_ios_ira(startvol,steps,temp):

    MCATPV={
    '0'  :   ['out-of-olis','IOS:Q4','IOS:Q5','IOS:Q7','IOS:Q8'],
    '1'  :   ['rfq-achromat1-rough','IOS:Q9','IOS:Q10','IOS:Q11'],
    '2'  :   ['prebuncher-line','ILT:Q34','ILT:Q35','ILT:Q36','ILT:Q37','ILT:Q41'],
    '3'  :   ['rfq-achromat2-rough','ILT:Q42','ILT:Q43','ILT:Q44'],
    '4'  :   ['rfq-ilt-periodic','ILT:Q48'],
    '5'  :   ['rfq-match','ILT:Q50','IRA:Q1','IRA:Q2','IRA:Q3','IRA:Q4'],
    }

    MCATSequencer(MCATPV,startvol,steps,temp)

    return 1
```

Figure 3.12: A full sequential tune optimization definition in `python`, which defines a series of six total steps, counting from zero. Each dictionary-key pair for `MCATPV` contains groups of variables, in this case quadrupoles in the OLIS, ILT and IRA lines, to be optimized. During optimization, `MCATSequencer` finds the relevant constraint in `sy.f` by matching the first element in each array (*e.g.* 'out-of-olis', Fig. 3.10). This constraint is activated in `TRANSOPTR` (uncommented), and the variables associated with each step are optimized (*e.g.* 'out-of-olis', OLIS quadrupoles Q4,5,7 and 8). The optimum values are fed back into the simulation, and the next group of variables are then optimized, until the entire sequence is complete.

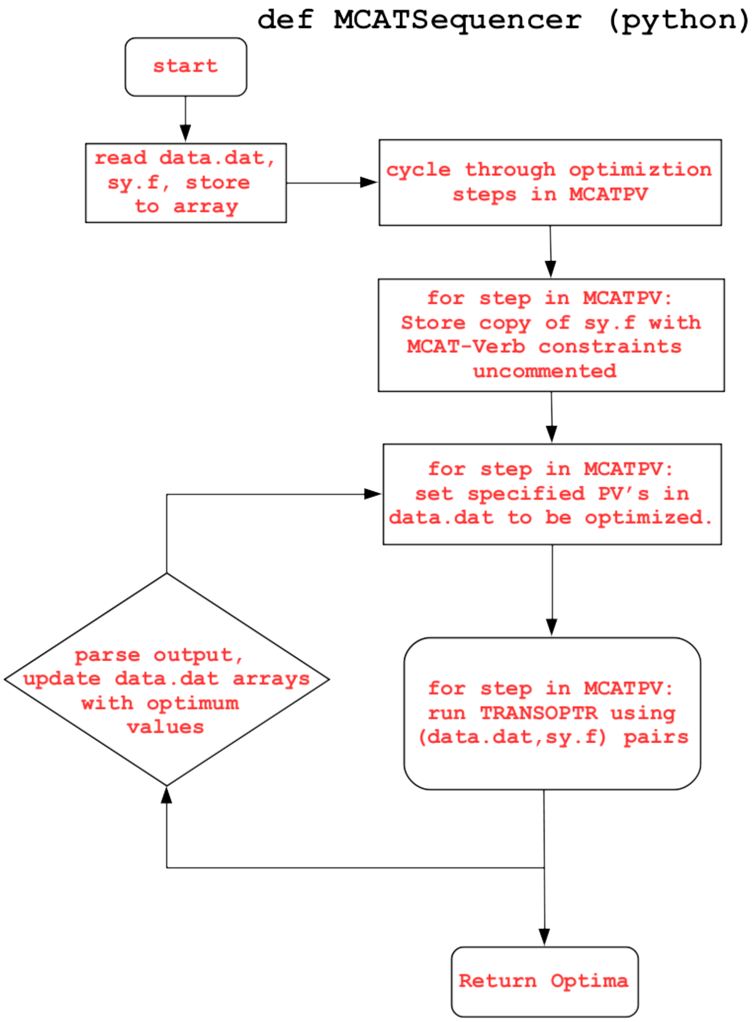

Figure 3.13: Flowchart representing `MCATSequencer` execution steps for sequential tune optimization with `TRANSOPTR`.

Chapter 4

The ISAC Linac in `TRANSOPTR`

`All models are wrong,`
`but some are useful.`

G.E.P. Box

As TRIUMF tackled the issue of designing and commissioning linear accelerators in the mid ’90s, the design effort turned to available accelerator simulation codes, in partnership with other institutions. The design history of the ISAC-RFQ has been documented by Koscielniak[65] and made use of a modified version of `PARMTEQ-M`, originally from Los Alamos, whose simulations were then used for beam-based commissioning[66]. The MEBT and HEBT sections were collaboratively designed with the University of Alberta[67, 68, 69, 70] and initial tunes were developed using `Trace-3D`. The ISAC drift tube linac design was itself the product of a collaboration between TRIUMF and the Institute for Nuclear Research of the Russian Academy of Sciences[10, 71] (INR-RAS). This saw the use of the newly developed code `LANA` for investigations of DTL beam dynamics[72]. The same code along with `Trace3D` were then used for the development of a high energy booster addition, the superconducting rf (SCRF) linac[36], made of a sequence of two-gap resonators[73]. The latter was designed in collaboration with INFN-LNL, the Italian Institute of Nuclear Physics[74].

`TRANSOPTR`'s envelope simulation and optimization capability is presented in this chapter, applied to the ISAC-I linac's low, medium and high energy sections: LEBT, MEBT & HEBT, allowing evaluation of entire start-to-end linac tunes, one of the main goals of this project. The ISAC-RFQ simulation was benchmarked[14] with the multiparticle code `PARMTEQ` and is presented in Section 4.1. Section 4.2 consists of an investigation of the MEBT design tune, which aims to understand why the ISAC-DTL quadrupole optics require manual tuning. The DTL envelope simulation was benchmarked with the multiparticle code `LORASR` and published in *Physical Review Accelerators and Beams*[16], presented in Section 4.3.

4.1 `TRANSOPTR` ISAC-RFQ Implementation

The infinitesimal transfer matrix (3.73) for the 2-term RFQ requires knowledge of the vane modulation, via the parameters (A_{01}, A_{10}), which depend upon (a, m, k), the modulation indices. An `ascii` formatted file containing (s, a, m, k) is all `TRANSOPTR` needs to compute the elements $\mathcal{A}_{\pm}$, $\mathcal{B}$ and $\mathcal{C}$ from Eqs. (3.74), (3.75) and (3.76). For the ISAC-RFQ, this was stored in a 298 line text file, which is plotted in Figure 4.1, showing vane modulation parameters for the 760 cm long structure. Typical RFQ multiparticle simulations proceed half-modulation by half-modulation, also referred to as cells. For example, in codes like `PARMTEQ`, the longitudinal coordinate always spans $[-\pi, \pi]$, with k constant over a half modulation. However, this causes discontinuities in k at the cell interfaces. This is a consequence of adiabatic approximation in an RFQ, where the modulation wavenumber k is varied across the structure slowly enough to be treated as a constant. This results in discontinuities in k at the cell interfaces. In practice, it is a matter of designing a sufficiently progressive variation in k along the structure, to minimize kicks due to discontinuities.

$$\nabla^2\phi_{RFQ} = \begin{cases} 0, & \text{inside cell} \\ \neq 0 & \text{cell interfaces} \end{cases}$$

`TRANSOPTR`'s global integration makes it awkward to handle a stepwise discontinuous value like k. Instead, the continuous spatial phase $\psi(s)$ of Eq. (3.70) is used. A table of the parameters (s, a, m, k) in the RFQ is interpolated in `TRANSOPTR` using a cubic spline.

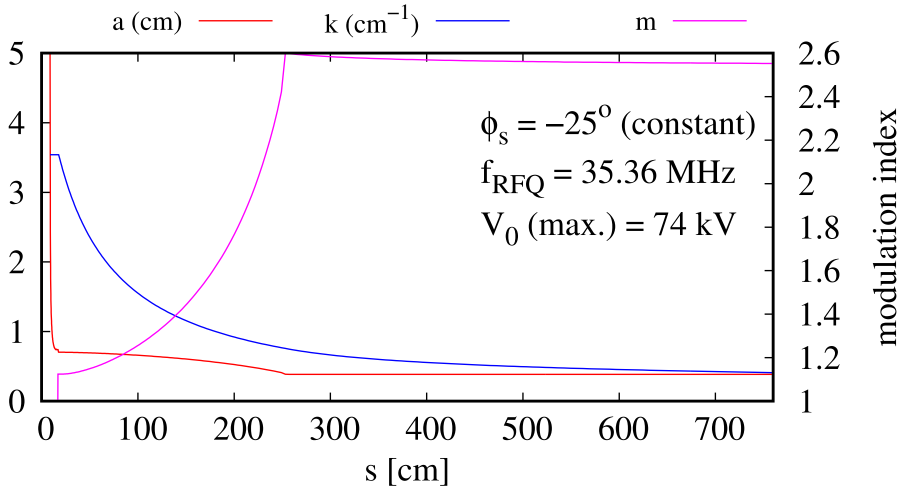

Figure 4.1: ISAC-RFQ vane modulation parameters, showing both the aperture a and the longitudinal wavenumber k to the left hand y-axis. The transverse modulation depth index m is shown to the right hand y-axis. The ISAC-RFQ is designed with a constant synchronous particle phase held at -25°[14].

4.1.1 ISAC-RFQ `TRANSOPTR-PARMTEQ` Benchmark

Comparative envelope simulations between `TRANSOPTR` and `PARMTEQ`, for an identical starting beam distribution from Table 4.1, are shown in Figure 4.2. Another important distinction inherent to the `TRANSOPTR` implementation is the linearity of the RFQ forces, represented in the F-matrix (3.73). This means that nonlinear effects

Parameter	Unit	Value
V_0	[MV]	3.520×10^{-2}
E_i	[MeV]	2.871×10^{-2}
m_0	[MeV/c^2]	13041.020
α_{xy}		4.000
β_{xy}	[mm/mrad]	80.000
ϵ_{xy}	[mm mrad]	3.000
α_z		0.026
β_z	[rad/MeV]	1.784
ϵ_z	[rad MeV]	5.750×10^{-9}

Table 4.1: `TRANSOPTR` RFQ simulation parameters as used in Figure 4.2, for ^{14}N. The parameters α_{xy},β_{xy} and ϵ_{xy} are the input Twiss parameters for the x and y dimensions, while subscripts z denote longitudinal[14].

upon the phase space beam distribution are not represented in optr; the multiparticle regimen includes them. When the beam envelope remains small and near axis where the RFQ field is linear, both models agree better than for cases where the beam is large compared to the aperture. Emittance growth due to nonlinear bunch distortions, as discussed in Section 2.6, are not represented in `TRANSOPTR`. Figure 4.3, shows the phase space beam distributions for both `PARMTEQ` and `TRANSOPTR`, with the latter displaying a 2 rms containment ellipse of area $A = 4\pi\epsilon_{rms}$. The top row of the figure shows the input beam distribution, the middle row shows the output.

As a further test, the `TRANSOPTR` ISAC-RFQ had its voltage decreased from the optimum value of V_0 for an $A/q = 30$ beam, shown in Figure 4.4. The reference particle energy rapidly fell to zero starting at 93% of the optimum V_0. Previous investigations[75], both in `PARMTEQ` and on-line, found the ISAC-RFQ transmission sharply falls to zero when the voltage is set to 92%. The RFQ envelope model agrees remarkably well with this cutoff voltage. Though the effects of nonlinearities may be seen in Fig. 4.3, middle's (ϕ, E) plot, the core of the distributions remain in agreement, in terms of orientation, evidencing the region of linear response in the multiparticle simulation. The transverse dynamics of the displayed RFQ simulation are very well

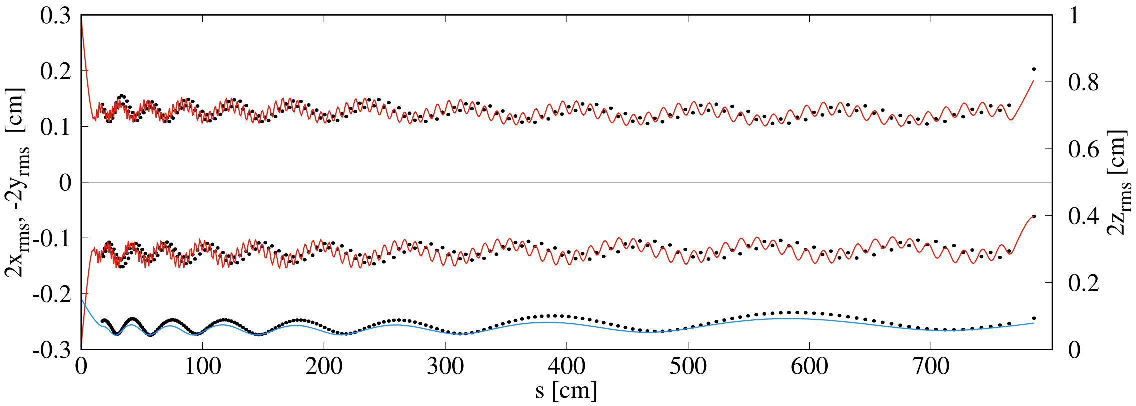

Figure 4.2: ISAC-RFQ comparative envelope simulation for a $^{14}N^{+}$ beam accelerated from 28.56 keV to an output energy of 2.15 MeV. The `PARMTEQ` 2 rms beam size through the RFQ are shown as black dots, while the `TRANSOPTR` simulation envelopes of the same beam is shown as solid lines. Observe the disagreement between transverse oscillations between both models, arising from the continuous treatment of k in `TRANSOPTR`, while it is stepwise increasing in `PARMTEQ`. Input beam parameters, used for both simulations, are shown in Table 4.1[14].

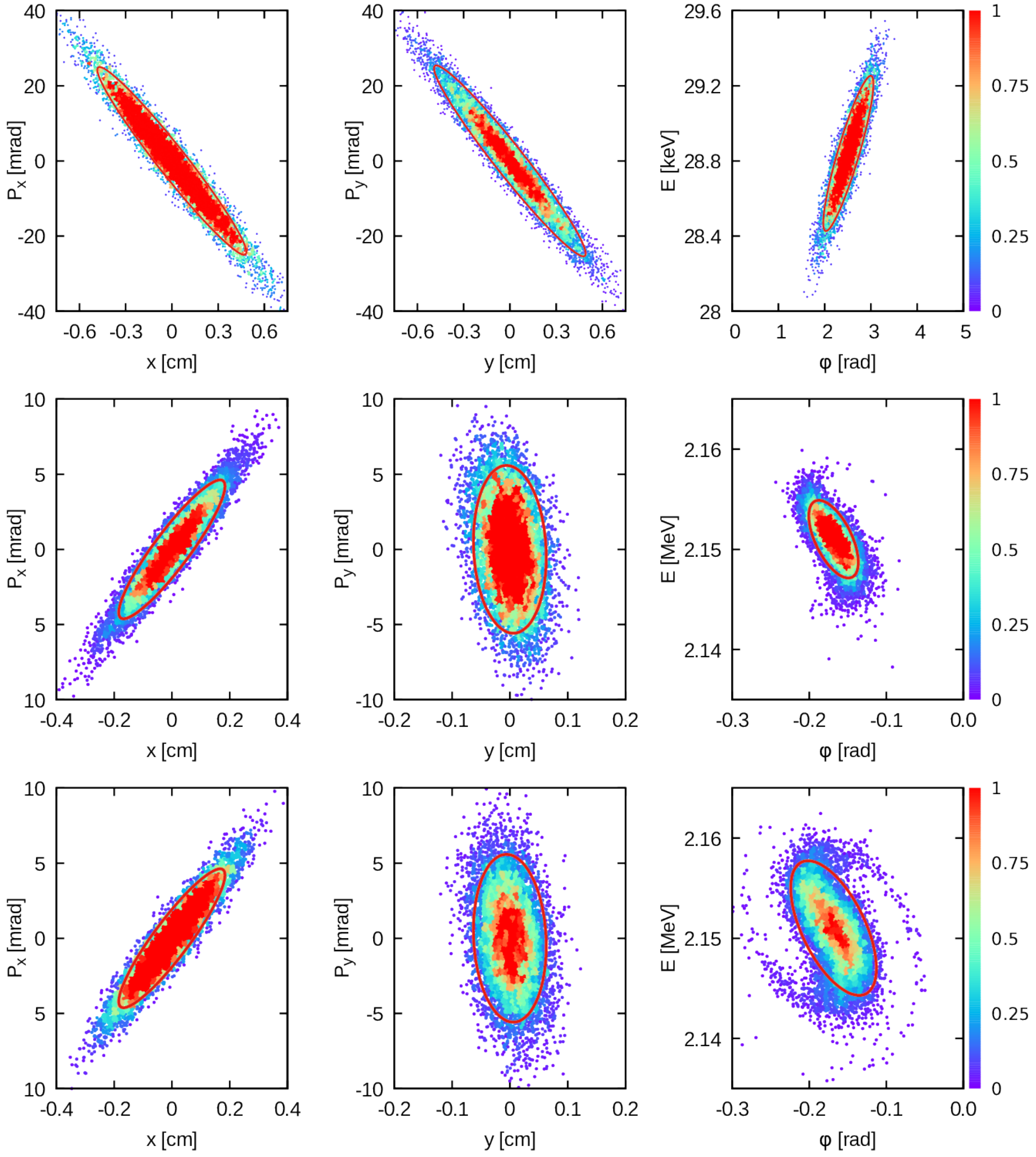

Figure 4.3: Benchmark comparison between `PARMTEQ`, showing a normalized particle density distribution overlaid with `TRANSOPTR`'s beam containment ellipse, which corresponds to to 86% containment assuming a Gaussian beam distribution. Injected (x, P_x), (y, P_y) and (ϕ, E) phase space distributions shown in the top row and the output in the middle row. The bottom row shows the effects of tripling the injected longitudinal distribution's emittance, causing filamentation, which is not represented in `TRANSOPTR`. The simulations start and end at the edges of the RFQ's vacuum tank[14].

described by first order optics, seen in each of the (x, P_x) and (y, P_y) plots in the figure. As a demonstration of the differences between models, in the last row of Fig. 4.3, the input longitudinal emittance has been tripled. The `PARMTEQ` simulation predicts distortion and filamentation, while the `TRANSOPTR` model does not. Nevertheless, the majority of the beam distribution is still contained in the 2 rms ellipse. Though the modelling of nonlinearities is an essential part of RFQ design, for an already built machine, in the context of accelerator tune computations, a first order treatment is sufficient, since optimal tunes will seek to keep the distribution contained in the linear zone.

For tune computation in an existing machine, the envelope method is particularly powerful due to its speed. Figure 4.5 shows an $A/q = 30$ beam from OLIS, optimized using `MCATSequencer` (Section 3.10) through the low energy section and into the RFQ. For this example, the 3-harmonic pre-bunching has been simulated by first running a continuous beam from OLIS up until the location of the pre-buncher device (arrows on Fig. 4.5), then simulating a bunched beam from there until the simulation end at linac injection. The longitudinal bunch length z is set to the $\beta\lambda$ value for the 11 MHz fundamental of the pre-buncher, at $E/A = 2.04\,\mathrm{keV/u}$. The momentum spread is set to the maximum deviation of the three-harmonic waveform to that of a perfect sawtooth[16]. The initial value for P_z is made equal to the ratio of the device's voltage to the source bias, typically a few hundred volts compared to kilovolts. The ability in `TRANSOPTR` to compute continuous low to medium energy tunes for the ISAC accelerator in a single simulation is novel.

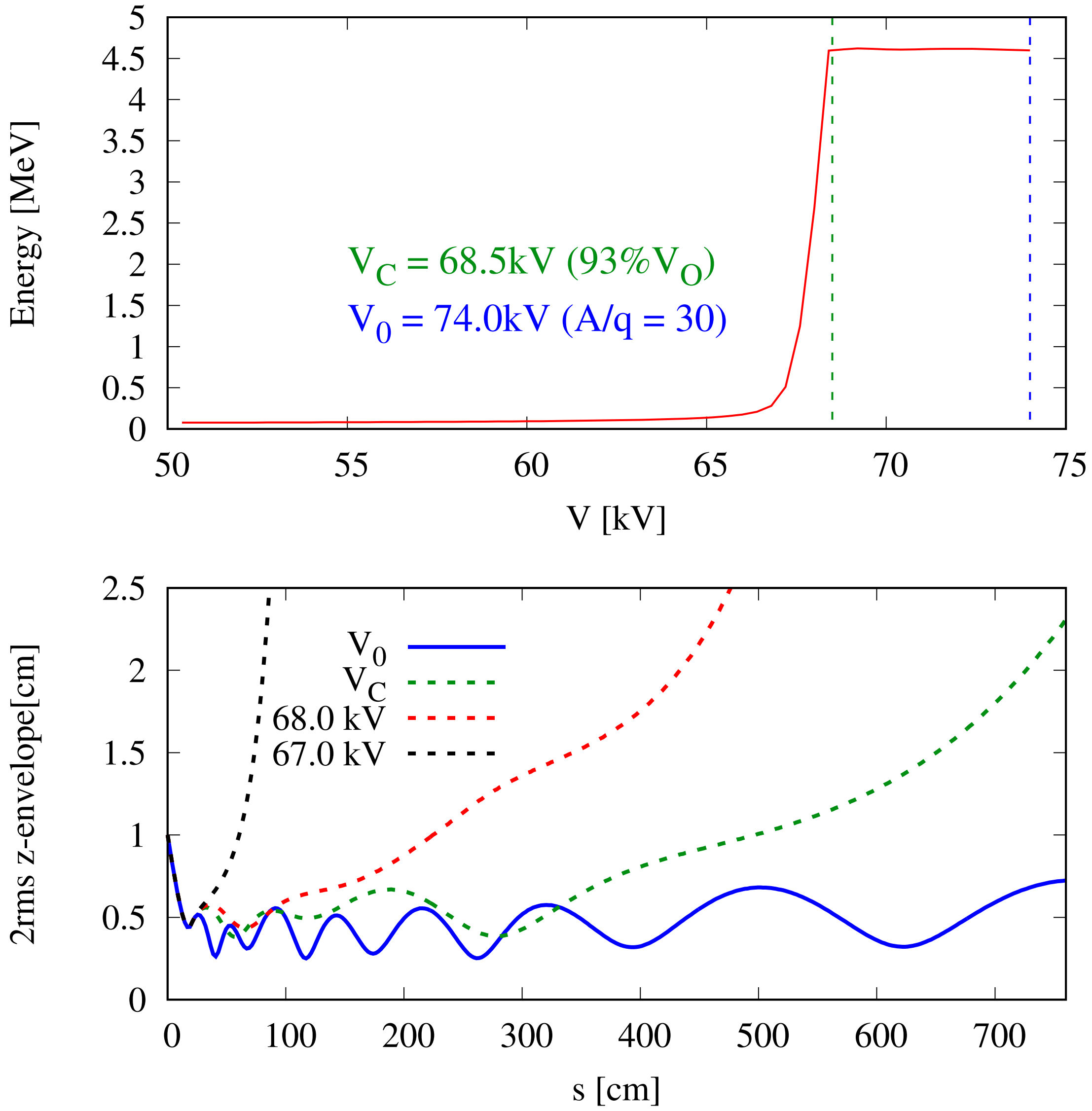

Figure 4.4: **Top:** `TRANSOPTR` simulated reference particle energy output from the ISAC-RFQ vs. vane voltage for an $A/q = 30$ beam. The reference particle energy reaches its design value (4.59 MeV) at a cutoff voltage V_C which is 93% of the optimum voltage V_0 needed to maintain bunch coherence longitudinally. **Bottom:** optr-computed z-envelopes for V_0, V_C and lower, showing the rapid growth in longitudinal envelope size, which would lead to transmission loss since it exceeds the length of RFQ cells, causing bunch decoherence. `TRANSOPTR` does not represent this effect.

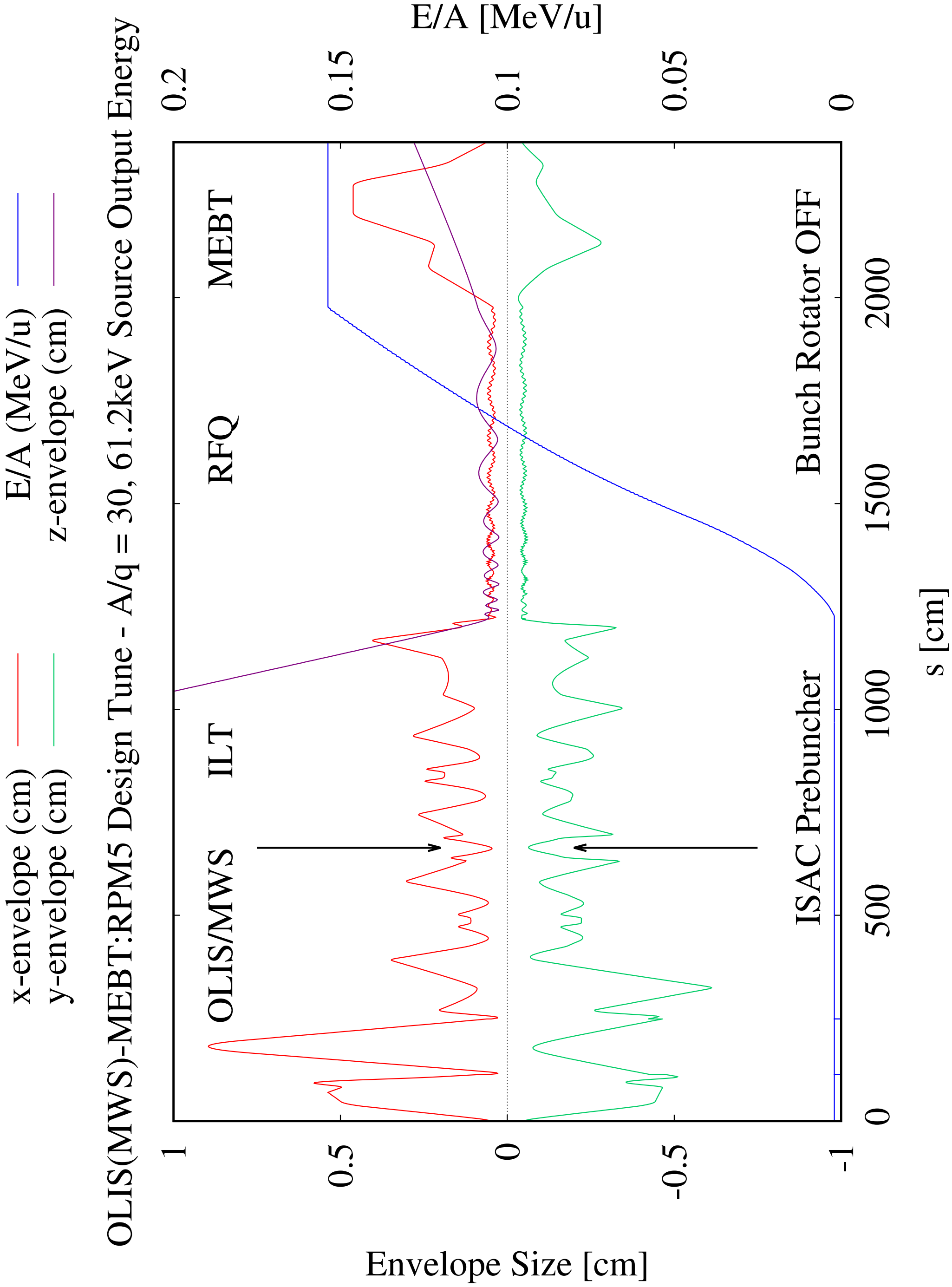

Figure 4.5: Composite `TANSOPTR` 2 rms envelopes from OLIS MWS to MEBT Faraday Cup 5 (MEBT:FC5). Beam undergoes RFQ acceleration from low to medium energy sections. For longitudinal dynamics, a bunch of length $z = \beta\lambda$ is initiated at the ISAC pre-buncher (highlighted), keeping the transverse dimensions of the continuous OLIS beam at that location[76].

4.2 The ISAC-MEBT Section in `TRANSOPTR`

On-line beam development carried out between 2020 and 2022 investigated the MEBT optics using the `TRANSOPTR` model[77]. This included extracting RFQ output initial conditions using a tomographic reconstruction method[78, 77]. While it was possible to establish good agreement on the RFQ output leg of the section, the DTL injection leg after the corner presented challenges. In particular, persistent need for strong vertical steering is found necessary to transmit beam through the corner. This can partially be explained by shifting and cracking floor slabs, under the stress action of the ISAC-I experimental hall foundations settling in the two decades after its construction. There are visible fissures in the concrete that have appeared over the years[63], requiring sealing to prevent water infiltration.

However, these are expected to cause misalignments on the order of roughly 0.5 cm in the beamline, consistent with the observed on-line steering corrections typically used by operations[63]. What cannot be explained by alignment issues of this magnitude are observed transmission drops between MB2, the second dipole in the corner, and the Faraday cup at DTL Tank-1 injection, typically below 70%, with the horizontal inter-dipole charge selection slits completely open. This transmission loss cannot be explained by alignment issues alone. The observed transmission loss in MEBT is indicative of a deviation between machine and model, in either beam or transfer matrices. In this section, the `TRANSOPTR` model of the MEBT section[17] has been used to perform an analysis of the design tune of the machine which is presented and discussed. The MEBT corner (Fig. 4.6) is scrutinized. The aim of this investigation is to understand the cause of these on-line difficulties, which in-turn bring about further issues with the DTL.

4.2.1 Tune Eccentricity

Distances between the effective edges of the MEBT quadrupoles are shown in Figure 4.7. The inter-quadrupole drift distances are measured in units of the beam doubling distance, equal to 17.3 cm in MEBT (Section 3.4, Figure 3.2). This is chosen since it is the strongest constraint upon the envelopes in the MEBT section and so will be most sensitive to errors. Since the slit has a 2 mm opening in the local horizontal plane[79]

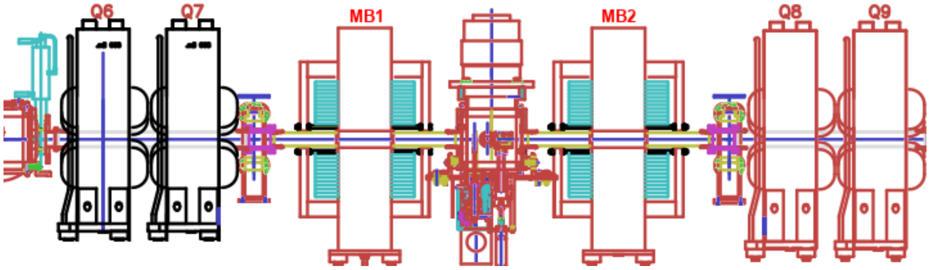

Figure 4.6: The ISAC MEBT corner, which is shown here as a straight sequence of elements. The dipoles MB1 and MB2 are separated by a vacuum box containing beam diagnostics and horizontal charge selection slits. Quadrupoles Q6, Q7 are mirror symmetric about the inter-dipole midpoint to Q8 and Q9. Beam propagates from left to right. The dipole magnets themselves are rectangular, but are angled with respect to the reference orbit to produce a 22.5° edge in the x-z plane. Obtained from TRIUMF Design Office.

(tilted at 45° with respect to the lab frame), it presents a strong transmission constraint requiring operators detune some quadrupoles to restore transmission through the aperture. The MEBT tune and quadrupole tip-fields are shown in Figure 4.8, for an $A/q=6$ beam. Note the chopper-slit waist (arrows in the figure) is reproduced in the x-plane at the midpoint between dipoles MB1 and MB2. Next, it is imaged at the rebuncher using Q8 and Q9, while the last quadrupoles reproduce the spot mid Tank-1. The optics must be able to precisely reproduce this image at three locations.

A stripping foil between quadrupoles 5 and 6, near the chopper slit, enables charge state increase if needed, but the foil scattering will increase the emittance, particularly by increasing the transverse bunch momentum, an effect which the round waist seeks to minimize. The key issue with the MEBT design tune lies just downstream of the foil: The large growth in x-envelope between the chopper-slit waist and the entrance of quadrupole Q7, where x increases by nearly a factor of 10, as shown in Figure 4.9. In turn, this induces severe eccentricity upon the (x, x') distribution, evidenced by the saturation of the parameter r_{12}, which reaches near unity. The beam distributions in (x, x') and (y, y') at Q7 are shown on the left of Figure 4.10. A notably large drift exists between quadrupoles Q7 and Q8 (Fig. 4.7), which define the MEBT corner. Strictly speaking, there are no quadrupoles between Q7 and Q8, however the rectangular MEBT dipoles are positioned to create an edge angle of 22.5° in the x-plane, which produces a transverse focal effect[40] described by Eq. (3.47). However, the operator has limited control over this, as it is trajectory dependent.

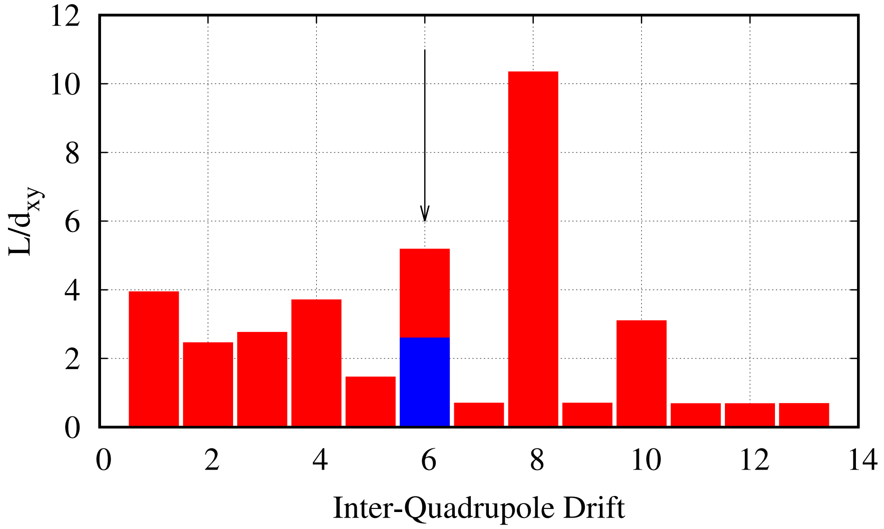

Figure 4.7: MEBT section inter-quadrupole drift distances (L), measured with respect to the doubling distance d_{xy} formed at the chopper slit waist[17], which is the smallest envelope constraint in the MEBT tune. The value of L is obtained by measuring the centerpoint to centerpoint distances, minus one quadrupole effective length. Horizontal axis number denote quadrupoles where each drifts end. Since the slit is located midway between Q5 and Q6, the quad-to-slit distance in either case is half of the Q5-Q6 drift. This is shown as the blue bar.

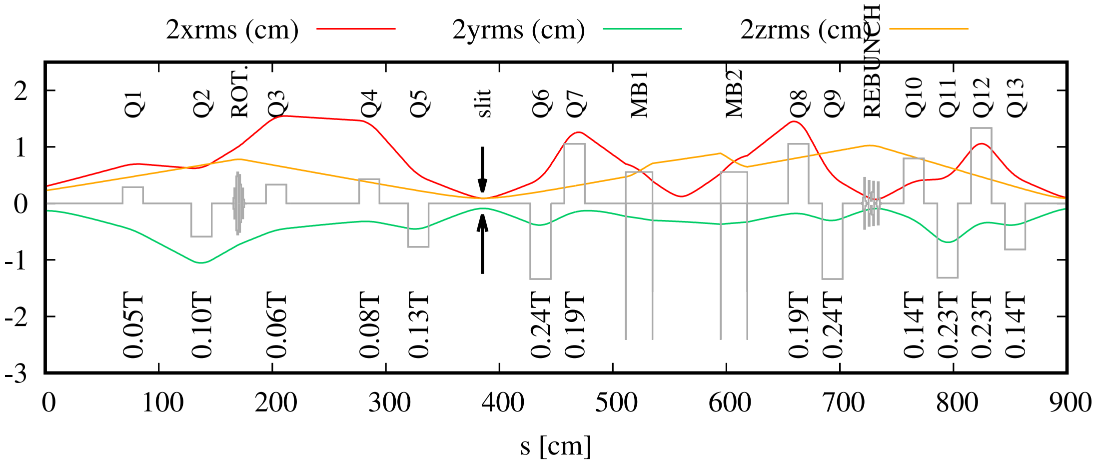

Figure 4.8: MEBT tune[17] in `TRANSOPTR`, from RFQ exit up to DTL injection, for an $A/q = 6$ beam at $E/A = 0.153\,\mathrm{MeV/u}$. The rebuncher (REB.) time focuses into DTL Tank-1. Chopper-slit indicated with arrows. The absolute value of quadrupole tip-fields is displayed at the bottom of the graph. Arbitrary strengths in grey.

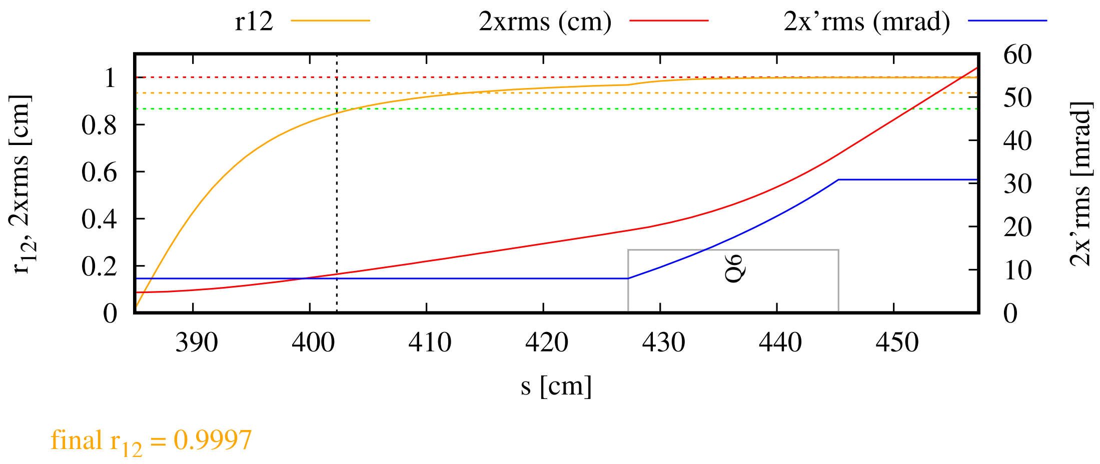

Figure 4.9: 2 rms (x, x') envelopes and r_{12}, from MEBT chopper slit until the start of MEBT:Q7. Colored dotted lines indicate $r_{12} = 0.866$ (green), $r_{12} = 0.933$ (yellow) and $r_{12} = 0.999$ (red). Computed r_{12} parameter at quadrupole Q7's start listed at the bottom of the plot.

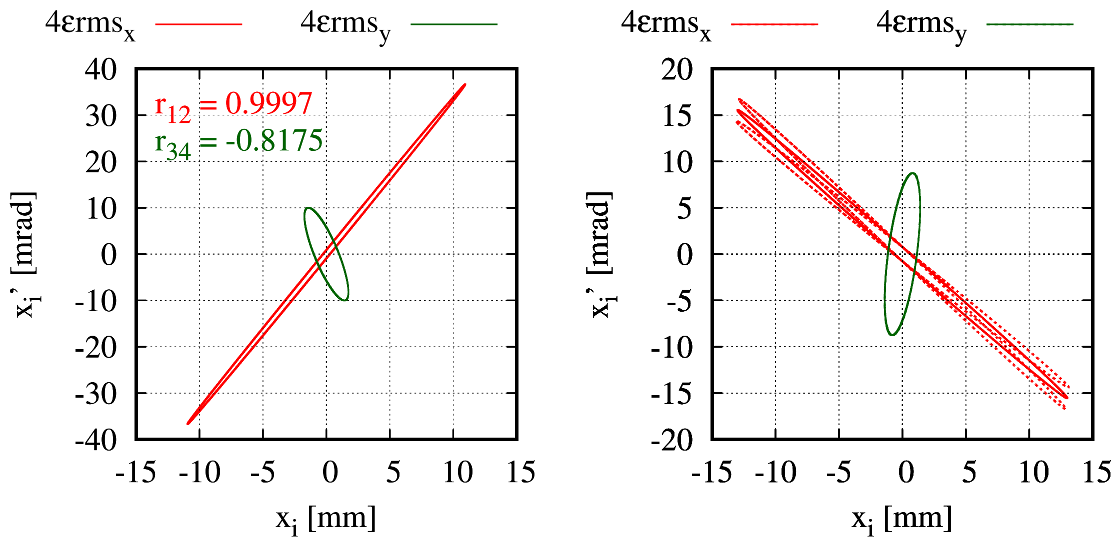

Figure 4.10: **Left:** 4ϵ rms (x, y) beam containment ellipses computed in `TRANSOPTR` at the start of quadrupole MEBT:Q7's field. The correlation coefficients r_{12} and r_{34} are indicated. **Right:** The left distribution has been transformed through Q7, and the effect of a $\pm 5\,mT$ quadrupole tip-field error is shown as dotted lines. The error is too small in the vertical dimension to be seen.

The horizontal distribution (Fig. 4.10, left) is particularly eccentric, with its semi-major axis now dominating the semi-minor, in contrast to the vertical which itself has undergone a doubling in size since the chopper-slit, but remains more round. Figure 4.11 shows the correlation coefficients in the corner and downstream. Horizontal envelopes through the corner (Fig. 4.8) produce single particle trajectory-like straight lines, discussed in Section 3.4, evidencing this long drift. Per Section 2.6, one expects the horizontal envelope downstream will be particularly sensitive to quadrupole gradient errors, with the potential for the emergence of a mismatch. This is also significant since the drift after Q7, per Fig. 4.7, is the largest inter-quadrupole distance in the entire section, 5 doublings in size between either of Q7 or Q8 and the central x-waist in the corner. Thus, we also expect that the precise location of this waist will be quite sensitive to the exact setting of Q7.

The effects of a $\pm 5\,mT$ field error in Q7's field upon the $\boldsymbol{\sigma}$-matrix is shown at the right of Figure 4.10, producing a transformation error mostly in x', as a consequence of the high value of r_{12} at the quad's entrance together with the broad size in (x, x') (Fig. 4.11). The error in the vertical plane is much smaller, being imperceptible on the comparable scale shown in the figure, highlighting the lesser sensitivity to field errors

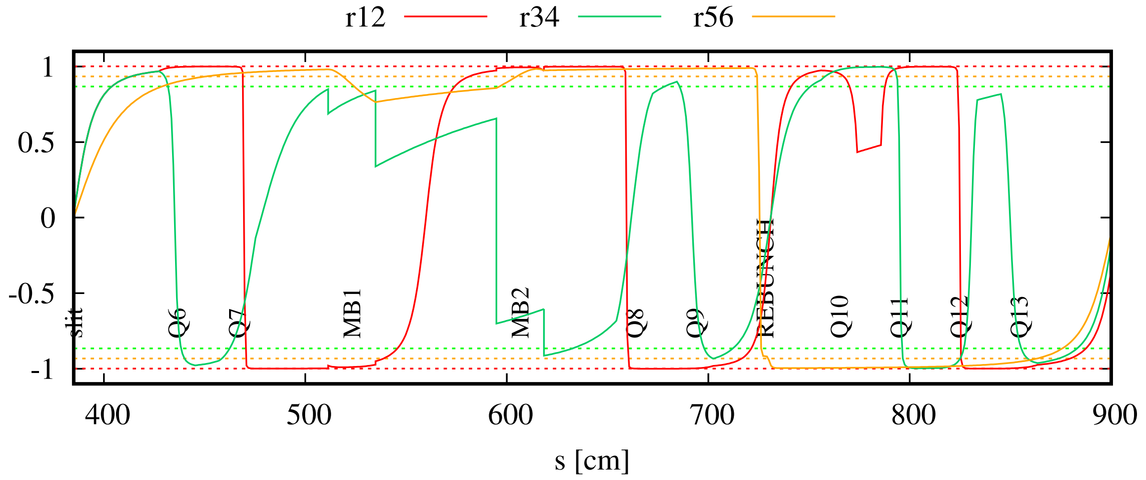

Figure 4.11: Beam matrix correlation coefficients between canonical coordinates in TRANSOPTR, showing strong transverse correlations r_{12} and r_{34}. An A/q = 30/5 beam has been used at E/A = 0.153 MeV/u. Colored dotted lines indicate $r_{ij} = 0.866$ (green), $r_{ij} = 0.933$ (yellow) and $r_{ij} = 0.999$ (red). Simulation starts at MEBT chopper-slit

at lower distribution eccentricity and size. The horizontal momentum error out of Q7 in such cases is significant. A Monte-Carlo simulation consisting of 250 iterations applying a Gaussian random error of up to ± 5 mT tip-field on each quadrupole is shown to the left of Figure 4.12. The consequences of the momentum error in Fig. 4.10 cause the emergence of a mismatch downstream of the corner and into the DTL. The parameters $\mathcal{D}$ from Eq. (2.54) for each of the 250 iterations are shown for x and y to the right of Figure 4.12, evidencing a principally horizontal mismatch into the DTL. The on-line observation of transmission loss between the MEBT corner and Tank-1 is likely explained by the mismatch shown in Figure 4.12, in which the x-envelope's size can vary appreciably at Q12 (Fig. 4.12, left, $s \approx 450$ cm). For cases where the x-envelope is broadened, either due to quadrupole field errors or even a mismatch at the chopper-slit, this large horizontal envelope will be more sensitive to vertical alignment through the 2" (5.08 cm) diameter MEBT vacuum beam pipe, supporting the known requirement for strong vertical steering in the MEBT section and corner[63] and supported by the observation that setting downstream DTL model gradients results in poor transmission, when MEBT is strictly set to model computed values.

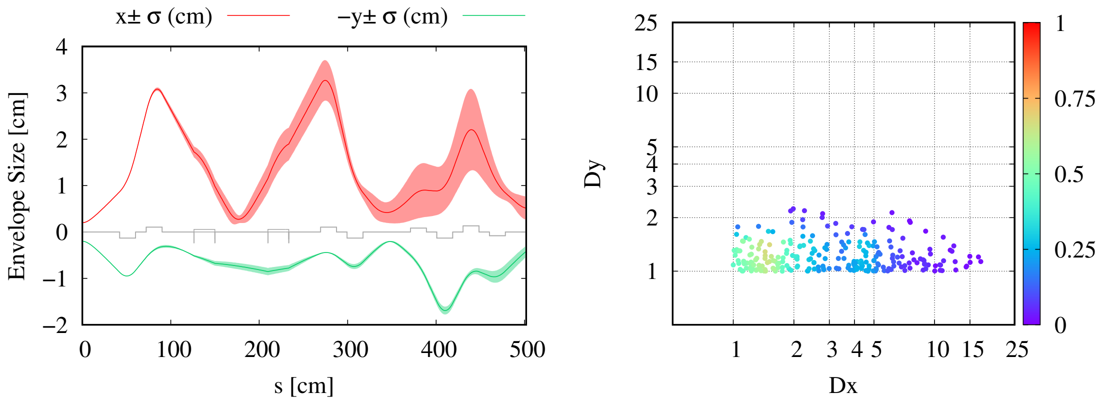

Figure 4.12: **Left:** Transverse envelope mean and variance for a randomly computed ± 5 mT Gaussian distributed quadrupole tip-field errors, obtained after 250 iterations. **Right:** The Bovet mismatch parameters $\mathcal{D}$ from Eq. (2.54) have been computed at each iteration for (x, y) with respect to the design tune. The local density of points is shown on the colorscale, on a relative scale from [0,1].

4.2.2 Chromaticity of the MEBT Corner

The MEBT 90° bend section is singly, not doubly achromatic[75] (Section 2.5), owing to the absence of inter-dipole quadrupoles in its final design[80]. This means that the dispersion[31] function will be nonzero downstream. Chromatic effects in the $\boldsymbol{\sigma}$-matrix cause the smearing of quadrupole foci[31], causing the emergence of tails in the transverse distributions (halo), which in the presence of apertures can cause further transmission losses. Additionally, the chromaticity of the corner causes the emergence of correlations between dimensions 1,2 and 5,6, as shown in Figure 4.13. Since the longitudinal distribution in the corner is defined by the bunch rotator cavity, variation of its parameters or even those of the ISAC-RFQ may affect the transverse envelopes in and beyond the corner. This translates to nonzero values for σ_{15}, σ_{16}, σ_{25} and σ_{26}, coupling the horizontal and longitudinal phase spaces and deviating from the ISAC-DTL design tune[71] assumption of an uncoupled injected beam. These effects cannot be tuned away and are inherent to the design. While the eccentricity and large x-envelope size in the tune cause a sensitivity upon the precise quadrupole gradients, the chromaticity couples longitudinal energy spread out of the RFQ and rotator rf settings to the horizontal size. Diurnal temperature correlations to the rf phases observed at ISAC-I[81] can potentially couple to the transverse beam size out of MEBT, inducing temperature-transmission correlations, observed at ISAC-I and reported in[12].

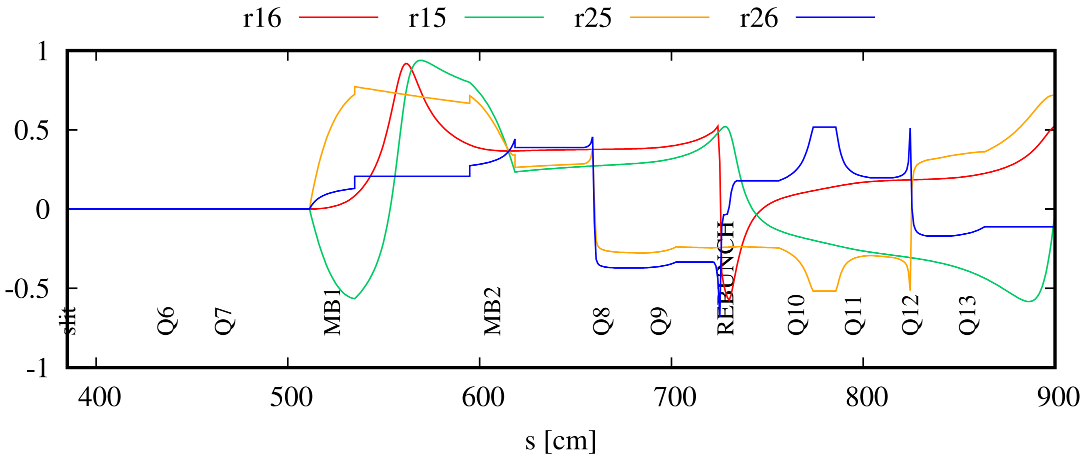

Figure 4.13: Beam matrix correlation coefficients between canonical coordinates in `TRANSOPTR`, showcasing chromatic couplings downstream of the MEBT corner. These persist into the DTL. An $A/q = 6$ beam has been used at $E/A = 0.153\,\mathrm{MeV/u}$.

4.2.3 DTL Injection Mismatch

The presented observations suggest that the tune around the corner is quite sensitive to small errors in quadrupole field gradients. There are no field readbacks in the MEBT optics, rendering the value of each device's gradient uncertain. Use of relatively long quadrupoles given the local E/A and $A/q \leq 6$ limitation produces tunes with low tip-field requirements when compared to the magnetization and hysteresis errors. This leads to a mismatch condition into the ISAC-DTL, shown in Figure 4.14, causing beam losses through the linac. Using shorter effective length devices would in turn force higher tip-fields for equivalent focal strength, diminishing this sensitivity. The section's power supplies are also unipolar, rendering device degaussing more difficult. The identified sensitivity has led to the initiation of an investigation of the MEBT optics, with work underway to begin a re-surveying of the quadrupole magnetic fields. Once completed, this will allow testing of MEBT section tuning using better representations of the true quadrupole focal effects, which have up to the present been described with the same B-I fit. This work is guided using the `TRANSOPTR` model of the section, developed and presented herein. Finally, it was observed during model tests on-line in 2020 and 2021 that the MEBT bunch rotator systematically overfocuses at the stripping foil for $A/q \leq 4.5$[82], thereby broadening P_z, likely exacerbating these issues at lower A/q, given the chromaticity of the corner. Solutions to the MEBT issue can be broken down into three categories: short, medium and long term. Short term palliation of the mismatch caused by MEBT is presented in the next chapter, matching MEBT manually into the `TRANSOPTR` model-optimized DTL optics. This effectively reverses the present operational doctrine, in which MEBT optics are set exactly to model values, then the entire DTL lattice is manually tuned for transmission. In the intermediate term, precise knowledge of the MEBT quadrupole tip fields would allow the tuning of the section without relying upon B-I calibrations, which are susceptible to things like hysteresis errors or variations in quadrupole calibrations between devices. Finally, in the longer term, a full redesign of the optics, using shorter quadrupoles which will require higher gradients, minimizing the effects of hysteresis and residual magnetization errors. A redesigned corner should also produce a doubly achromatic output, which will eliminate downstream transverse-longitudinal couplings, which in turn can help mitigate diurnal transmission losses. This will allow model coupled tuning of the MEBT section, not presently feasible.

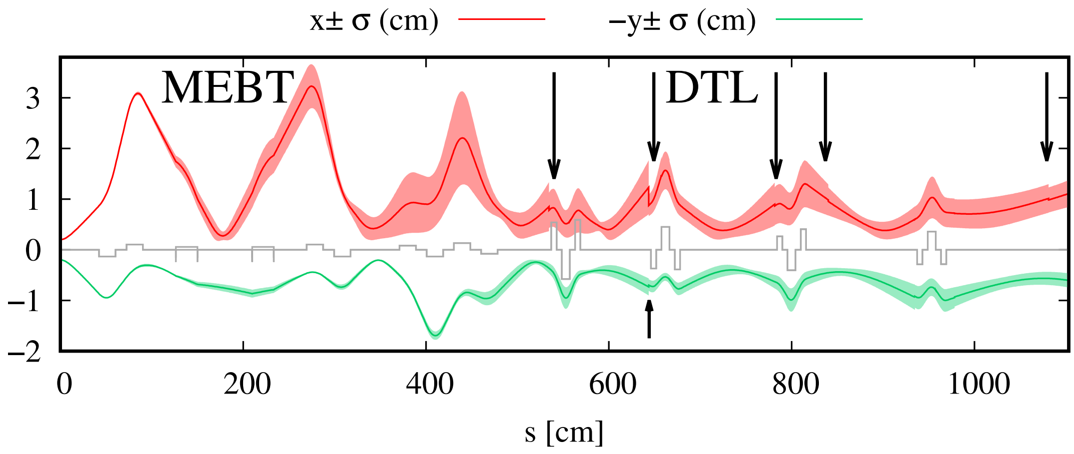

Figure 4.14: A Monte-Carlo simulation in `TRANSOPTR` in which a ± 5 mT Gaussian random error is applied to each quadrupole tip-field, for 250 iterations. The mean (solid line) and variance (shaded area) of the envelopes are shown. Beam starts at the round waist at the MEBT chopper slit and ends at the exit of the ISAC-DTL. Slit apertures have been simulated inside the DTL structure using the `TRANSOPTR` subroutine `slit`[83]. The mismatch leads to aperture collisions (arrows) principally in x, the dispersive plane, causing transmission loss.

4.3 `TRANSOPTR` Drift Tube Linac Implementation

Unlike the RFQ, where the beam dynamics emerge from the vane modulations, the DTL consists of several independently controlled multigap cavities, with differing drift tube structures and therefore fields $\mathcal{E}(s)$. The addition of the ISAC-DTL to `TRANSOPTR`[16] makes use of the axially symmetric field F-matrix (3.62) derived in[44]. Simulation of inter-cavity phasing effects nevertheless required the modification of `TRANSOPTR`'s source to enable global time tracking[84], which was previously not done outside of rf cavities. From machine blueprints, the global layout of the lattice were measured, providing element center-point locations and dimensions for the model. Original surveys of the DTL triplet quadrupoles were analyzed to obtain their effective lengths and B-I calibrations[63]. The on-axis fields $\mathcal{E}(s)$ were generated by building a model in the Poisson solver `Opera2D`[15]. Finally, the DTL energy vs. phase relationship was measured on-line with an $^{16}O^{4+}$ beam over a 48 h beamtime, providing a first full measurement of the characteristic E/A response of the ISAC-DTL. This enabled the establishment of a calibration between the `TRANSOPTR` model and the control system voltage parameters, presented in Section 5.3.

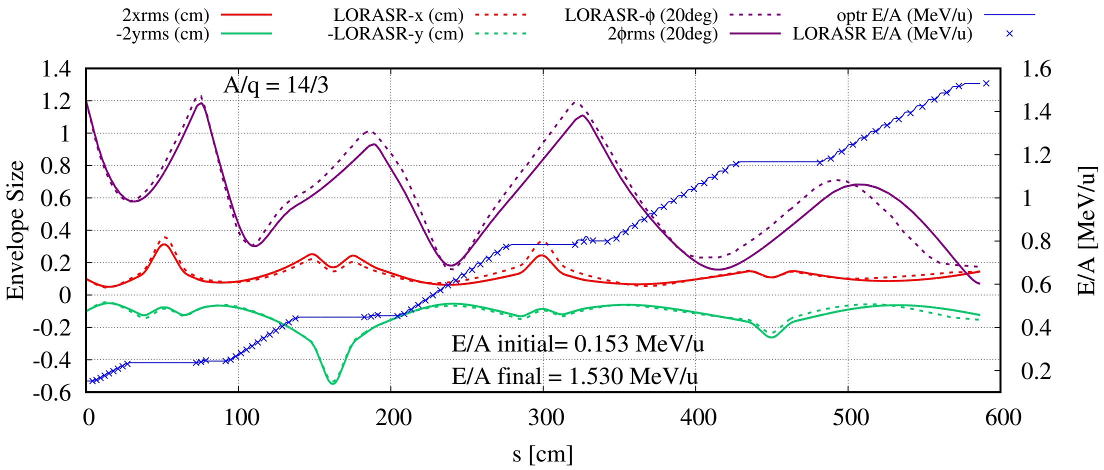

Figure 4.15: Comparison of 2 rms (x, y, z) envelopes in `TRANSOPTR` and `LORASR` through the ISAC-DTL, set for full operational acceleration at $E/A = 1.53\,\mathrm{MeV/u}$[16]. In this plot, the (x, y) conventions are reversed with respect to the machine.

4.3.1 ISAC-DTL `TRANSOPTR`-`LORASR` Benchmark

Verification of `TRANSOPTR`'s ISAC-DTL capability was carried out using the multiparticle code `LORASR`[85], developed at IAP-Frankfurt and ubiquitously used[86] for IH-DTL beam dynamics investigations. Figure 4.15 shows the comparison between 2 rms containment envelopes for both codes, using an identical starting distribution[16] listed in Tab. 4.2. In both cases, the linac has been set for full operational E/A output at 1.53 MeV/u. Each drift tube in `LORASR` has been individually tuned to match the effective voltage computation predicted by `TRANSOPTR`. The (z, P_z) phase space evolution of the `LORASR` distribution and `TRANSOPTR` ellipse are shown in Fig. 4.16.

`TRANSOPTR`'s optimizer was also used to define the transverse tune in Fig. 4.15 by way of the magnetic quadrupoles. This was accomplished by requiring $\mathbf{M}_{11} = \mathbf{M}_{33} = \text{-}1$ and $\mathbf{M}_{12} = \mathbf{M}_{34} = 0$ across each triplet[16]. The optimized quadrupole settings returned by the envelope code were fed into `LORASR`. On the other hand, the longitudinal tune is chosen to cause appreciable second order aberrations in Tank-5, due to the choice of establishing a small z-waist at the exit of the resonator. Given the diverging z-envelope at that tank's injection (Fig. 4.15, $s \approx 480$ cm), this choice requires imparting additional longitudinal restoring forces to the bunch, causing filamentation (Fig. 4.16, bottom right). In the Tank-5 case, the price to pay for such a strong longitudinal

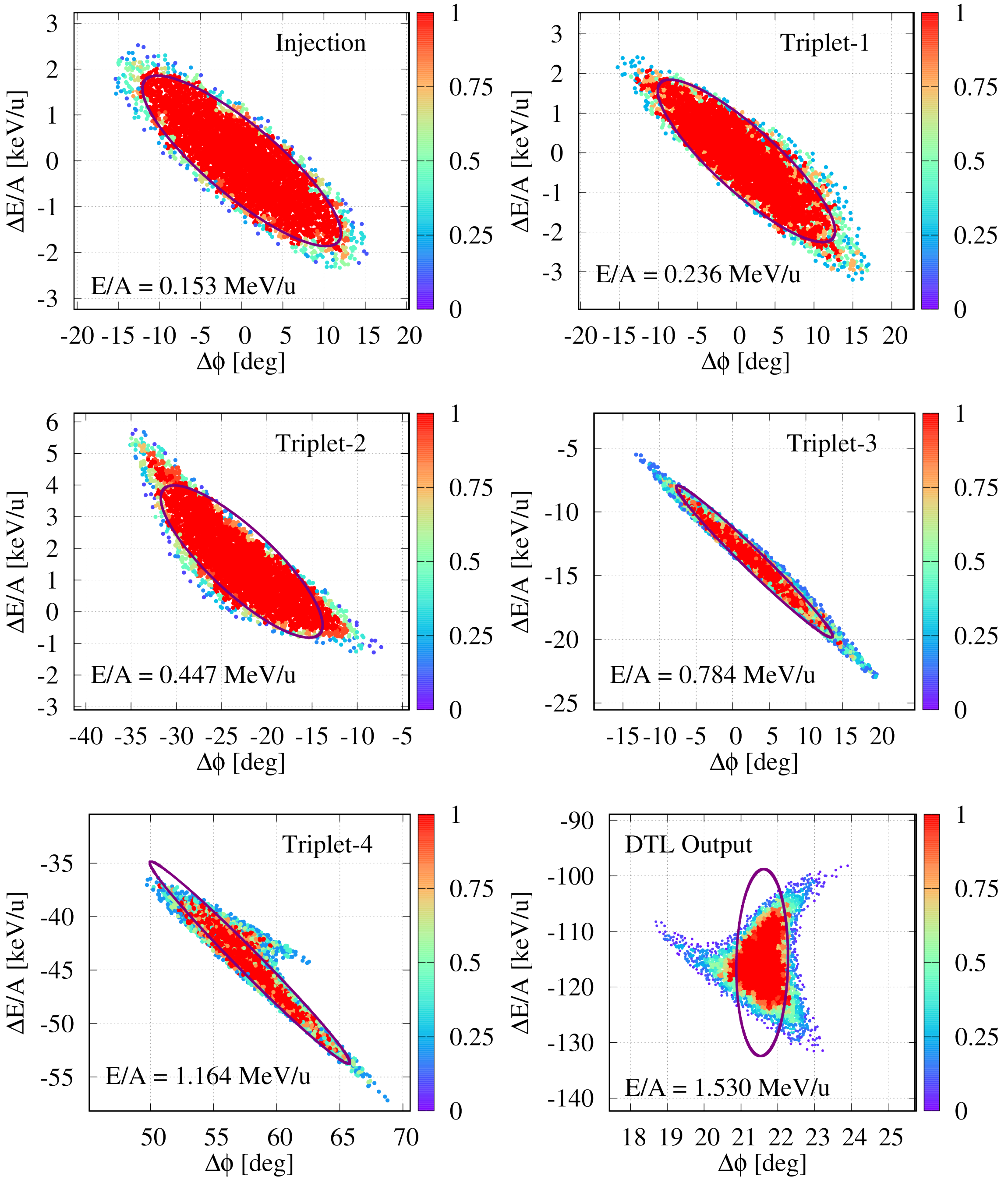

Figure 4.16: Longitudinal phase space distributions about the reference particle: `LORASR` normalized density for 5,000 particles (points) and `TRANSOPTR` 4 rms containment ellipses (purple) at injection and through the ISAC-DTL, for the envelopes shown in Fig. 4.15, with injected beam parameters in Tab. 4.2. Normalized color density scale shown on the right of each plot. As the bunch progresses through the linac, second order components of the accelerating fields cause rf filamentation, which is represented in the multiparticle code. `TRANSOPTR` computes the linear component of the forces, which agrees with the core of the multiparticle beam simulation[16].

Parameter	Units	Value
E_i	[MeV]	2.121
m_0	[GeV/c^2]	13.044
x_i	[cm]	0.100
P_{x_i}/P	[mrad]	5.900
r_{12}		-0.850
y_i	[cm]	0.100
P_{y_i}/P	[mrad]	5.900
r_{34}		-0.850
$\epsilon_{x,y}$	[cm mrad]	0.311
z_i	[cm]	0.170
P_{z_i}/P	[mrad]	6.133
r_{56}		-0.848
ϵ_z	[cm mrad]	0.554

Table 4.2: Input `TRANSOPTR` reference particle parameters and $\boldsymbol{\sigma}$-matrix used for the comparative simulation shown in Figs. 4.15 & 4.16, an ^{14}N^{3+} beam. Emittances are unnormalized[16].

focus is an increase in z-emittance by roughly 40%[16]. Nevertheless, `TRANSOPTR` successfully tracks the core of the (z, P_z) distribution. Additionally, the optimizer can be called to minimize these higher order effects, by constraining transfer matrix element $\mathbf{M}_{65} \approx 0$. It is not exactly zero due to the necessity of a small amount of longitudinal focusing, to prevent bunch divergence.

Each cavity's phase response is compared to `LORASR` in Fig. 4.17, showing the good overall agreement near optimum acceleration at different field scalings. Additionally, ^{16}O^{4+} on-line measurements are shown superimposed to both models. Differences between both codes are attributable to non-flatness of peak electric field values in each gap used for the `TRANSOPTR` model, whereas the `LORASR` model was purposely built with flat fields: This allows for an implicit comparison of the difference in E/A response to phase scanning. Interestingly, the `TRANSOPTR` data (non-flat fields) agrees better with on-line measurements than with the flat field assumption[16]. Additionally, since `LORASR` defines the beam energy in terms of the bunch centre, in regions of high particle losses this together with second order aberrations may act to shift the average energy. The `LORASR` phases were iterated until transmission loss caused the code to abort. This can be seen in the figure for phases negative of optimum acceleration. Since `TRANSOPTR` tracks only a single reference particle which always transmits, no such effect takes place.

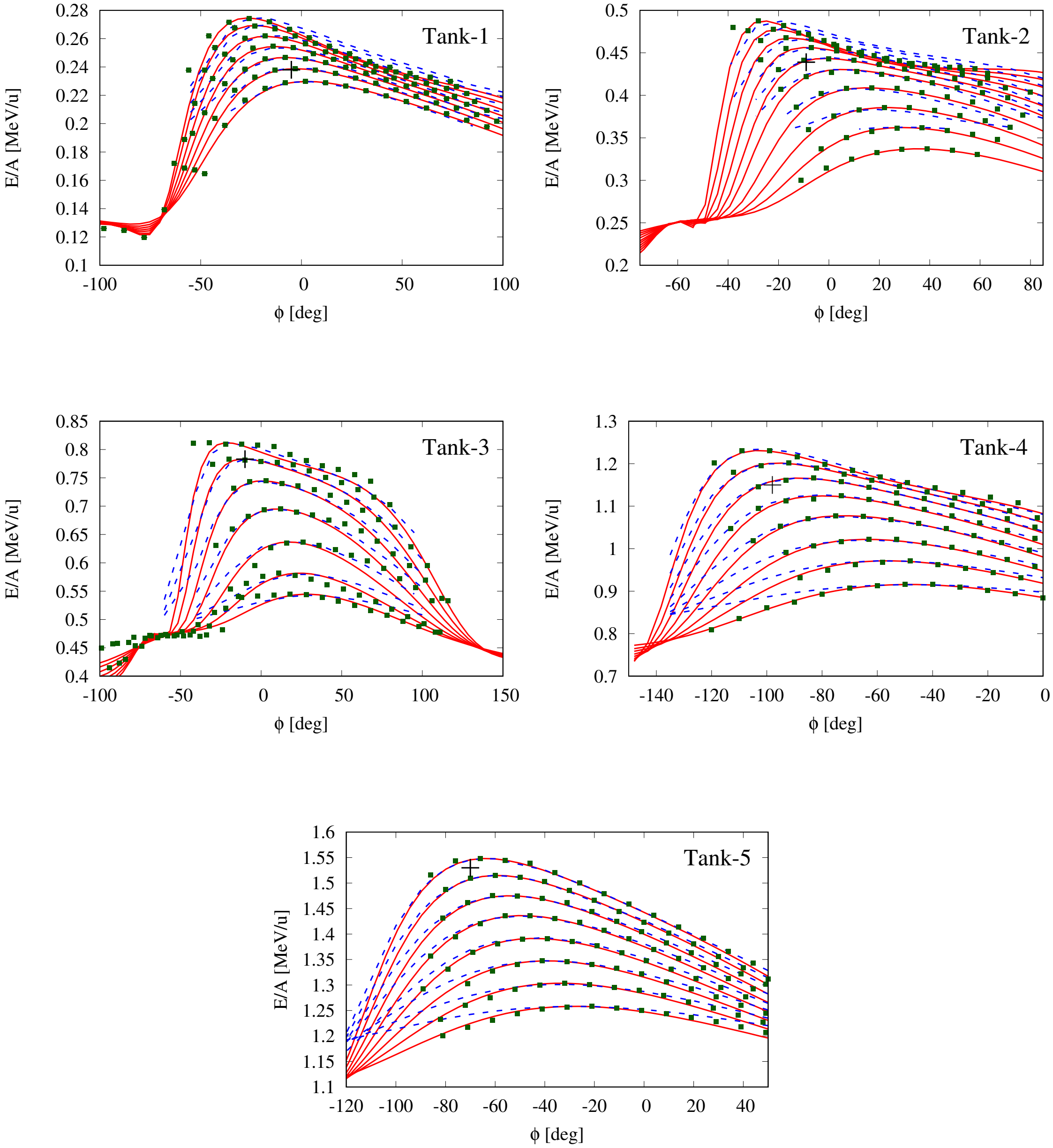

Figure 4.17: Comparison between `TRANSOPTR` (red), `LORASR` multiparticle simulation (blue) and ISAC-DTL on-line (green) reference particle E/A output rf phase response for listed DTL tanks. The operational maximum E/A for each cavity is shown as a black cross on each plot. While `TRANSOPTR` tracks a single reference particle, `LORASR` used a total population of $\mathrm{N} = 2000$ ions. Scans in the latter code were liable to particle transmission loss, which at phases sufficiently far away from the optimum can cause the code to abort. Particle losses in the strongly decelerating E/A regime (phases negative of optimum) also shifted the bunch center definition, causing a slippage when compared to `TRANSOPTR`'s reference particle[16].

Figure 4.18 shows 2 rms envelopes from the OLIS multi-charge ion source of a $^{20}\mathrm{Ne}^{4+}$ beam with $E/A = 2.04\,\mathrm{keV/u}$, transported and matched into the ISAC-RFQ. All tunes computed with `MCATSequencer` (Section 3.10). There are two cases on display: Initially (Fig. 4.18, top), the ISAC-DTL is set for $E/A = 0.803\,\mathrm{MeV/u}$ with Tank-3. The DTL has been retuned to $E/A = 1.53\,\mathrm{MeV/u}$ (Fig. 4.18, bottom), after also re-optimizing injection in the ISAC-RFQ, thereby minimizing the effects of a synchro-betatron oscillation present in the initial state. Additionally, the MEBT tune has been optimized and set from a time-focus on the stripping foil to debunching, minimizing P_z. `TRANSOPTR` now enables fast computation of entire linac tunes from first principles. The envelope method is equally powerful for the analysis of existing machine tunes, as shown with the MEBT section in this chapter. Using the insights gained from this analysis, a new tuning methodology was devised for the ISAC-DTL, which is presented in the next chapter.

More broadly, the developments presented in this chapter are general and not limited to the ISAC linac. The required input parameters for the RFQ and DTL envelope simulation and optimization capabilities presented herein are the typical design parameters of these machines. For the rf quadrupole, a table of (s, a, m, k) values, or alternatively (s, A_{01}, A_{10}, k) is required, while the on-axis longitudinal field intensity $\mathcal{E}(s)$ must be supplied for the axially symmetric DTL case.

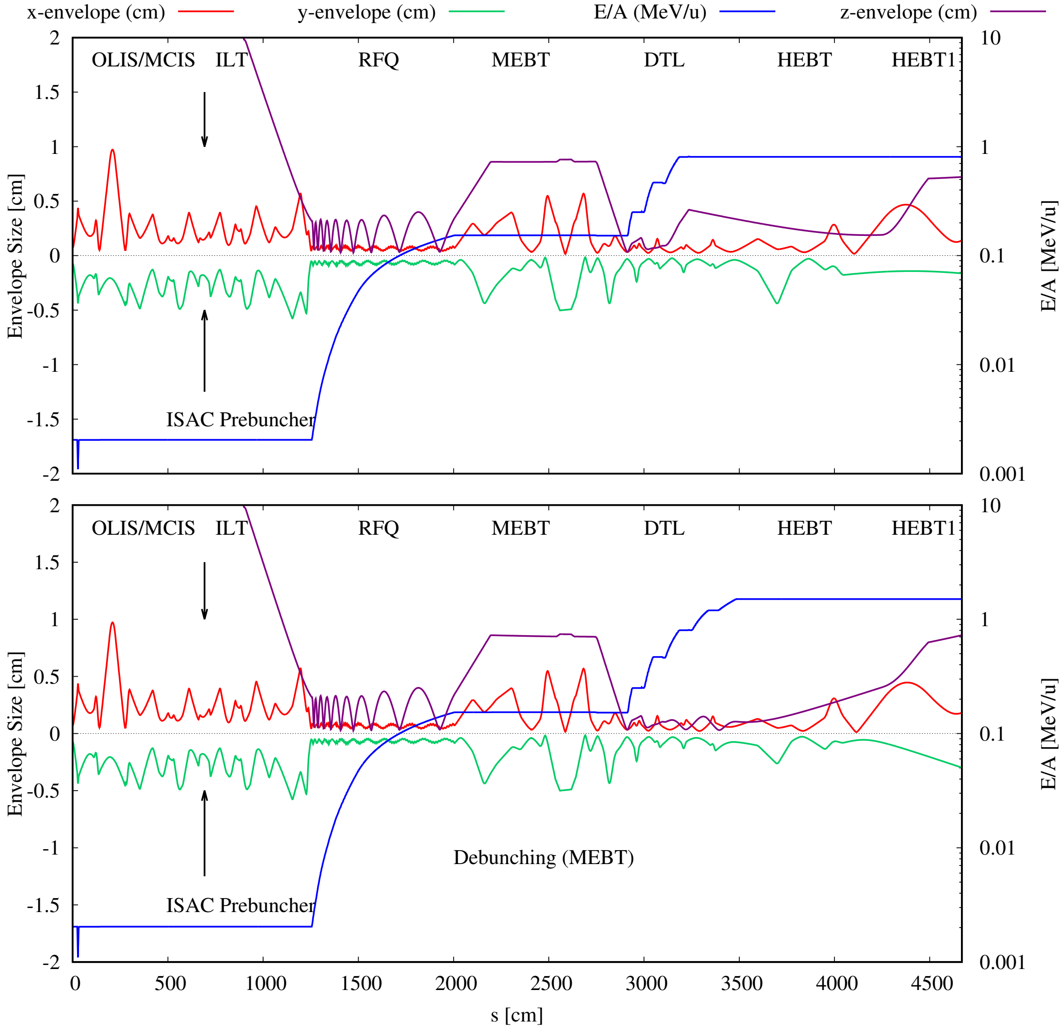

Figure 4.18: Simulations of 2 rms beam containment envelopes through the ISAC-I linac. The reference particle energy is shown in blue for a $^{20}\mathrm{Ne}^{4+}$ beam, extracted from OLIS with $E/A = 2.04\,\mathrm{keV/u}$ and ending at the HEBT1 high energy diagnostic station at maximum DTL operational output $E/A = 1.53\,\mathrm{MeV/u}$. A decelerating Einzel lens[87] is located near $s = 0$, causing a brief drop in E/A. `TRANSOPTR` is executed in 6D bunched mode and the beam matrix initial conditions for the longitudinal dimensions are chosen to mimic the acceptance of the pre-buncher, represented as a single discrete 11 MHz rf kick (arrows), though OLIS beams are continuous[16].

Chapter 5

Model Coupled Accelerator Tuning On-Line

Applying `TRANSOPTR` to compute tunes allows for its use to perform on-line measurements or tuning intervention, this opens a new tuning paradigm, with basic examples shown in this chapter. First, the low energy section and DTL transverse beam envelopes are computed and compared to on-line observations. Next, a beam based rf calibration is established with the DTL, using $^{16}\mathrm{O}^{4+}$. Finally, using `MCATSequencer` (Section 3.10) to perform `TRANSOPTR` optimizations through rf cavities, to find (V_s, ϕ) producing a given desired E/A sidesteps the complexities of analyzing the response of each tank to parameter variations, instead numerically optimizing the total energy of the reference particle through the field.

5.1 OLIS Extraction and RFQ Injection

The low energy section of the accelerator (Fig. 1.5, *OLIS*) is comprised of electrostatics: Quadrupoles, steerers, spherical benders, etc.. The section was designed by Baartman[88], using `TRANSOPTR`. During a 2020 beam development period, a $^{7}\mathrm{Li}^{+}$ beam from the surface ion source at OLIS was injected into the ISAC-RFQ, with the intent of testing the updated `TRANSOPTR` model of that section, in which drawings of the as-built section were used to verify and correct original model dimensions[87].

Using `python` software which interfaces with the `EPICS` control system, real-time optics element setpoints were read and set in a parallel `TRANSOPTR` simulation, enabling extraction of the $\boldsymbol{\sigma}$-matrix at OLIS extraction and RFQ injection:

1. Rotary beam profile monitors (RPMs) throughout the low energy optics were used to measure the transverse intensity distributions.

2. Using the package `profiles`[89], the 2 rms (x, y) sizes were measured from these distributions, producing the sizes of the Li-beam.

3. These were then programatically set in the parallel `TRANSOPTR` simulation as fit constraints upon the beam matrix, at the location of each RPM.

4. Finally, an initial condition optimization using transverse Twiss parameters $(\alpha, \beta, \epsilon)$ for both (x, y) at Frenet-Serret $s = 0\,\text{cm}$, which in the model corresponds to the source extraction, was carried out. The envelopes corresponding to this initial condition fit are shown in Figure 5.1, with measured beamsizes shown as points.

The beam size measurements and the `TRANSOPTR` calculated envelopes correspond extremely well, given the uncertainty of misalignments, steering and OLIS beam quality. Causes of disagreement between envelope and measured sizes are likely attributable to differences in element positions or strength. Development of the OLIS model for this work included a review of the section's technical drawings to verify the optics. As there have been many modifications made to the OLIS beamline over the last 20 years, as-built drawings could not be clearly identified[61]. It was found that the electrostatic quadrupoles IOS:Q2 and IOS:Q5 were both moved by roughly 1" along the optical axis[61, 62], though the remainder of the ILT and IRA line has not been physically inspected. Since the agreement is nevertheless good, one expects these errors to be minimal, though certainly improvable. Doing so would require performing more accurate re-surveying of the as-installed optics to confirm their dimensions and positioning. As a re-design and re-building of the low energy optics is scheduled to occur in the near future, this should enable an updating of the `TRANSOPTR` model and an improvement of its on-line agreement and predictive power.

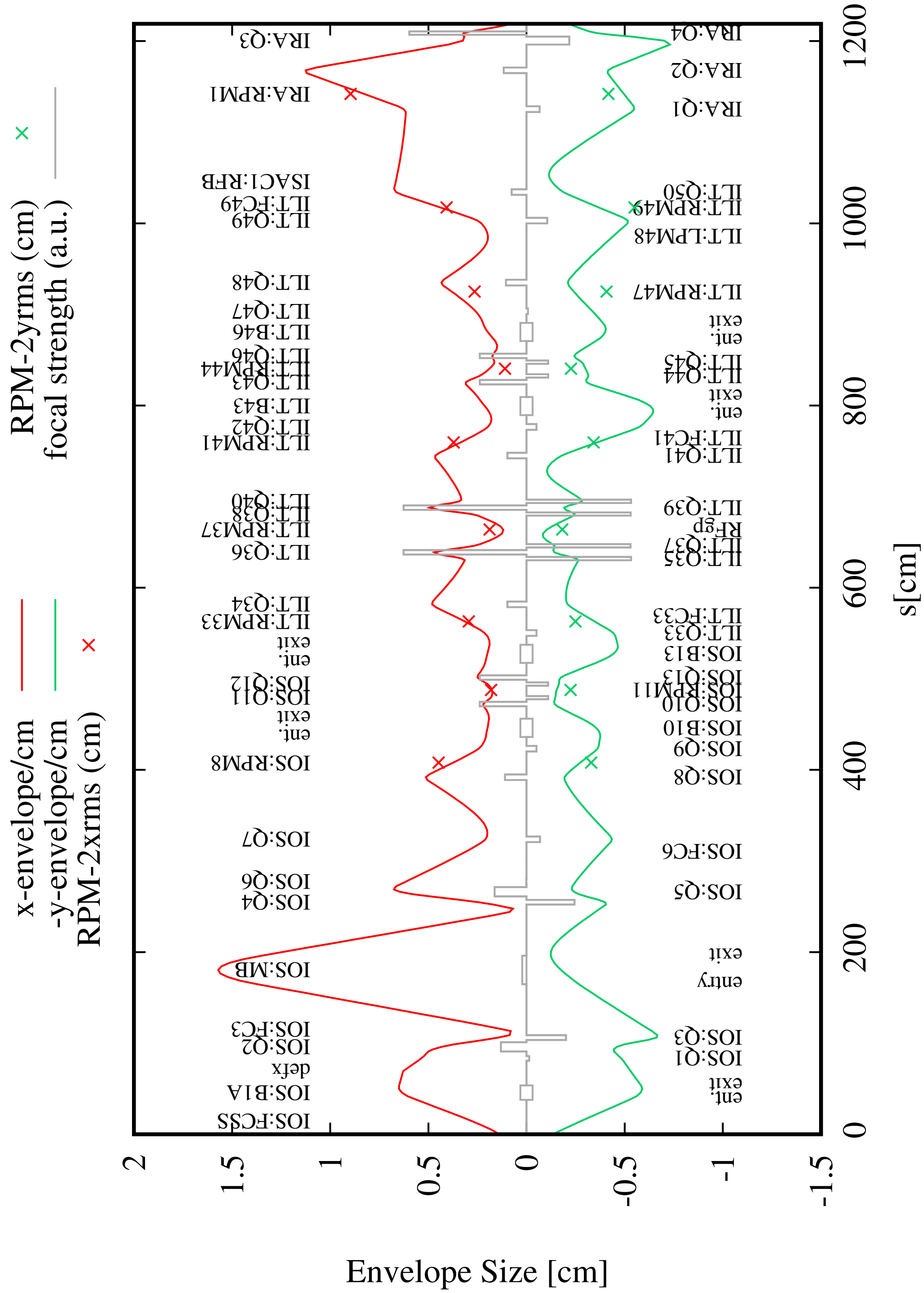

Figure 5.1: Using rotary position monitors (RPMs) in the low energy section, it is possible to perform an initial condition optimization, finding the transverse starting beam matrix elements which reproduce on-line measured beam profiles, given the live setpoints of the optics, using `TRANSOPTR`. In this case, a $^{7}\mathrm{Li}^{+}$ beam at 30 keV was used. On-line tune computed with `MCATSequencer` definition from Fig. 3.12.

Beam containment ellipses for (x, x') and (y, y') are shown in Figure 5.2 at OLIS extraction (Fig. 5.1, bottom) and RFQ injection (Fig. 5.1, top), reconstructed using on-line measured intensity profiles. This constrained beam optics optimization method using the envelope code enables the measurement of containment ellipses generated by OLIS without a dedicated emittance meter. The measurements in Fig. 5.1 and 5.2 can easily be proceduralized for operators, only requiring the measuring of beam profiles along the line. It is important to note that this method will only work if the transmission is very high, as close to 100% as possible. In the case presented herein, measured transmission was 95%. Small transmission losses along the line will also contribute to reconstruction errors, since `TRANSOPTR` has *a priori* no information as to where the beam is lost. The on-line tune simulation software used to produce the above figures is presently in use for the development of on-line tuning software for operators.

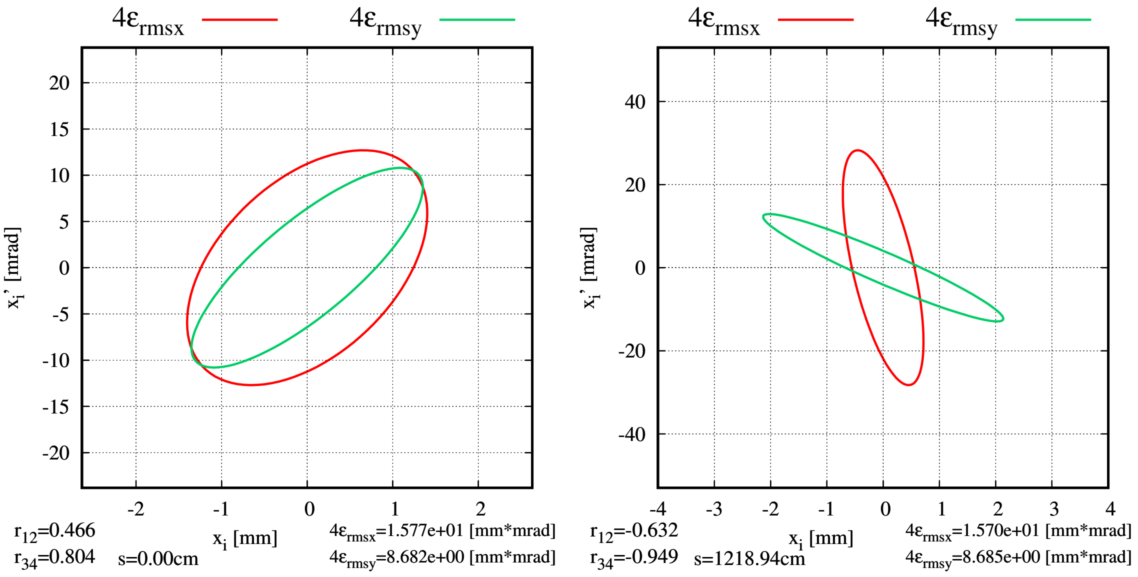

Figure 5.2: Using the measured on-line beam sizes of a ^{7}Li$^+$ beam at 30 keV from OLIS (Fig. 5.1), the starting beam parameters from the surface source were reconstructed using the envelope model, showing 4ϵ rms containment ellipses (left) and the injected ISAC-RFQ distribution (right). The reconstruction provides an initial emittance estimation for both transverse dimensions.

5.2 DTL Drifting Tune On-Line

The understanding that the MEBT design tune is expected to be quite sensitive to small quadrupole tip-field errors (Section 4.2.3) resolves the longstanding observation that the DTL quadrupoles, when set to model values, did not produce acceptable transmission. Modelling and analysis with `TRANSOPTR` allows for the definition of the root cause of this error, which is threefold:

- The operational tune used to scale original DTL quadrupole current setpoints from `LANA` simulations accidentally inverted the B-I relationship for the inner ($L_{eff} = 8.7\,\mathrm{cm}$) and outer ($L_{eff} = 5.8\,\mathrm{cm}$) triplet quadrupoles for the DTL[63].
- The above scaling also inverted the polarities of all DTL quadrupoles[90].
- Operational tuning methodology has, to date, set the MEBT section quadrupole currents to model computed values and procedures prevent their manual tuning[91]. This causes a transverse injection mismatch at the DTL (Section 4.2.3).

These factors explain why it has been observed that setting model computed values produced low transmission through the drift tube structure over the life of the machine. Understanding that the MEBT tunes causes a mismatch at Tank-1 injection, it is possible to diagnose the longstanding necessity of manual DTL quadrupole tuning at ISAC as the operationalization of a transverse mismatch correction through manipulation of the DTL optics. By inverting the tuning approach of the MEBT-DTL-HEBT segment, it is possible to achieve high transmission through the DTL and produce beam profiles in the HEBT section consistent with the according model. This was first achieved using a $^4\mathrm{He}^+$ beam, injected at 0.151 MeV/u from the MEBT section into the DTL, with its rf unpowered. The MEBT quadrupoles Q6 to Q13 were manually adjusted after having computed a transverse tune for the DTL and HEBT quadrupoles using `MCATSequencer`[16, 90]. Results are presented in Figure 5.3, showing the computed tune as dotted lines, measured beam profile sizes along the machine, and the best-fit envelopes through these recorded datapoints as solid lines. Table 5.1 lists beam parameters associated with this tune. In order to extract the sizes inside the DTL lattice itself, linear position monitors (LPMs) were used (Fig. 5.3, $s < 500\,\mathrm{cm}$), while a rotary position monitor (RPM) was used in HEBT, downstream of the linac (same figure, $s \approx 950\,\mathrm{cm}$).

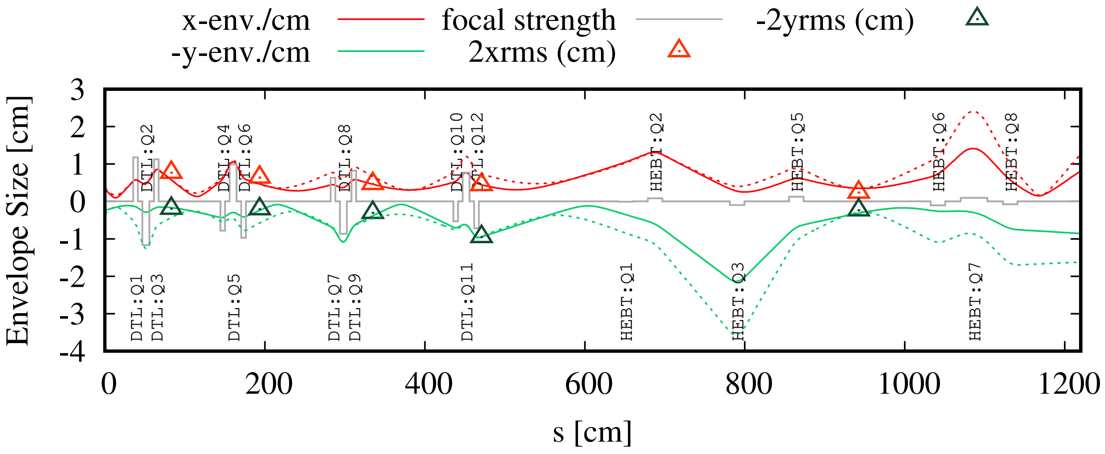

Figure 5.3: Computed 2rms envelopes for a ^{4}He$^+$ beam at $E/A = 0.151\,$MeV/u (dotted lines). Measured beam sizes are shown as triangular dots along the plot. The LPM traces ($s < 500\,$cm) cannot be processed on-line and were post-processed, while the HEBT:RPM5 sizes ($s \approx 950\,$cm) were extracted using `profiles`[89]. Using measured beamsizes, the actual on-line beam parameters were extracted (solid lines), with the fit parameters listed in Table 5.1. Despite the mismatch into the tune, a transmission of 98% was recorded through the DTL.

Parameter	Unit	Model-Tune	Post-Processed
E_i/A	[MeV/u]	0.151	0.151
m_0	[GeV/c^2]	3.726	3.726
x_i	[cm]	0.360	0.334
P_{x_i}/P	[mrad]	23.600	24.157
r_{12}		-0.800	-0.959
ϵ_x	[mm mrad]	38.784	22.780
y_i	[cm]	0.340	0.241
P_{y_i}/P	[mrad]	22.500	7.500
r_{34}		-0.000	-0.889
ϵ_y	[mm mrad]	26.563	8.293

Table 5.1: Parameters used for a ^{4}He$^+$ beam tuned through the ISAC-DTL at $E/A = 0.151\,$MeV/u, with all of the DTL rf unpowered. Post-processing intensity traces from the linear position monitors, together with the measured HEBT:RPM5 sizes, it was possible to extract the injected parameters into Tank-1.

While the package `profiles`[89] was used for the RPM size extraction, as of yet there exists no programmatic method of extracting the size online from the LPM readings. Consequently, the LPM sizes had to be post-processed after the measurements were taken on-line. Since the LPMs consist of a movable slit which is scanned in front of a Faraday cup, the measurement process is longer than for RPMs, rendering their use more involved. An improvement for DTL tuning at ISAC would be:

- (**Short-term**) Writing of software to extract the centroids and rms beam sizes from the LPM detectors automatically at ISAC, or
- (**Long-term**) Replacement of LPMs with newer, faster transverse diagnostics, that can be used during rf operation.

The short-term solution would allow the processing of LPM traces, though the devices cannot be used when DTL rf is enabled, limiting its applicability. Measurement during rf operation would require new devices. Though the recorded transmission for the ^{4}He$^+$ tune shown in Figure 5.3 was 98%[92], the match into Tank-1 is not perfect. Inspection of Table 5.1 shows the emittances for both transverse dimensions disagree with the model tune parameters that were used. Unfortunately, extraction of these parameters is difficult without use of the LPMs.

Performing quadrupole scans[76] at HEBT is error prone at this E/A, since the quadrupoles, of similar effective lengths and apertures as the MEBT quadrupoles, also operate at low gradient, whereas the shorter DTL quadrupoles require higher gradients for a similar focal strength. While the injected distribution could be extracted with a HEBT quadrupole scan using RPM5, in practice this was found to result in tunes with low transmission. Manually de-tuning the MEBT optics to achieve a match into a model-computed DTL tune has been repeatedly performed and results in high transmission, at or above 90%. Future diagnostic improvements as discussed in this section should allow for the on-line evaluation of the injected distribution's emittance and Twiss parameters, in turn enabling use of the `MCATSequencer` (Section 3.10) to re-compute the DTL optics on-line once beam from the MEBT has been manually matched, to re-establish the transverse tune (Fig. 5.3, dashed x, y envelopes) through the DTL.

5.3 Beam-Based Calibration of DTL Fields

The characteristic energy-phase response for IH tanks[15] was exploited to establish calibrations between the control system field scaling parameter V_E and the on-axis field scaling factor V_s, for each DTL cavity. Due to the nature of the rf amplifiers, some responses are quadratic, controlling power ($P \propto V^2$) and others are linear, controlling voltage:

$$V_E = k_1 V_s + k_0, \tag{5.1}$$

$$V_E = k_2 V_s^2 + k_1 V_s + k_0. \tag{5.2}$$

Comparison of the `TRANSOPTR/Opera2D` energy-phase relation to on-line beam based measurements allows for the computation of the fit parameters in Eqs. (5.1) and (5.2). A $^{16}\mathrm{O}^{4+}$ beam was manually tuned through the machine, up to the HEBT1 diagnostic station, consisting of an air cooled, 90° dipole magnet with a radius of curvature ρ = 1.537 m and can deflect a beam with rigidity up to (Bρ) = 1.1 T·m[93] (Figure 5.4) is used for energy measurements. A position-energy diagnostic consisting of vertically oriented parallel wires separated by 0.8mm is used to measure beam energy and energy spread. Dispersion caused by the dipole turns a spread in bunch P_z into a horizontal position spread Δx. The energy resolution of adjacent harp wires is $\Delta E/E \sim 0.1\%$[94]. This method has a recorded energy error of roughly 1%[95, 96].

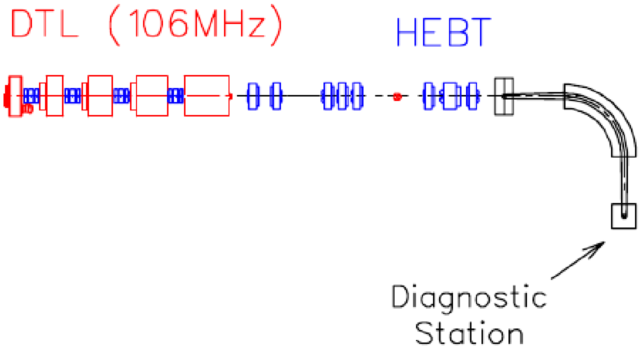

Figure 5.4: The DTL and HEBT1 high energy station, featuring the 90° HEBT1 dipole, also known as the Prague magnet. The parallel wire detector is located at the position labeled Diagnostic Station on the image.

Each cavity was powered on at low amplitude, then several beam energy readings were taken while keeping the control system voltage V_E constant but varying the cavity phase parameter. Once a phase sweep was completed, the cavity voltage was incremented by a fixed amount and the data collection repeated. This produced for each cavity a set of characteristic energy-phase curves at constant cavity voltage. The calibration between the `TRANSOPTR` parameter V_s and the control system V_E was then achieved by iteratively running the code to find the lowest possible field scaling which matches the maximum energy of each on-line phase scan[97]. The linear or quadratic fit parameters with computed linear regression errors are listed in Tab. 5.2 and allow the `TRANSOPTR`-DTL model to directly read-in the control system rf amplitude and obtain the correct physical scaling of the on-axis field within the cavity. Graphs of each fit are shown in Figures 5.5 and 5.6, including displaying the raw fit calibrations obtained between V_E and V_s.

IH-Tank	a [V]	m [V]	b [V]
Tank-1	7±1	-(2±1)×10^3	(2.6±0.4)×10^6
Buncher-1	–	(7.99±0.07)×10^3	(3.06±0.05)×10^6
Tank-2	–	(6.83±0.08)×10^3	-(3.66±0.05)×10^6
Buncher-2	-1.6±0.1	(9.0±0.2)×10^3	-(7.2±0.1)×10^6
Tank-3	–	(7.01±0.04)×10^3	-(4.69±0.03)×10^6
Buncher-3	–	(6.50±0.08)×10^3	(1.51±0.08)×10^6
Tank-4	–	(4.85±0.06)×10^3	-(1.70±0.05)×10^6
Tank-5	–	(4.14±0.06)×10^3	-(1.33±0.05)×10^6

Table 5.2: `TRANSOPTR` calibration fits for each cavity in the ISAC-DTL, using either a linear ($y = mx+b$) or quadratic ($y = ax^2+mx+b$) fit function[97]. An $^{16}O^{4+}$ beam at $E/A = 0.153$ MeV/u was injected into the DTL from the RFQ for this measurement. Fit residual errors are shown as uncertainties for each parameter.

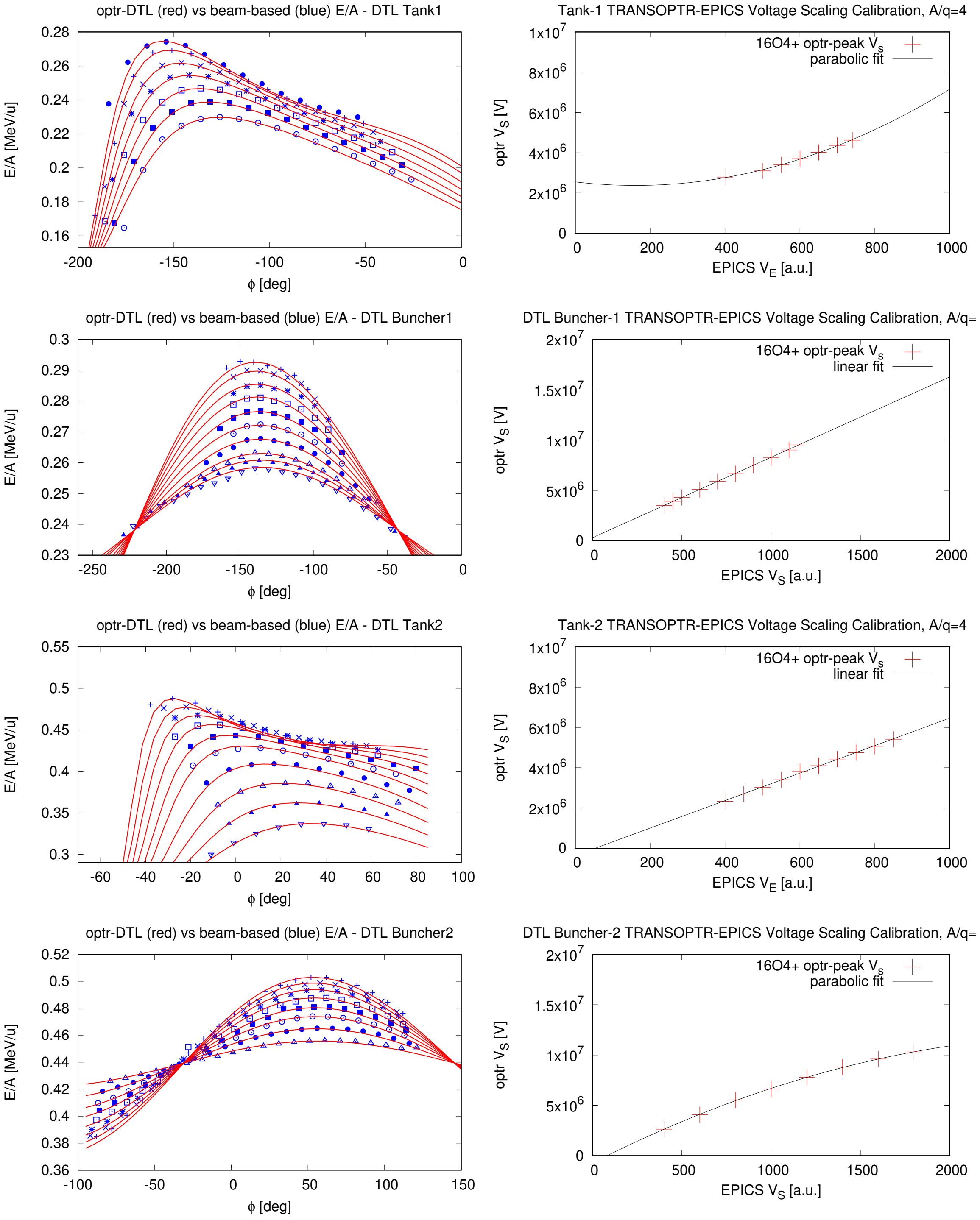

Figure 5.5: Beam-based calibration[97] of the `TRANSOPTR`-DTL cavity electric fields, using $^{16}O^{4+}$. The energy-phase response at constant field scaling is shown on the left, while the rf amplitude calibration is shown on the right[15, 16].

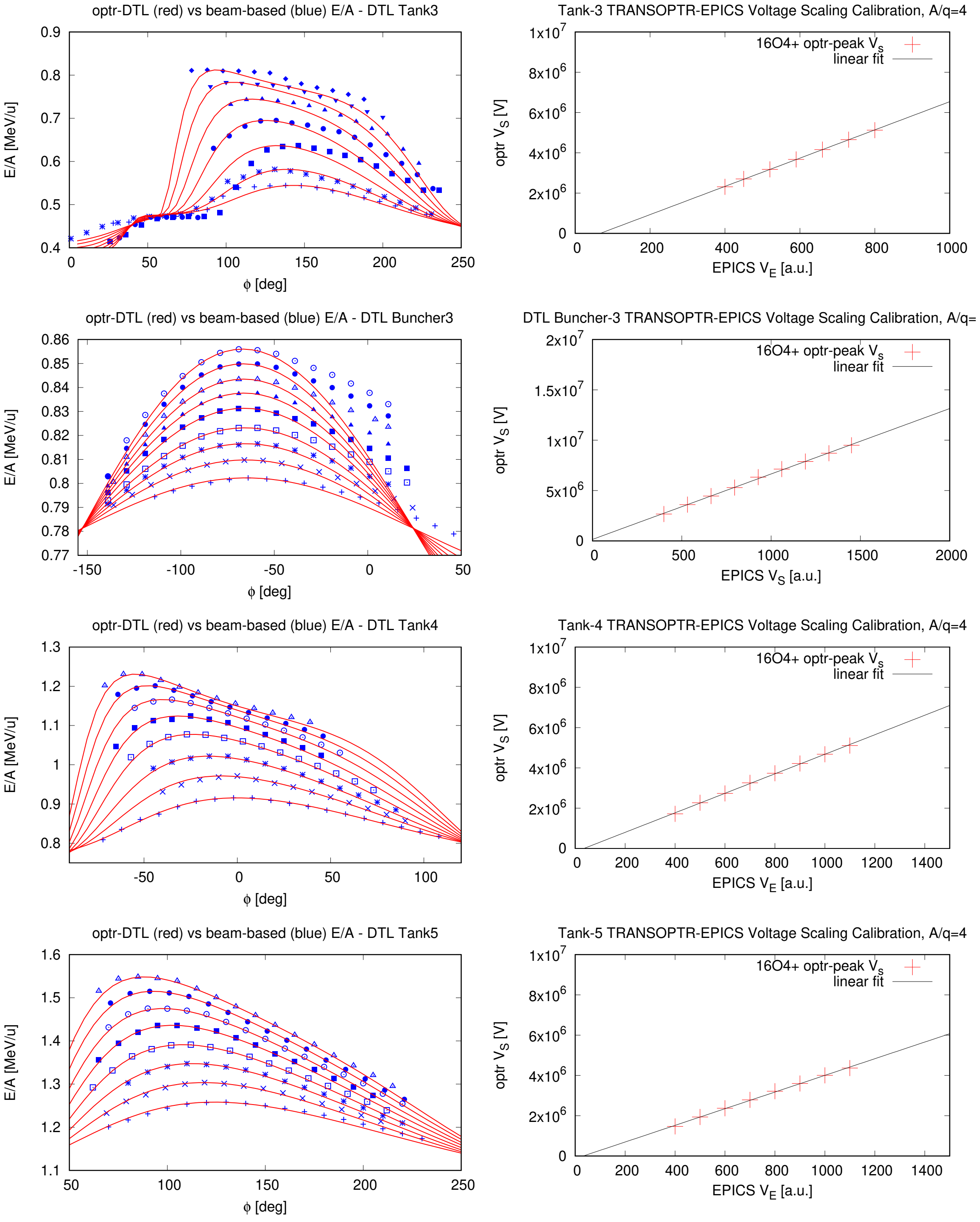

Figure 5.6: Beam-based calibration[97] of the `TRANSOPTR`-DTL cavity electric fields, using $^{16}\mathrm{O}^{4+}$. The energy-phase response at constant field scaling is shown on the left, while the rf amplitude calibration is shown on the right[15, 16].

Until now, the lack of an on-line energy setting capability has caused the operational energy change procedure to require manual ramping of V_s, while periodically optimizing ϕ for maximum energy gain. This had to be performed while also periodically re-tuning the quadrupoles to the new beam energy to maintain transmission and observable beam and also ramping the high energy dipole magnet downstream of the linac, used to monitor the beam energy. This causes tuning to be inefficient and does not guarantee proper optimization of all parameters. The presented calibration allows `TRANSOPTR`'s optimizers to compute DTL IH cavity voltage settings for any desired output energy, in control system field scaling units. The calibration from Table 5.2 additionally enables the on-line determination of the DTL energy, by running a `TRANSOPTR` simulation using the real-time rf amplitude values, while calling the optimizer to find the cavity phases which minimize bunch P_z, while also constraining the bunchers be operated 45° off peak-acceleration. This is a new method to monitor the configured reference energy profile through the accelerator.

5.3.1 ISAC-DTL Buncher Operation

A feature is visible on the Buncher-3 dataset (Fig. 5.6, second from top), in which recorded E/A seem to disagree with `TRANSOPTR`'s predictions at phases higher than -50°. The recorded buncher data is attributable to a choice that was made during measurements: The Buncher-3 E/A output spectrum was observed to produce two separate peaks on the high energy diagnostic station[15], and it was chosen to record the E/A of the high energy end of the distribution in such cases, recorded in the figure. The emergence of high energy tails suggests the nonlinear evolution of the (z, P_z) distribution in Buncher-3, implying it is being operated in a regime beyond its expected linear response. To verify this, blueprints of the bunchers were used to measure the distance from first to second gap center in each ISAC-DTL buncher. This distance, also referred to as the cell length is defined as[27]:

$$L = \frac{\beta_s \lambda}{2}, \tag{5.3}$$

with λ the cavity rf wavelength and β_s the synchronous particle velocity in the cell. Using both the mid-gap to mid-gap distance and the DTL rf parameters, the design β_s in the first cells of each DTL Buncher are listed in Table 5.3. Observe the signifi-

Buncher	Operational E_i/A [MeV/u]	Operational β_s [%]	Design β_s [%]
1	0.238	2.26	2.31
2	0.439	3.07	2.72
3	0.781	4.09	3.33

Table 5.3: Comparison of operational injection E_i/A and reference synchronous velocity β_s for each ISAC-DTL Buncher, compared with the design synchronous velocity of the first cell (distance from first to second midgap) for each.

cant difference between β_s for Bunchers 2 and 3, which are operated at synchronous velocities 13% and 23% higher than their design assumption[10]. The observed discrepancies between `TRANSOPTR` and on-line measurements for Buncher-3 illustrate the breakdown of the first order reference particle treatment. Table 5.3 suggests the deviation from the synchronous profile is most significant in Buncher-3 and Figures 5.5 and 5.6 suggest these issues are unique to that device. The triple-gap cavity synchronous velocity correspond to operation of the upstream IH tank at below design output E/A[98]; they are intended to provide bunching for such a case. Per Figs. 5.5 and 5.6, Tanks-2 and 3 are easily capable of compensating the minor energy gain caused by the triple-gap cavities. Thus, bunchers 2 & 3 can remain unpowered for full acceleration, avoiding operation beyond their design synchronous velocity. This is both supported by simulations (Figure 5.7), and previous operational experience: There are in fact several cases where bunchers 2 and 3 have been left unpowered due to rf issues, with no significant change in DTL transmission or final energy spread[92].

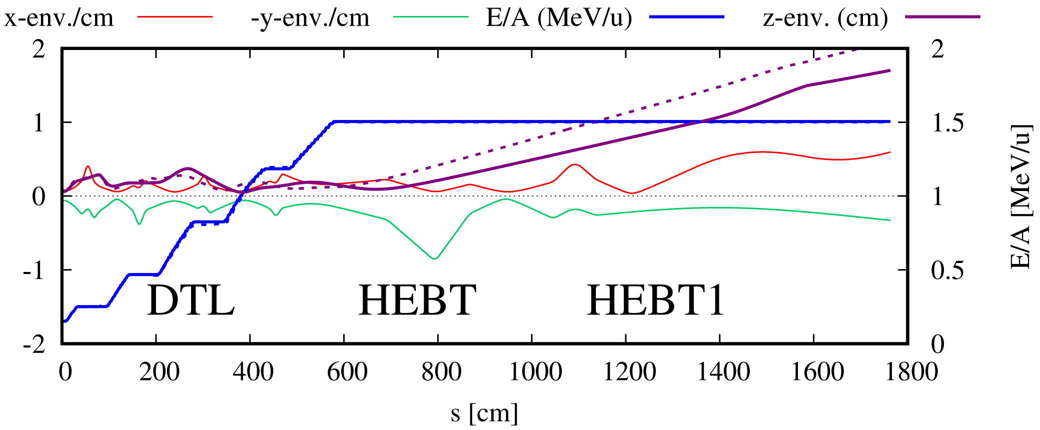

Figure 5.7: `TRANSOPTR` computed ISAC-DTL envelopes showing a tune for $E/A = 1.53$ MeV/u with (dotted lines) and without (solid lines) operation of bunchers 2 and 3. Transverse settings computed with `MCATSequencer`.

5.3.2 Model Based Energy Optimizations

An optimization is performed to find the (V_s, ϕ) values which correspond to the real-time setting of the tank, to find the final E/A in the model, by constraining: $\mathbf{M_{21}} + \mathbf{M_{43}} + \mathbf{M_{65}} \approx 0$[16], shown in Figure 5.8. This criterion minimizes the total accumulated effects of the functions $\mathcal{A}(s)$ and $\mathcal{B}(s)$ (Eqs. (3.63) & (3.64), respectively) in the transfer matrix for the accelerating structure. This both minimizes the transverse rf focal effects of tank transit while also avoiding excessive bunch z-growth by providing a small amount of longitudinal bunching and minimizing second order aberrations on the distribution.

```
      SUBROUTINE TSYSTEM
      COMMON/SCPARM/QSC,ISC,CMPS
      COMMON/MOM/P,BRHO,pMASS,ENERGK,GSQ,ENERGKi,charge,current
      COMMON/PRINT/IPRINT
      COMMON/SS/SX(13,6)
      COMMON/BLOC1/RFA1,RFP1

      CMPS=0.0765 ! Number of cm per step, for plotting only
      wo=1.0 ! Weight aberration from optical elements

      call marker('DTL:FC0')
      ! RF cavity/linac: ISAC1:DTL1
      call linacn(100,1001,6.79376e-06*RFA1**2.0 - 0.00219132*RFA1 +
     &2.55377,32.746,1.0608e+08,1.0*RFP1,'ISAC1:DTL1')
      call fit(2,6,5,0.0,1.,1)
      call fit(2,2,1,0.0,1.,1)
      call fit(2,4,3,0.0,1.,1)
      call print_transfer_matrix
      return
      end
```

Figure 5.8: `TRANSOPTR` `sy.f` file spanning Tank-1, calling subroutine `linac`[13], with fit constraints to find the real-time cavity output energy using the calibration from Fig. 5.5. The control system amplitude `RFA1` is converted to a physical scaling of the on-axis field in MV/cm. Fit constraints are placed on the beam matrix element $\mathbf{M_{65}} = 0$[16], which minimizes longitudinal restoring forces through the cavity. Constraints are also specified for $\mathbf{M_{21}} = \mathbf{M_{43}} = 0$, minimizing rf defocusing. This allows for the prediction of the real-time E/A in the machine.

The optimization method shown in Figure 5.8 is presently being integrated into the tuning procedure for operators at TRIUMF. Additionally, the model can perform noninvasive energy measurements, with Figure 5.9 showing the predicted E/A values for a ^{36}Ar^{7+} beam[97], performed offline. Generic starting beam parameters were used for the longitudinal $\boldsymbol{\sigma}$-matrix, listed in Table 5.4. The measured E/A errors are shown to the left of the figure, and are at or below the 1% uncertainty level for the HEBT1 dipole magnet. Additionally, this DTL configuration does not make use of Buncher-2 for this particular $E/A = 1.50\,\mathrm{MeV/u}$ tune, as discussed in Section 5.3.1. Future maximum acceleration DTL tunes can avoid operation of bunchers 2 and 3, which will reduce power consumption and avoid unnecessary rf equipment operation.

Parameter	Unit	Value
E_i	[MeV]	2.754
m_0	[GeV/c^2]	16.766
q	[e]	7
z_i	[cm]	0.153
P_{z_i}/P_0	[mrad]	4.0
r_{56}		0.139

Table 5.4: Input `TRANSOPTR` reference particle parameters and $\boldsymbol{\sigma}$-matrix used for the Tank-5 energy change computation on-line, shown in Figure 5.9.

Using an additional fit constraint, the reference particle kinetic energy variable `energk` in Figure 5.8 can be optimized for a user specified output energy, allowing for the definition of a predictive energy change optimization which can be carried out in the envelope code. This enables the computation of the final required amplitude of the IH structure, which thanks to the calibration in Section 5.3, enables the direct setting of DTL rf amplitudes necessary for a given final output energy. This is shown in Figure 5.10, where the same ^{36}Ar7+ beam data has been used to demonstrate the computation. The output Tank-4 beam E/A is used as the initial condition for the optimization, and the model computed a final Tank-5 setting which produces $E/A = 1.498\,\mathrm{MeV/u}$, a -0.1% error.

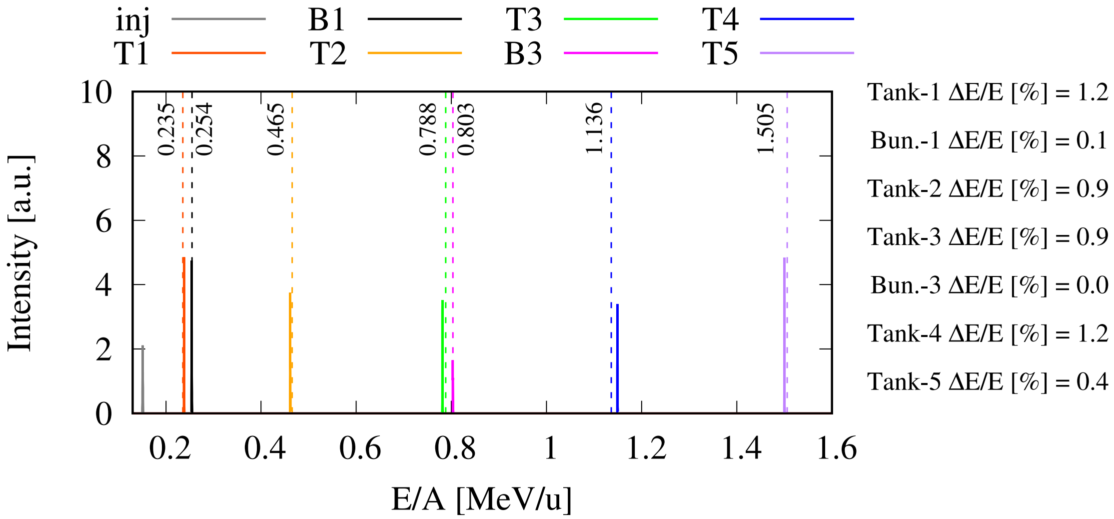

Figure 5.9: `TRANSOPTR` computed DTL longitudinal energy configuration (vertical dotted lines), compared to beam energy measurements performed at HEBT1, for $^{36}\mathrm{Ar}^{7+}$. Tanks (T) and bunchers (B) are indicated in the legend, with the MEBT injection (inj) $E/A = 0.151\,\mathrm{MeV/u}$. The calibrated DTL amplitudes are used. Model computed reference particle E/A values indicated on the graph. Buncher-2 is unpowered in this case. Errors between model and on-line measurements shown to the right.

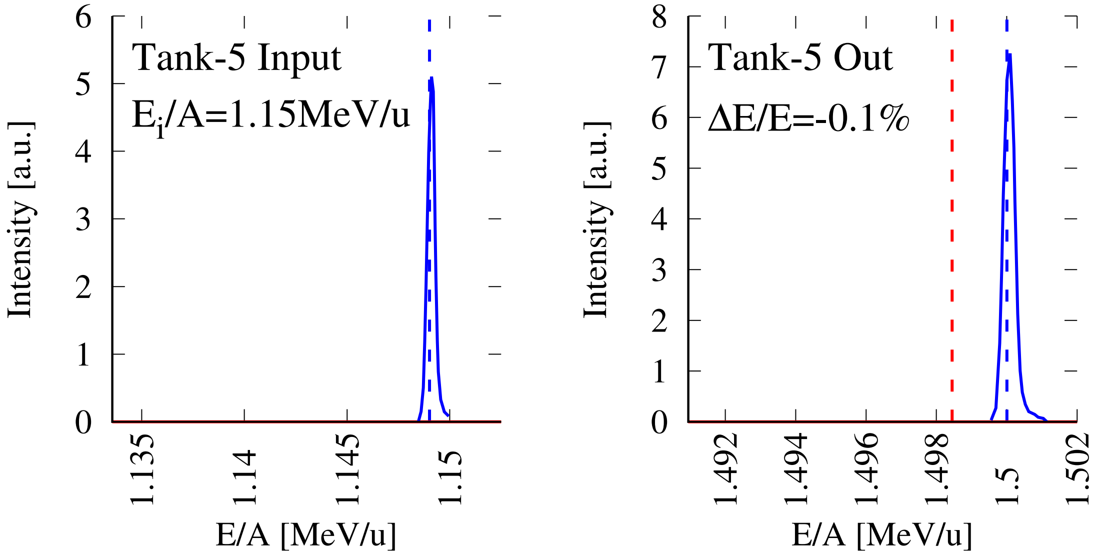

Figure 5.10: `TRANSOPTR`'s simulated annealing optimizer can compute the predicted rf settings and output E/A (red dotted line) for a $^{36}\mathrm{Ar}^{7+}$ beam compared to on-line data (blue dotted line) acquired at the ISAC HEBT high energy diagnostic station.

Chapter 6

Summary & Conclusion

Deepening knowledge in nuclear physics is driven by increasingly high precision experiments, requiring unprecedented beam parameters. This causes the need for more sophisticated and complex accelerators to drive this science. Heavily subscribed delivery schedules at TRIUMF's Isotope Separator and Accelerator (ISAC) means the complex task of frequently tuning the apparatus while maintaining high beam quality, requiring a modern tuning approach based on detailed modelling using computer simulations and machine learning techniques. The development of a full optimizable end-to-end beam envelope simulation of the ISAC linac, capable of real-time output, based on diagnostic feedback input, is a novel implementation of the envelope method.

Since the 1950s, beam matrix methods have been constrained to elements with time-independent Hamiltonians such as drifts, dipoles and quadrupoles. Recent work at TRIUMF has extended this to devices whose focal effects are not in closed form, for instance time-varying accelerating fields[47]. This dissertation has shown the first application of the infinitesimal transfer matrix method to RFQ[14] and DTL[16] type accelerators. For the RFQ implementation, the two first terms of the Kapchinsky-Teplyakov potential for the modulated quadrupole's potential has been used to expand the Hamiltonian for a relativistic charged particle to second order in the coordinates, enabling the treatment of accelerated envelopes through such linacs in `TRANSOPTR`.

These developments have been used to develop model coupled accelerator tuning software, the stated goal of this dissertation and is based upon the works of Lapostolle, Sacherer, Brown, Dahl[99], and many others. This ongoing research aims to exploit such simulations to control accelerators. Previous computation of RFQ or DTL beam envelopes required averaging over multiparticle simulation outputs, both more computationally taxing and rendering manipulations to the beam or transfer matrix less straightforward. Instead, the method discussed herein uses a quadraticized Hamiltonian about a Frenet-Serret reference particle frame, while also tracking energy and time, producing the linear optics. This naturally returns the transfer matrix at each integration step, rendering the computation of constrained optimization upon $\mathbf{M}$ or $\boldsymbol{\sigma}$ straightforward. The computation of tunes using multiparticle simulations for such structures has been a more involved and time consuming endeavour. The key element of this development is that `TRANSOPTR`'s optimizers can be used to effectively produce tunes for identically developed multiparticle models, yielding a tool to assist the designer.

Analysis of the ISAC-MEBT optics revealed a transverse mismatch into the DTL. Transformations of the beam matrix in the section, including a 45° transverse frame rotation, a chromatic 90° bend, low quadrupole settings and the need for a precise longitudinal tune produce a sensitive response of the x-envelope to small errors in the quadrupole tip-fields. This has led to ongoing work to better survey and characterize the devices in the high energy sections[100], improving the accuracy of their field settings. A novel tuning technique for the MEBT-DTL sections has been shown, based on the analysis in this research project. This presents the advantage of confining manual quadrupole tuning to MEBT, which remains unchanging regardless of DTL E/A configuration, enabling the use of model-computed optics for the separated function linac. A future redesign will render the 90° corner doubly achromatic, mitigating observed diurnal transmission variations across the DTL. Planned improvements and replacement of the rf amplifiers will also aid in mitigating these effects.

The simulation of energy gain through the DTL has been used to perform a calibration between the model parameters and the control system rf amplitude variables. This enables the simulation of the real-time state of the machine, since the control system amplitude can be translated into a physical scaling of the normalized electric field distribution $\mathcal{E}(s)$ used in software. This has led to a new method for predictive DTL energy computations: Transfer matrix optimization through the IH structure allows for the optimization of the output beam energy, a novel capability. The envelope code can be used to optimize rf phase and amplitude, aiming for the desired final E/A while minimizing elements of the transfer matrix through the cavity. This has allowed for the exploration of model coupled accelerator tuning techniques at the ISAC linac, using `TRANSOPTR` to compute the machine optics, enabling the reduction of tuning complexity and overhead time. The methodology presented is being developed into a series of accelerator tuning applications at TRIUMF.

The code is now suited for the development of machine learning methods using the end-to-end model elaborated herein[101]. Work has been initiated at TRIUMF in collaboration with RWTH Aachen University and Forschungszentrum Jülich, which has explored the use of the low energy section of the envelope model for reinforcement learning software which aims to produce corrective steering based on diagnostic inputs. This opens the road to the use of the MCAT approach, in which the model optics can be computed from first principles, augmented with ML based techniques to produce an automated tuning capability that operators may one day wield, reducing the overall complexity of machine tuning.

Bibliography

[1] Fred Gilman. The November revolution. *Slac Beam Line*, pages 3–5, 1985.

[2] J Reginald Richardson, EW Blackmore, G Dutto, CJ Kost, GH Mackenzie, and MK Craddock. Production of simultaneous, variable energy beams from the TRIUMF cyclotron. *IEEE Transactions on Nuclear Science*, 22(3):1402–1407, 1975.

[3] JJ Burgerjon, OK Fredriksson, AJ Otter, WA Grundman, and BC Stonehill. Construction details of the TRIUMF H- cyclotron. *IEEE Transactions on Nuclear Science*, 20(3):243–247, 1973.

[4] M Stanley Livingston. The history of the cyclotron. In *Seventh International Conference on Cyclotrons and their Applications*, pages 635–638. Springer, 1975.

[5] A Gottberg. Target materials for exotic ISOL beams. *Nuclear Instruments and Methods in Physics Research Section B: Beam Interactions with Materials and Atoms*, 376:8–15, 2016.

[6] Bricault PG, Dombsky M, Schmor PW, and Stanford G. Radioactive ion beams facility at TRIUMF. *Nuclear Instruments and Methods in Physics Research Section B*, 126:231–235, 1997.

[7] Peter Kunz, Corina Andreoiu, Pierre Bricault, Marik Dombsky, Jens Lassen, Andrea Teigelhöfer, Henning Heggen, and Fiona Wong. Nuclear and in-source laser spectroscopy with the ISAC yield station. *Review of Scientific Instruments*, 85(5):053305, 2014.

[8] P Bricault, M Dombsky, A Dowling, and M Lane. High power target developments at isac. *Nuclear Instruments and Methods in Physics Research Section B: Beam Interactions with Materials and Atoms*, 204:319–324, 2003.

[9] RE Laxdal. Acceleration of radioactive ions. *Nuclear Instruments and Methods in Physics Research Section B: Beam Interactions with Materials and Atoms*, 204:400–409, 2003.

[10] RE Laxdal, PG Bricault, T Reis, and DV Gorelov. A separated function drift-tube linac for the ISAC project at TRIUMF. In *Proceedings of the 1997 Particle Accelerator Conference (Cat. No. 97CH36167)*, volume 1, pages 1194–1196. IEEE, 1997.

[11] R Tiede, U Ratzinger, H Podlech, and C Zhang. KONUS Beam Dynamics Designs Using H-Mode Cavities. In *Proceedings Hadron Beam 2008*, pages 223–30, 2008.

[12] O Shelbaya and OK Kester. Toward an End-to-End Model for ISAC-I Accelerators. In *Journal of Physics: Conference Series*, volume 1067, page 062028. IOP Publishing, 2018.

[13] Richard Baartman. `TRANSOPTR`: Changes since 1984. Technical Report TRI-BN-16-06, TRIUMF, 2016.

[14] O Shelbaya, R Baartman, and O Kester. Fast radio frequency quadrupole envelope computation for model based beam tuning. *Phys. Rev. Accel. Beams*, 22(11):114602, DOI: `10.1103/PhysRevAccelBeams.22.114602`, Nov 2019.

[15] Olivier Shelbaya. The TRANSOPTR Model of the ISAC Drift Tube Linear Accelerator - Part I: Longitudinal Verification. Technical Report TRI-BN-20-08, TRIUMF, 2020.

[16] Olivier Shelbaya, Tiffany Angus, Rick Baartman, Paul M. Jung, Oliver Kester, Spencer Kiy, Thomas Planche, and Stephanie D. Rädel. Autofocusing drift tube linac envelopes. *Phys. Rev. Accel. Beams*, 24:124602, DOI: `10.1103/PhysRevAccelBeams.24.124602`, Dec 2021.

[17] Olivier Shelbaya. TRANSOPTR Implementation of the MEBT Beamline. Technical Report TRI-BN-19-02, TRIUMF, 2019.

[18] Olivier Shelbaya. TRANSOPTR Implementation of the HEBT Beamlines. Technical Report TRI-BN-19-06, TRIUMF, 2019.

[19] Olivier Shelbaya. TRANSOPTR Implementation of ISAC-II. Technical Report TRI-BN-19-13, TRIUMF, 2019.

[20] Olivier Shelbaya, Spencer Kiy, Richard Baartman, and Oliver Kester. Toward Autonomous Phasing of ISAC Heavy Ion LINACs. In *10th Int. Particle Accelerator Conf.(IPAC'19), Melbourne, Australia, 19-24 May 2019*, pages 3827–3830, 2019.

[21] Barquest C. Web-Based Control Room Applications at TRIUMF. In *Proceedings of the 9th International Particle Accelerator Conference*, pages 4832–35, 2018.

[22] Spencer Kiy, RE Laxdal, Marco Marchetto, S.D. Rädel, O Shelbaya, et al. Beam-Based Measurements of the ISAC-II Superconducting Heavy Ion Linac. In *Proceedings of the 9th International Particle Accelerator Conference*, pages 4832–35, 2018.

[23] Leo R Dalesio, AJ Kozubal, and MR Kraimer. Epics architecture. Technical report, Los Alamos National Lab., NM (United States), 1991.

[24] Guido Van Rossum and Fred L Drake Jr. *Python tutorial*, volume 620. Centrum voor Wiskunde en Informatica Amsterdam, 1995.

[25] Klaus Wille. *The physics of particle accelerators: an introduction.* Clarendon Press, 2000.

[26] Jankowiak, Andreas and Kamps, Thorsten. Physik und Technik moderner Teilchenbeschleuniger. Lecture, Humboldt-Universität zu Berlin, 2012-2013.

[27] T P Wangler. *RF Linear Accelerators.* Wiley Series in Beam Physics and Accelerator Technology. Wiley, 1998.

[28] Bernhard J. Holzer. Beam optics and lattice design for particle accelerators. (arXiv:1303.6514):171–206. 36 p, Mar 2013.

[29] Richard Baartman. Aberrations in Electrostatic Quadrupoles. Technical Report TRI-DN-95-21, TRIUMF, 1995.

[30] Edmund J N Wilson. Transverse beam dynamics; 1985 ed. 1985.

[31] A Verdier. Chromaticity (particle accelerators). Technical Report 10.5170/CERN-1995-006.77, CERN, 1995.

[32] R Baartman. Quadrupole shapes. *Physical Review Special Topics-Accelerators and Beams*, 15(7):074002, 2012.

[33] Rick Baartman. Low energy beam transport design. *CERN Yellow Reports: School Proceedings*, 5:491–491, 2018.

[34] Claude Bovet, Robert Gouiran, Karl Helmut Reich, and Igor Gumowski. A selection of formulae and data useful for the design of AG synchrotrons. Technical Report CERN-MPS-SI-Int-DL-70-4, CERN, 1970.

[35] Marco Marchetto et al. ISAC-II operation and future plans. *LINAC08, Victoria, British Columbia, CANADA*, page 1, 2008.

[36] RE Laxdal, G Clark, K Fong, A Mitra, M Pasini, R Poirier, I Sekachev, G Stanford, et al. Superconducting Accelerator Activities at TRIUMF/ISAC. In *Proc. 14th Int. Linac Conf., Korea*, 2002.

[37] MA Fraser. Second-order transit time factors for a two gap resonator. Technical Report HIE-ISOLDE-PROJECT-Note-0005, 2009.

[38] Bricault P, Poirier R, Ries T, Roper R, and Standford S. Tank1 of the ISAC-DTL Linac. In *Proceedings of the 1999 Particle Accelerator Conference, New York, NY*, pages 3540–42, 1999.

[39] Heighway EA and Hutcheon RM. Transoptr - A second order beam transport design code with optimization and constraints. Technical report, Atomic Energy of Canada Limited, 1981.

[40] Karl L. Brown, Frank Rothacker, David C. Carey, and F. C. Iselin. TRANSPORT: A Computer Program for Designing Charged Particle Beam Transport Systems. 1973.

[41] Frank J Sacherer. RMS envelope equations with space charge. *IEEE Transactions on Nuclear Science*, 18(3):1105–1107, 1971.

[42] Goldstein H., Poole C.P., and Safko J.L. *Classical Mechanics*. Addison Wesley, 2002.

[43] R. Baartman, Bach F, and et al. Bylinsky Y. Reliable Production of Multiple High Intensity Beams With the 500 MeV TRIUMF Cyclotron. In *Proceedings of the Cyclotrons 2010 Conference*, pages 280–2, 2010.

[44] Richard Baartman. Linac Envelope Optics. Technical Report TRI-BN-15-03, TRIUMF, 2015.

[45] R. Baartman. Fast Envelope Tracking for Space Charge Dominated Injectors. In *Proceedings of LINAC 2016 Conference*, pages 1017–21, 2016.

[46] MS De Jong and EA Heighway. A first order space charge option for transoptr. *IEEE Transactions on Nuclear Science*, 30(4):2666–2668, 1983.

[47] Richard Baartman et al. Fast envelope tracking for space charge dominated injectors. In *Proceedings of LINAC 2016 Conference*, pages 1017–21, 2016.

[48] Karl L Brown. Slac-75. *A First-and Second-Order Matrix Theory For the Design of Beam Transport Systems and Charged Particle Spectrometers*, 1967.

[49] Richard Baartman. Electrostatic Bender Optics. Technical Report TRI-DN-05-07, TRIUMF, 2005.

[50] Richard Baartman. Linearized Equations of Motion in Magnet with Median Plane Symmetry. Technical Report TRI-DN-05-06, TRIUMF, 2005.

[51] IM Kapchinskij and NV Lazarev. The linear accelerator structures with space-uniform quadrupole focusing. *IEEE Transactions on Nuclear Science*, 26(3):3462–3468, 1979.

[52] Staples JW. RFQ's - An Introduction. Technical report, Lawrence Berkeley Laboratory, 09 1990.

[53] Wikimedia Commons. `https://commons.wikimedia.org/wiki/File:RFQ_accelerator_schematic.svg`, 2013. Accessed: 2023-02-08.

[54] Olivier Shelbaya. A Quick TRANSOPTR Primer. Technical Report TRI-BN-20-06, TRIUMF, 2020.

[55] Peter JM Van Laarhoven and Emile HL Aarts. Simulated annealing. In *Simulated annealing: Theory and applications*, pages 7–15. Springer, 1987.

[56] Press WH. *Numerical Recipes 3rd Edition: The Art of Scientific Computing.* Cambridge University Press, Cambridge, England, 3 edition, 2007.

[57] Rick Baartman. Low energy beam transport design optimization for RIBs. *Nuclear Instruments and Methods in Physics Research Section B: Beam Interactions with Materials and Atoms*, 204:392–399, 2003.

[58] RH Merson. An operational method for the study of integration processes. In *Proc. Symp. Data Processing*, volume 1, page 25. Weapons Research Establishment, 1957.

[59] Richard Baartman. Runge-Kutta Customization for TRANSOPTR. Technical Report TRI-BN-18-09, TRIUMF, 2018.

[60] Olivier Shelbaya. ISAC-RFQ Parameter Documentation. Technical Report TRI-BN-22-07, TRIUMF, 2022.

[61] Olivier Shelbaya. Anomalous Operational OLIS Tunes. Technical Report TRI-BN-19-20, TRIUMF, 2019.

[62] Olivier Shelbaya. Report On OLIS Quadrupoles 5 and 7. Technical Report TRI-BN-22-12, TRIUMF, 2022.

[63] Olivier Shelbaya and Richard Baartman. Langevin-Like DTL Triplet BI Fits and Analysis of Transverse DTL Tuning Difficulties. Technical Report TRI-BN-19-18, TRIUMF, 2019.

[64] Olivier Shelbaya. Sequential Tune Optimization with TRANSOPTR. Technical Report TRI-BN-20-14, TRIUMF, 2020.

[65] Shane Koscelniak. Design History of the ISAC RFQ. Technical Report TRI-DN-95-04, TRIUMF, 1995.

[66] Koscielniak Sand L. Root, Lee R, R. Laxdal, and Grguric I. Beam Dynamics of the TRIUMF ISAC RFQ. In *Proceedings of LINAC96, Geneva, Switzerland*, pages 402–404, 1996.

[67] GM Stinson. A design for short quadrupoles for the ISAC MEBT beam line. Technical Report TRI-DNA-97-01, TRIUMF, 1997.

[68] GM Stinson. Conceptual Design for the MEBT Dipoles . Technical Report TRI-DNA-97-03, TRIUMF, 1997.

[69] GM Stinson. A design for a 4-in. x-y steerer for the MEBT beam line. Technical Report TRI-DNA-99-02, TRIUMF, 1999.

[70] GM Stinson. MEBT quadrupole measurements and computed losses of unaccelerated beam. Technical Report TRI-DNA-99-04, TRIUMF, 1999.

[71] Robert Laxdal. Concept Design for Quadrupole Triplets for the ISAC Separated Function Drift Tube Linac. Technical Report TRI-DN-99-05, TRIUMF, 1999.

[72] DV Gorelov, PN Ostroumov, and RE Laxdal. Use of the LANA Code for the Design of a Heavy Ion Linac. In *Proceedings of the 1997 Particle Accelerator Conference (Cat. No. 97CH36167)*, volume 2, pages 2621–2623. IEEE, 1997.

[73] RE Laxdal, B Boussier, K Fong, M Laverty, AK Mitra, and V Zviagintsev. ISAC-II QWR cavity characterizations and investigations. *Physica C: Superconductivity*, 441(1-2):193–196, 2006.

[74] A Facco, V Zviagintsev, R Laxdal, and Enrico Chiaveri. The superconducting medium beta prototype for radioactive beam acceleration at TRIUMF. In *PACS2001. Proceedings of the 2001 Particle Accelerator Conference (Cat. No. 01CH37268)*, volume 2, pages 1092–1094. IEEE, 2001.

[75] RE Laxdal and M Marchetto. The ISAC post-accelerator. *Hyperfine Interactions*, 225(1-3):79–97, 2014.

[76] O. Shelbaya, R.A. Baartman, and O.K. Kester. End-to-End RMS Envelope Model of the ISAC-I Linac. In *Int. Particle Accelerator Conf.(IPAC'21), Campinas, SP, Brazil*, Aug 2021.

[77] O. Shelbaya, R.A. Baartman, P.M. Jung, O.K. Kester, S. Kiy, T. Planche, Y.-N. Rao, and S.D. Rädel. On-Line Retuning of ISAC Linac Beam with Quadrupole Scan Tomography. In *Int. Particle Accelerator Conf.(IPAC'21), Campinas, SP, Brazil*, Aug 2021.

[78] Olivier Shelbaya. Maximum Entropy Tomography at the ISAC-RFQ. Technical Report TRI-BN-20-12, TRIUMF, 2020.

[79] M Marchetto, J Aoki, K Langton, RE Laxdal, W Rawnsley, JE Richards, et al. The ISAC-II current monitor system. *LINAC10, Tsukuba*, 2010.

[80] R.E. Laxdal. Optimization of the Charge Selection Section of MEBT. TRIUMF, unpublished report, Sept. 1997.

[81] Spencer Kiy. LLRF Phase Shifter Calibrations, October 2020. Technical Report TRI-BN-20-19, TRIUMF, 2020.

[82] Olivier Shelbaya. Overfocusing of the MEBT Bunch Rotator. Technical Report TRI-BN-21-18, TRIUMF, 2021.

[83] Richard Baartman. SLIT routine for TRANSOPTR. Technical Report TRI-BN-19-21, TRIUMF, 2019.

[84] Olivier Shelbaya. Addition of global time tracking to TRANSOPTR. Technical Report TRI-BN-20-03, TRIUMF, 2020.

[85] R. Tiede, G. Clemente, H. Podlech, U. Ratzinger, A. C. Sauer, and S. Minaev. LORASR code development. *Conf. Proc. C*, 060626:2194–2196, 2006.

[86] R. Tiede, D. Mäder, N. Petry, H. Podlech, U. Ratzinger, and C. Zhang. Improvements of the LORASR Code and their Impact on Current Beam Dynamics Designs. In *27th International Linear Accelerator Conference*, page TUPP063, 2014.

[87] Olivier Shelbaya. OLIS to RFQ Beam Transport and Acceleration in TRANSOPTR. Technical Report TRI-BN-20-13, TRIUMF, 2020.

[88] Richard Baartman. ISAC LEBT. In *ISAC and ARIEL: The TRIUMF Radioactive Beam Facilities and the Scientific Program*, pages 69–77. Springer, 2013.

[89] Kristin Wu. Profile Monitor Signal Classification using Random Forest Classifier. Technical Report TRI-BN-21-11, TRIUMF, 2021.

[90] Olivier Shelbaya. Model Coupled DTL Drifting Tune On-Line. Technical Report TRI-BN-22-13, TRIUMF, 2022.

[91] Jonathan Aoki. The ISAC Operators' Manual Section 3.7 - Beam Delivery, Release 2. TRIUMF Document-76739, TRIUMF, 2015.

[92] TRIUMF RIB Operations Group. RIB Operations Electronic Logbook, 2022.

[93] Robert Laxdal. Test3 - Commissioning Preparation and Test Results. Technical Report TRI-DN-00-29, TRIUMF, 2000.

[94] RE Laxdal. Completion and Operations of ISAC-I and Extension to ISAC-II. In *PACS2001. Proceedings of the 2001 Particle Accelerator Conference (Cat. No. 01CH37268)*, volume 1, pages 556–560. IEEE, 2001.

[95] J. Lassen, R. E. Laxdal, M. Marchetto, and V. A. Verzilov. Upgrade of the ISAC Time-of-flight System. *Conf. Proc. C*, 110904:1147–1149, 2011.

[96] M Marchetto, RE Laxdal, and V Zvyagintzev. Beam quality and operational experience with the superconducting LINAC at the ISAC II RIB facility. In *2007 IEEE Particle Accelerator Conference*, pages 1392–1394. IEEE, 2007.

[97] O Shelbaya, R Baartman, P M Jung, O Kester, T Planche, and S.D. Rädel. Transfer Matrix Optimization of Multigap Accelerating Cavities. *Working Paper.*

[98] M Marchetto, J Berring, and RE Laxdal. Upgrade of the isac dtl tuning procedure at triumf. *EPAC08, Genoa*, page 3440, 2008.

[99] L Dahl, J Klabunde, P Strehl, and V Schaa. Longitudinal and Transverse Beam Optimization at the Unilac. In *Proc. 1979 Lin. Accel. Conf.*, 1979.

[100] J. Nasser, R.A. Baartman, O.K. Kester, S. Kiy, T. Planche, S.D. Rädel, and O. Shelbaya. Algorithm to Mitigate Magnetic Hysteresis in Magnets with Unipolar Power Supplies. In *Proc. IPAC'22*, number 13 in International Particle Accelerator Conference, pages 156–159. JACoW Publishing, Geneva, Switzerland, 07 2022.

[101] David Yuchen Wang, Harpriya Bagri, Calum Macdonald, Spencer Kiy, Paul Jung, Olivier Shelbaya, Thomas Planche, Wojciech Fedorko, Rick Baartman, and Oliver Kester. Accelerator Tuning with Deep Reinforcement Learning. In *Workshop at the 35th Conference on Neural Information Processing Systems (NeurIPS)*, Vancouver, BC, Canada, 2021.